BER the international journal of bridge engineering management and research

Editorial
Vol. 2, No. 4 (2025) Issue of International Journal of Bridge Engineering, Management and Research (IJBEMR)

Anil K. Agrawal, Dist. M. (ASCE), Ph.D., P.E.

Editor-in-chief, International Journal of Bridge Engineering, Management and Research
Professor and Chair of Civil Engineering
The City College of New York, New York, NY 10031, USA

Submitted: 01 October 2025 **Accepted:** 01 October 2025 **Publication date:** 10 October 2025

DOI: 10.70465/ber.v2i4.69

It is my pleasure to publish the October issue (4th issue) of Vol. 2 of the International Journal of Bridge Engineering, Management and Research. You can find detailed information about the journal in the inaugural issue published in September 2004 or at https://www.ijbemr.org. In this issue of the journal, we are pleased to bring to you six papers in innovative areas of bridge engineering.

Bridge deck deterioration poses a significant challenge to transportation infrastructure, resulting in costly maintenance and potential safety hazards. Traditional bridge deck assessments primarily rely on visual inspections, which can be subjective and fail to capture subsurface defects such as delamination, rebar corrosion, and concrete degradation. To enhance the accuracy of condition assessment, the paper entitled "**Clustering-Based Framework for Multi-Sensor Data Fusion in Bridge Deck Condition Assessment**" explores multi-sensor data fusion and clustering techniques for defect identification using Ground Penetrating Radar and Impact Echo. By integrating multiple nondestructive evaluation (NDE) datasets, a clustering-based framework was developed to automatically categorize bridge deck conditions. K-Means, Density-Based Spatial Clustering of Applications with Noise (DBSCAN), Gaussian Mixture Models, and Fuzzy C-Means clustering algorithms were evaluated to determine their effectiveness in grouping similar defect patterns. The optimal number of clusters is determined using the elbow method, silhouette score, and Davies–Bouldin Index. Results indicate that DBSCAN outperforms other clustering techniques in detecting defect hotspots while effectively handling noise and spatial inconsistencies. The clustered defects are mapped spatially to visualize regions of deterioration, enabling bridge engineers to identify high-risk areas and prioritize maintenance efficiently.

Edge fairing is often applied to box-girder bridge decks to improve their aerodynamic performance, particularly in long-span bridges. A thorough understanding of the aerodynamic response and flow behavior of bridge decks with edge fairings is essential for optimal design and ensuring wind-induced safety. The paper entitled "**Influence of Nose Position of Edge Fairing on Aerodynamic Characteristics of Box Girder Bridge Deck**" presents a numerical investigation into the influence of the nose position of edge fairings on the aerodynamic behavior of box-girder bridge decks. Two-dimensional unsteady Reynolds-averaged Navier–Stokes simulations were performed using the *k-ω-SST* turbulence model, supported by appropriate validation studies. Both static and dynamic simulations were conducted for two configurations: edge fairings with nose-up and nose-down positions. The static analysis showed that the nose-down configuration offered superior aerodynamic performance compared to the nose-up configuration. In the nose-down position, the deck experienced reduced static wind forces with smaller fluctuations. Flow features such as leading-edge flow separation and reattachment, as well as trailing-edge flow separation, played critical roles in influencing aerodynamic forces. The dynamic simulations further revealed that the nose-down fairing configuration had improved aerodynamic damping in both torsional and heaving modes. In particular, leading-edge flow reattachment was identified as the primary contributor to enhanced aerodynamic damping in the nose-down configuration. Further, the relatively larger bottom plate slope demonstrated better aeroelastic responses in the nose-down position of the edge fairing.

Seismic isolation is a well-established technique to protect structures against earthquakes, allowing to achieve a level of safety not possible with conventional systems. The Somplago viaduct on the Udine–Tarvisio highway, built in 1976, was the first seismically isolated bridge in Italy. Its good performance during the strong shocks, which hit the viaduct when it was still under construction, encouraged the use of

Discussion period open till six months from the publication date. Please submit separate discussion for each individual paper. This paper is a part of the Vol. 2 of the International Journal of Bridge Engineering, Management and Research (BER), ISSN 3065-0569.

seismic isolation in bridges. The development of applications in Italy was initially quite slow, due to the delays in considering this new technology in technical standards. Significant developments occurred following the major seismic events that affected the country. Today, seismic isolation is almost always used for new construction projects and, especially, in major cases, such as illustrated in this state-of-the-art review paper entitled "**State-of-the-Art Review and Applications of Seismic Isolation in Newly Built Bridges in Italy**."

Concrete bridge decks are susceptible to subsurface defects such as delamination, caused by aging, corrosion, and environmental stressors, underscoring the need for timely, reliable NDE. While traditional acoustic methods, such as hammer or chain drag, remain widely used, they suffer from subjectivity, inconsistent impact forces, and limited applicability on overhead or vertical surfaces. This study, entitled "**Smart Acoustic Sounding for Automated Delamination Detection in Concrete Bridge Decks**," introduces a novel smart acoustic sounding system that modernizes impact sounding through an integrated framework consisting of a broadband electronic chirp excitation source, high-sensitivity MEMS microphones with acoustic shielding, and a tracking camera for automated and location-aware inspections. Advanced signal processing techniques, such as empirical mode decomposition, power spectral density, and the Hilbert–Huang transform, are employed to filter noise, extract frequency-based features, and support machine learning-based defect classifications. Laboratory testing on a full-scale concrete slab embedded with known artificial defects (e.g., shallow and deep delamination, voids, and honeycombing), as well as a deteriorated concrete beam, confirmed the system's ability to accurately identify defect zones, particularly shallow delamination with characteristic frequency signatures in the range of 1–3 kHz. The system produced real-time defect maps with minimal human input, demonstrating its potential to improve the accuracy, repeatability, and efficiency of bridge deck inspections and support data-driven maintenance decisions.

The bridge crossing the Gesso River is a multi-span masonry arch bridge built in the 19th century in Cuneo, Piedmont, Italy. Due to extended local degradation and damage, the bridge recently underwent a significant strengthening intervention. Ambient vibration tests were performed both before and after strengthening to assess the effectiveness of the repairs. The paper entitled "**Dynamic investigations before and after the strengthening of a masonry arch bridge**" presents the results of the dynamic investigations, identifying the modal characteristics of the masonry bridge through different techniques. The pre-intervention analysis revealed clear anomalies, including a sort of "frequency splitting" phenomenon and irregularities in the mode shapes that were localized in the regions of maximum masonry decay. After the strengthening works, the identified modal parameters showed an increase in natural frequencies, along with the resolution of previously identified mode shape irregularities, indicating a clear improvement of the bridge's structural condition. As a final remark, the presented results highlight the value of operational modal analysis as a nondestructive tool for validating the effectiveness of rehabilitation measures.

The history of bridges is retraced as a witness to humanity's progress. The evolution of materials and structural typologies has enabled ever-longer spans to be overcome at sustainable costs. The availability of materials, such as reinforced concrete and steel, has offered new possibilities that were unthinkable using wood and masonry. Then girder bridges were built, and later cable-stayed and suspension bridges, but also long arch bridges. The race for long spans continues. Bridges have always been and always will be a monument to progress. The paper entitled "**History of Bridges: Materials and Structural Types of a Monument to Progress**" documents the progress in bridge engineering as monuments of the future are being created.

With this editorial note, it is also my pleasure to invite you to submit your papers addressing research with new and substantial contributions in bridge engineering to the International Journal of Bridge Engineering, Management and Research. The journal is committed to a prompt peer review process and online publication of the paper within 4 weeks of acceptance. We are also committed to completing our peer review process within 90 days of paper submission. You are invited to submit your papers to the next issue of the journal as soon as possible.

BER the international journal of bridge engineering management and research

Clustering-Based Framework for Multi-Sensor Data Fusion in Bridge Deck Condition Assessment

Ibukunoluwa Grace Tella[1,*]; Eyosias Beneberu[2]; and Nur Yazdani[3]

Submitted: 08 August 2025 **Accepted:** 15 September 2025 **Publication date:** 10 October 2025

DOI: 10.70465/ber.v2i4.50

Abstract: Bridge deck deterioration poses a significant challenge to transportation infrastructure, resulting in costly maintenance and potential safety hazards. Traditional bridge deck assessments primarily rely on visual inspections, which can be subjective and may fail to capture subsurface defects, such as delamination, rebar corrosion, and concrete degradation. To enhance the accuracy of condition assessment, this study explores multi-sensor data fusion and clustering techniques for defect identification using ground penetrating radar and impact echo (IE). By integrating multiple non-destructive evaluation datasets, a clustering-based framework was developed to automatically categorize bridge deck conditions. K-Means, density-based spatial clustering of applications with noise (DBSCAN), Gaussian Mixture Models, and Fuzzy C-Means clustering algorithms were evaluated to determine their effectiveness in grouping similar defect patterns. The optimal number of clusters was determined using the Elbow Method, Silhouette Score, and Davies–Bouldin Index. Results indicate that DBSCAN outperforms other clustering techniques in detecting defect hotspots while effectively handling noise and spatial inconsistencies. The clustered defects are mapped spatially to visualize regions of deterioration, enabling bridge engineers to identify high-risk areas and prioritize maintenance efficiently.

Author keywords: Bridge condition assessment; non-destructive evaluation (NDE); ground penetrating radar (GPR); impact echo (IE); clustering algorithms

Introduction

Bridge decks are critical components of transportation infrastructure, yet they are among the most susceptible to deterioration. Exposure to traffic loads, environmental stressors, and material aging accelerates the formation of cracks, delamination, spalling, and corrosion of embedded rebar (Fig. 1).[1,2] Traditionally, bridge condition assessments rely on visual inspections, as reported in the National Bridge Inventory (NBI), which uses a 0–9 rating scale based on observed surface defects.[3] However, visual inspections are inherently subjective and often fail to detect subsurface deterioration before it becomes severe.[4] This limitation leads to delayed maintenance, increased repair costs, and, in extreme cases, catastrophic failure. Several studies have highlighted the limitations of visual inspections, including inconsistencies among inspectors and the inability to detect early-stage subsurface defects.[1,5] Non-destructive evaluation (NDE) technologies offer the potential to enhance the accuracy of concrete bridge deck assessment, as they enable early detection of subsurface defects, such as delamination, rebar corrosion, and concrete degradation, without causing physical damage. These noninvasive techniques facilitate more effective maintenance planning and reduce long-term repair costs.[1,6,7,8,9,10,11]

The FHWA and various Departments of Transportations (DOTs) have increasingly adopted NDE technologies to improve traditional bridge evaluation.[6] Among the various NDE methods, ground penetrating radar (GPR) and impact echo (IE) have been widely adopted for bridge deck condition assessment.[1,12,13]

GPR transmits electromagnetic waves into concrete substrates and records the reflected signals to assess internal conditions, such as rebar cover, moisture intrusion, and material quality.[5,14] The system, often mounted on a three-wheel cart or truck (Fig. 2), enables rapid scanning of bridge deck areas. Reflected signals are displayed as radargrams, which aid in identifying subsurface anomalies. Hyperbolic patterns in the radargram indicate the presence of embedded features such as rebars, while the A-scan waveform, a one-dimensional plot of signal amplitude versus time or depth at a single point, highlights amplitude changes with depth (Fig. 3).

*Corresponding Author: Ibukunoluwa Grace Tella. Email: igo8917@mavs.uta.edu

[1]PhD Candidate, Department of Civil Engineering, The University of Texas at Arlington

[2]Associate Professor of Practice, Department of Civil Engineering, The University of Texas at Arlington

[3]Dr. Tseng Huang Endowed Professor, Department of Civil Engineering, The University of Texas at Arlington

Discussion period open till six months from the publication date. Please submit separate discussion for each individual paper. This paper is a part of the Vol. 2 of the International Journal of Bridge Engineering, Management and Research (BER), ISSN 3065-0569.

Figure 1. Bridge deck deterioration

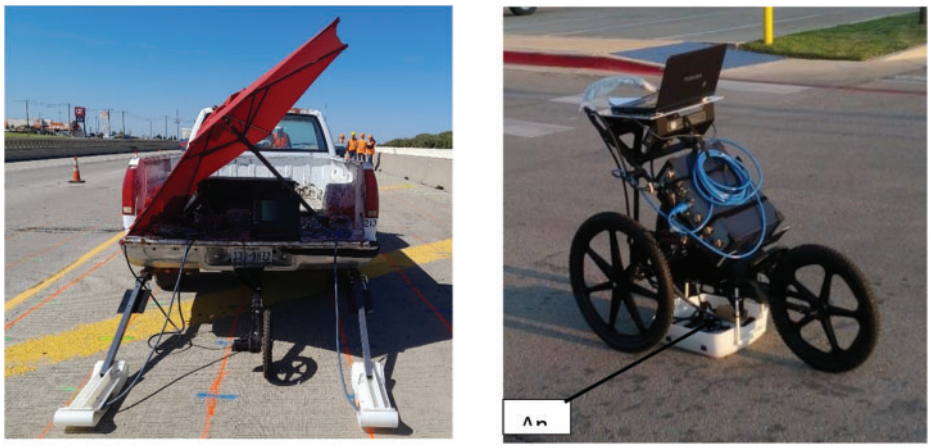

Figure 2. GPR system. (a) Truck-mounted GPR and (b) Three-wheel cart-mounted GPR

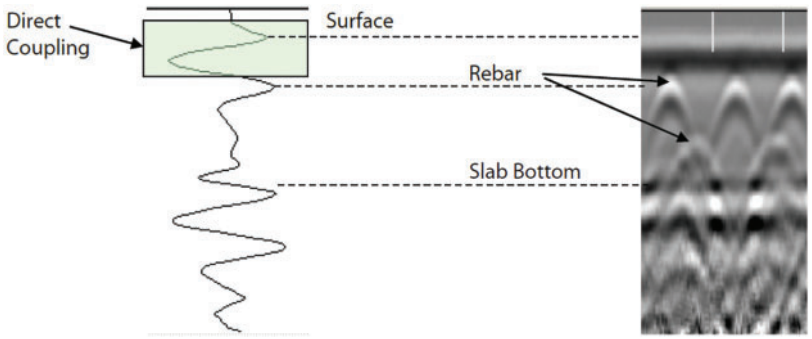

Figure 3. Typical GPR radargrams for bridge deck analysis[15]

Several studies have demonstrated the effectiveness of GPR in bridge deck evaluation. Hasan and Yazdani[16] investigated a Texas bridge deck using a 2.6 GHz antenna to detect variations in rebar cover depth. The study revealed that nearly 48% of the deck had inadequate cover. Hugenschmidt[17] conducted GPR scans on multiple bridges using a 1.2 GHz antenna and successfully identified asphalt pavement thickness variations and rebar cover inconsistencies with an average error of 6 mm when compared to core samples. These findings highlight the precision and reliability of GPR in noninvasive bridge deck assessment. However, it has limitations, including signal attenuation in moisture-rich environments and reduced effectiveness in detecting air-filled voids or delaminations.[18]

IE is a stress-wave-based technique used to detect concrete thickness and internal defects, such as delaminations, voids, and cracks, in bridge decks. The device can be a hand-held unit or a sonic surface scanner, as shown in Fig. 4. It provides a comprehensive view of subsurface conditions through analysis of frequency response.[13] The

method involves striking the deck surface with a mechanical impactor, generating stress waves that travel through the concrete. When these waves encounter defects, they reflect to the surface at distinct frequencies, which are then captured by a sensor (Fig. 5). Analyzing the frequency spectrum reveals the presence, depth, and extent of defects. Higher frequencies indicate shallower anomalies, while lower frequencies correspond to deeper defects. IE is particularly effective at detecting early-stage deterioration caused by rebar corrosion and freeze–thaw cycles, distinguishing between intact and deteriorated concrete.[19] However, the traditional hand-held IE device can be time-consuming, as it requires point-by-point surface contact and is sensitive to surface roughness. In contrast, the sonic surface scanner–IE system enables faster, continuous deck scanning, significantly improving efficiency and minimizing traffic disruptions. La et al.[20] successfully identified delaminations across multiple bridges using IE, later confirmed through coring. By integrating IE with GPR, the study provided a comprehensive assessment of both rebar-related issues and concrete integrity. Combining these methods enhances bridge condition assessment, allowing engineers to make informed decisions for maintenance and rehabilitation.

Although both GPR and IE provide valuable insights, no single technique can comprehensively assess concrete bridge deck condition. Despite the valuable data generated by these methods, their effectiveness is often limited by the need for manual interpretation and the complexity of large datasets. Machine learning (ML) algorithms enable efficient processing of large volumes of data, minimizing human error and subjectivity in defect classification. Additionally, they provide a promising approach to automating defect detection, enhancing classification accuracy, and improving predictive modeling.

ML techniques, particularly unsupervised clustering algorithms, can provide innovative solutions for bridge deck condition assessment by categorizing defect patterns without predefined labels.[19] Clustering algorithms group similar data points, making them valuable for automated defect identification and categorization of NDE data. Unlike threshold-based methods, clustering algorithms adapt to complex data distributions, enhancing defect detection accuracy. Several recent studies have also explored the use of multi-sensor data fusion, combiningGPR and IE with unsupervised learning.[21,22,23,24] Hoxha et al.[25] developed a robotic platform that integrates GPR and IE for automated subsurface defect mapping, demonstrating the potential for combining mobility with data-driven condition assessment. Similarly, Jafari and Dorafshan[26] compared supervised and unsupervised approaches for delamination detection using IE data, highlighting the advantages of unsupervised learning in the absence of labeled datasets. Völker and Shokouhi[27]

Figure 4. IE device. (a) Sonic surface scanner–IE system and (b) Hand-Held IE system

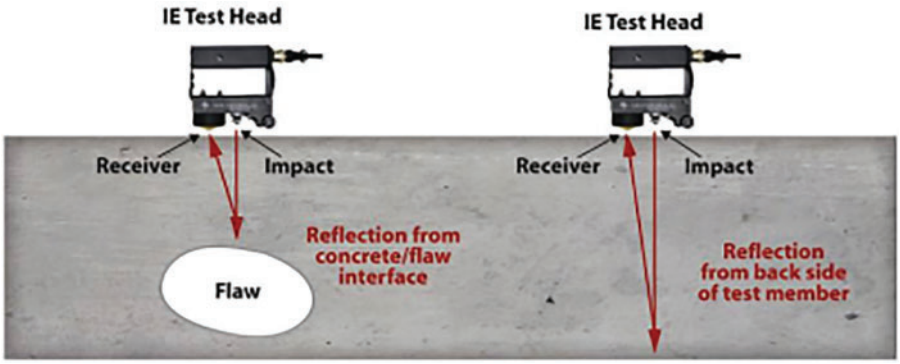

Figure 5. IE working principle

applied clustering-based fusion of IE, GPR, and ultrasound data for detecting simulated honeycombing in a concrete slab. The study demonstrated that density-based spatial clustering of applications with noise (DBSCAN) outperformed both K-Means and Fuzzy C-Means (FCMs), improving defect detectability by up to 10%. However, their study was limited to lab-scale testing on a single concrete specimen, and the transportability of their method to field-scale data remains an open question.

Various clustering techniques have been applied to bridge condition assessment, including K-means, DBSCAN, Gaussian Mixture Models (GMMs), and FCMs. K-Means, a centroid-based algorithm, assigns each data point to the nearest cluster center; however, it remains sensitive to outliers and noise.[28] DBSCAN identifies clusters based on point density, making it well-suited for detecting defect hotspots, handling irregular distributions in NDE datasets, and managing noise without needing a predefined number of clusters.[29] GMM employs probabilistic clustering with soft assignments, enabling the effective detection of overlapping defect regions and providing flexibility in modeling.[30] FCM, similar to GMM, enhances clustering by permitting data points to belong to multiple clusters, making it effective for analyzing uncertain and transitional defect zones in NDE data.[31]

Several studies have applied ML to NDE techniques, but most focus on single method clustering rather than true multi-sensor fusion. For example, Dinh and Zayed[5] developed a fuzzy logic-based approach using GPR data alone, lacking delamination insights from IE. Gagarin et al.[18] proposed a step-frequency GPR model that addresses only rebar corrosion without spatial clustering. Ibrahim et al.[19] applied fuzzy clustering to bridge deck defects, but did not integrate multiple NDE datasets. Additionally, Pedram et al.[32] used ML algorithms to analyze infrared images of reinforced concrete structures, improving corrosion defect identification. Omar and Nehdi[33] applied clustering algorithms to UAV-based infrared thermography (IRT) data, segmenting thermal images to detect delaminations without disrupting traffic.

Although these techniques enhance defect detection, challenges remain in integrating multiple large-volume NDE datasets and extracting meaningful condition patterns. Despite advancements in applying ML to NDE, most studies have focused on single-method analysis, often neglecting the integration of diverse NDE datasets needed for comprehensive defect identification. While past studies have shown the value of combining sensors and ML, most have been limited to lab environments, robotic setups, or isolated structural elements. The current research addresses this knowledge gap by developing a clustering-based multi-sensor data fusion framework that combines GPR and IE data to provide an automated and objective assessment of bridge deck condition. The proposed methodology was applied to eight full-scale bridges with diverse deck types, each with distinct construction techniques and deterioration patterns, demonstrating the practical scalability and real-world applicability of unsupervised learning in bridge deck evaluation. Building upon previous works,[5,19,32,33] this study integrates GPR and IE data within a clustering-based condition assessment model, offering a highly comprehensive view of bridge deck deterioration. This will consequently enhance accuracy, reliability, and efficiency in bridge infrastructure evaluation. The combination of GPR, IE, and ML-based clustering provides a robust approach to bridge monitoring, supporting improved maintenance and rehabilitation planning.

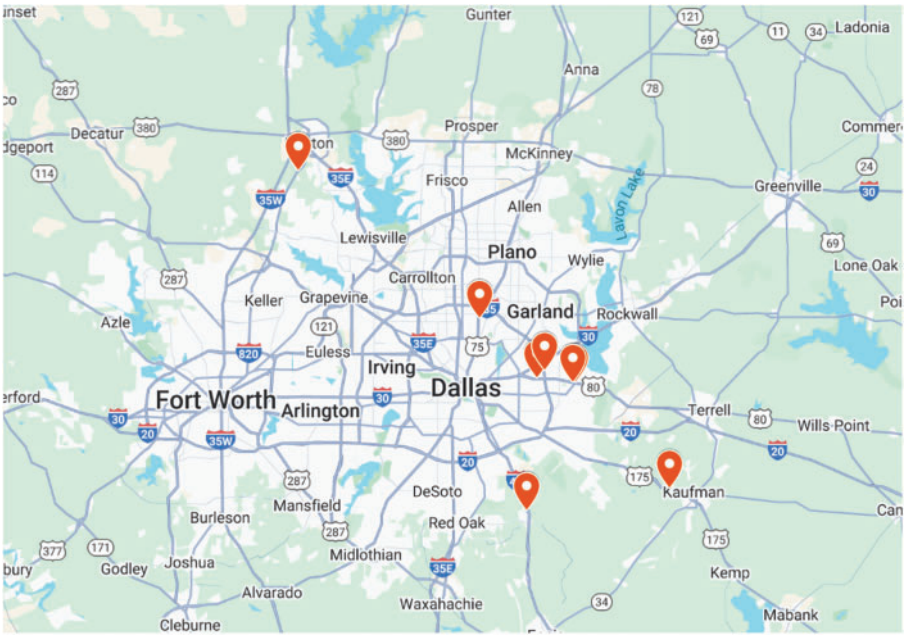

Figure 6. Bridge locations

Data Collection and Bridge Description

Field data was collected from eight different bridges in Texas using GPR and IE to assess the selected concrete bridge decks. Fig. 6 shows the locations of these bridges on Google Maps. Two common deck construction types encountered were cast-in-place (CIP) concrete over precast concrete panels (PCPs), often used in combination in composite systems where the CIP concrete is poured on top of the PCP. The characteristics, along with the NBI deck condition rating of each bridge, are summarized in Table 1.

Each bridge presented unique structural features and challenges, creating a diverse dataset for subsequent analysis and model development. To facilitate the NDE work, the Texas DOT personnel implemented traffic control measures. Longitudinal grid lines, spaced 760 mm apart, were marked on the bridge deck to guide NDE scanning. A truck-mounted GPR system, equipped with two 2.6 GHz antennas, was used to scan the bridge decks at a speed of 2.2 m/s, significantly reducing the time required compared to traditional methods. For IE scanning, 760 mm grid intervals were used with the test head pressed against the deck, providing additional subsurface condition data to complement the GPR findings. Fig. 7 shows the NDE data collection for bridge 6.

Clustering Workflow

The overall clustering workflow used in this study is summarized in Fig. 8. It begins with database preparation and data preprocessing, which includes exploratory data analysis (EDA), data cleaning, and normalization. EDA was performed to identify outliers and understand the distribution of features such as two-way travel time (TWTT), amplitude, and frequency. Normalization was applied to scale the features between 0 and 1.

Following preprocessing, cluster validation techniques were applied to determine the optimal number of clusters. The Elbow Method was used to identify the point of diminishing returns in within-cluster variance, providing a visual guide for selecting an efficient number of clusters. The Silhouette Score quantified how well-separated the clusters were, ensuring good cohesion and separation. The Bayesian information criterion (BIC) was used specifically for the GMM to strike a balance between model fit and complexity. For FCM clustering, the fuzzy partition coefficient (FPC) was employed to evaluate the clarity of the fuzzy cluster assignments. These methods were selected because they are widely accepted for evaluating the quality of clustering across both hard and soft clustering models.[29,34,35]

Table 1. Bridge description

Bridge name	Designation	Location	Year built	NBI deck condition rating	Deck type	Girder type	Deck area (m^2)
I-635 Bridge	Bridge 1	Mesquite, TX	2024	N/A	CIP	Composite steel deck	1,079
US 75 Pedestrian Underpass	Bridge 2	Dallas, TX	2023	N/A	CIP atop steel panel	None (cable-supported)	274
Westbound (WB) US 175 Big Brushy Creek	Bridge 3	Kaufman, TX	1950	5	CIP	Flat slab	2,044
WB US 80 at SH 352	Bridge 4	Sunnyvale, TX	2012	7	CIP atop PCP	Concrete I-girder	1,917
EB & WB US 80 Main Lanes at Stream 2B6	Bridge 5	Mesquite, TX	2012	4	CIP atop PCP	Concrete U–beams	985
US 377 over Hickory Creek Relief	Bridge 6	Denton, TX	1942	4	CIP	Steel I-girder	677
BI 45 at Ten Mile Creek Relief	Bridge 7	Dallas, TX	2024	N/A	CIP atop PCP	Concrete I-girder	722
Eastbound (EB)US 80 at SH 352	Bridge 8	Sunnyvale, TX	2012	6	CIP atop PCP	Concrete I-girder	1,917

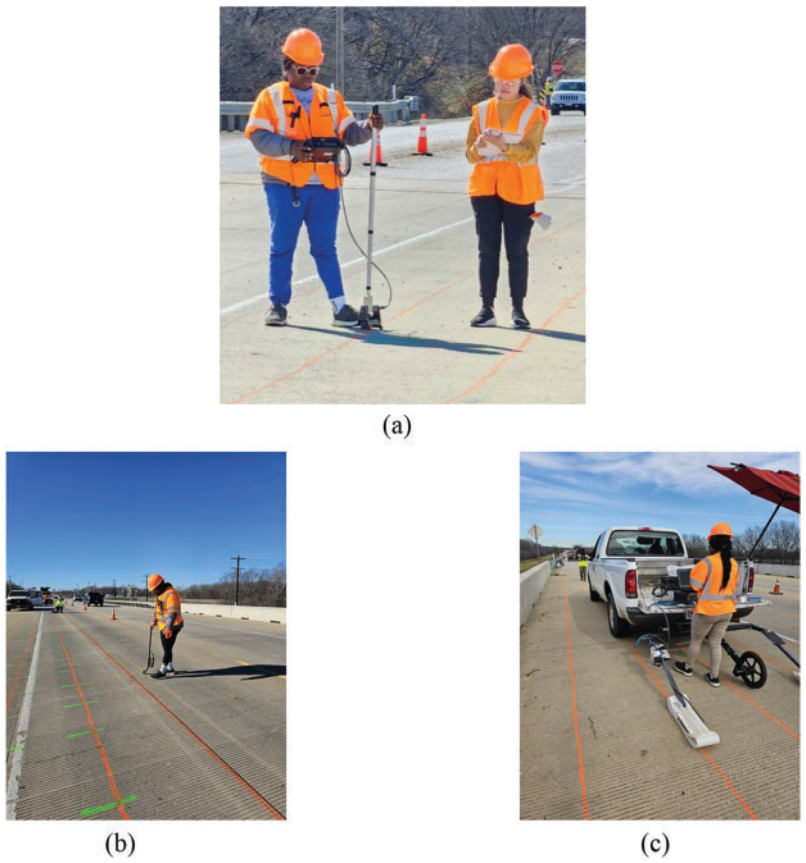

Figure 7. NDE scanning. (a) IE scanning, (b) GPR scanning gridlines, and (c) GPR deck scanning

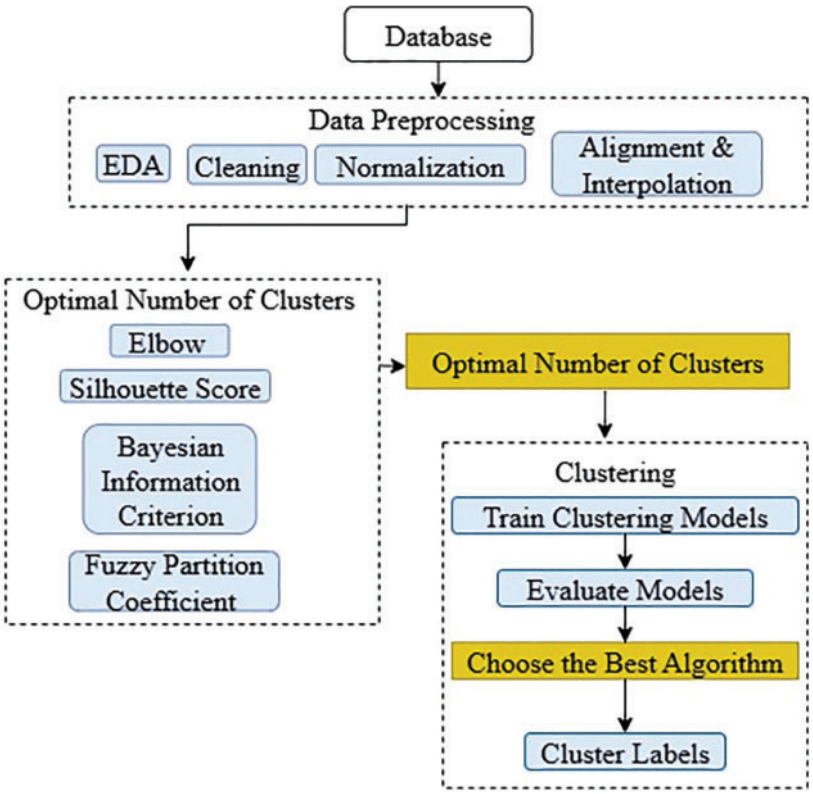

Figure 8. Clustering flowchart

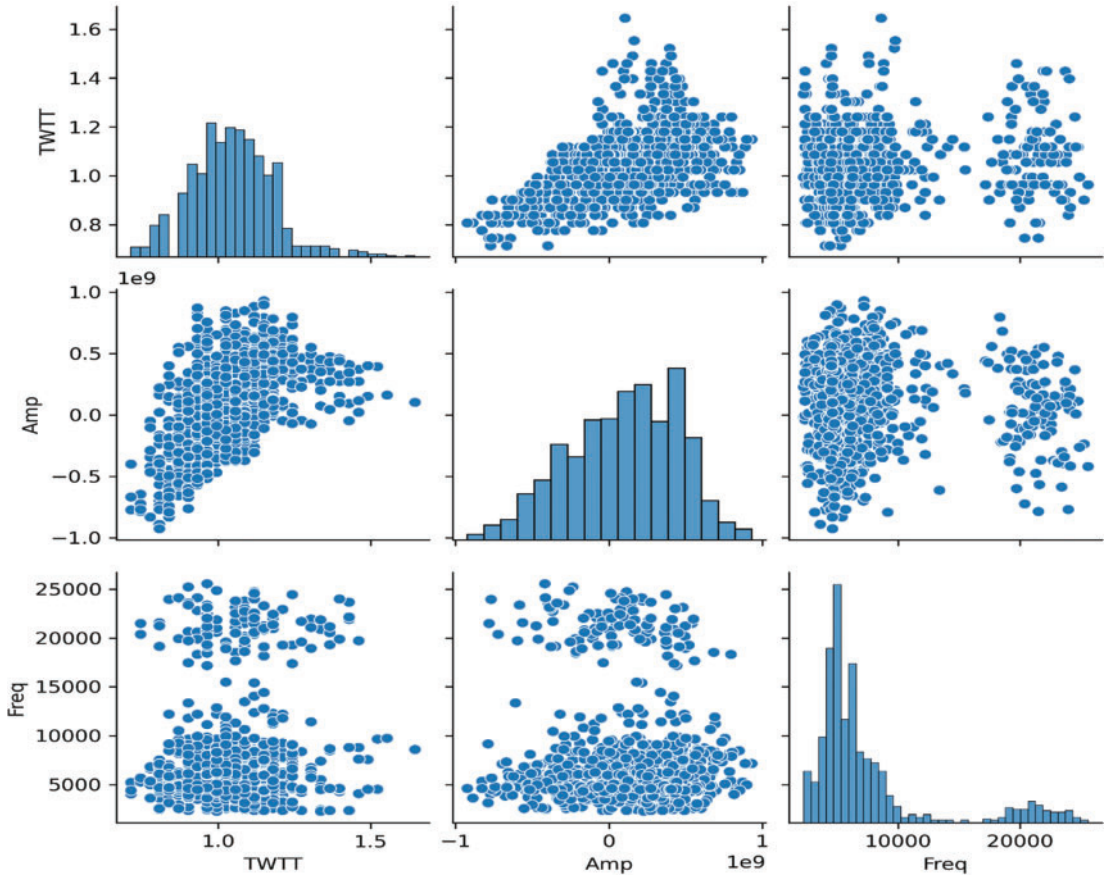

Figure 9. Raw GPR and IE feature distributions from test bridges before cleaning and normalization

Data Cleaning and Normalization

The collected GPR and IE data were preprocessed to ensure accuracy, consistency, and reliability. The first step involved data visualization to understand distribution patterns and detect anomalies. Noise and outliers were removed to enhance data quality. Feature normalization was applied, using Eq. (1), to ensure that TWTT, amplitude, and IE frequency values were within a standardized range of 0 to 1.[36] Histograms and scatter plots were generated to examine the raw feature distributions prior to normalization (Fig. 9). The result of the normalization process is shown in Fig. 10, illustrating consistent feature scaling suitable for subsequent analysis

$$X' = \frac{X - \min(X)}{\max(X) - min(X)} \frac{X - \min(X)}{\max(X) - min(X)} \quad (1)$$

where X is the original data and X' is the normalized data.

Data Alignment and Interpolation

To enable clustering of fused features from both sensors, the GPR and IE data were spatially aligned using a grid-based approach. GPR data points, which had higher spatial density, were retained as the reference grid. Each IE data point was matched to its nearest GPR neighbor based on spatial proximity using Euclidean distance.[37,38] In cases where multiple IE points mapped to the same GPR location, their values were averaged. For missing sensor values in sparse areas, inverse distance weighted interpolation was applied.[39,40] This allowed all features, including TWTT and amplitude from GPR and frequency from IE, to be combined for each grid cell. The resulting fused dataset maintained consistent x–y coordinates, ensuring reliable clustering across the combined feature space. This process ensured that all sensor readings were accurately mapped and spatially coherent, as demonstrated in the cluster distribution plots.

Cluster Number Determination

Since labeled condition states are not available for the GPR and IE data, supervised learning methods cannot be applied. Therefore, unsupervised learning techniques are necessary to discover inherent patterns and groupings in the dataset without predefined labels.[41,42] Selecting the optimal number of clusters (k) is a critical step in unsupervised learning, as it directly influences the quality and interpretability of the resulting clusters. The Elbow Method, Silhouette Score analysis, BIC, and FPC techniques were employed to determine the most suitable number of clusters for the integrated GPR and IE dataset.[35,34,28,29]

The Elbow Method involves plotting the within-cluster sum of squares for the selected features (TWTT, amplitude,

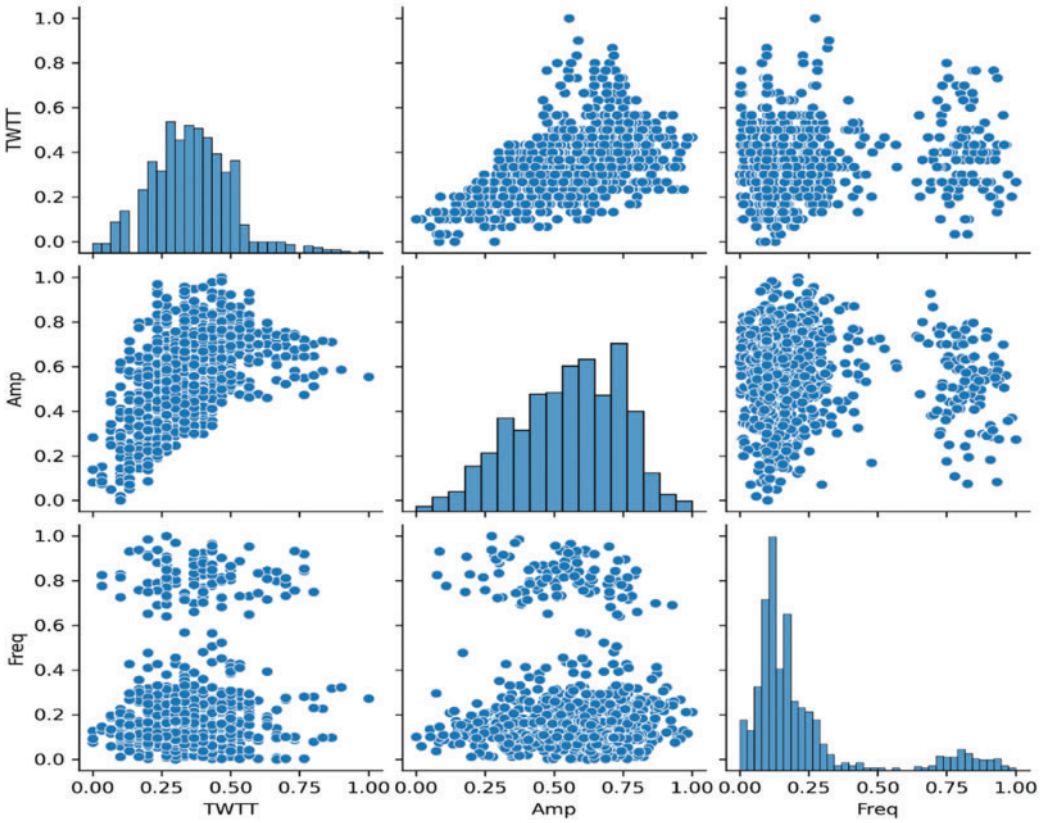

Figure 10. Normalized GPR and IE features from test bridges after preprocessing

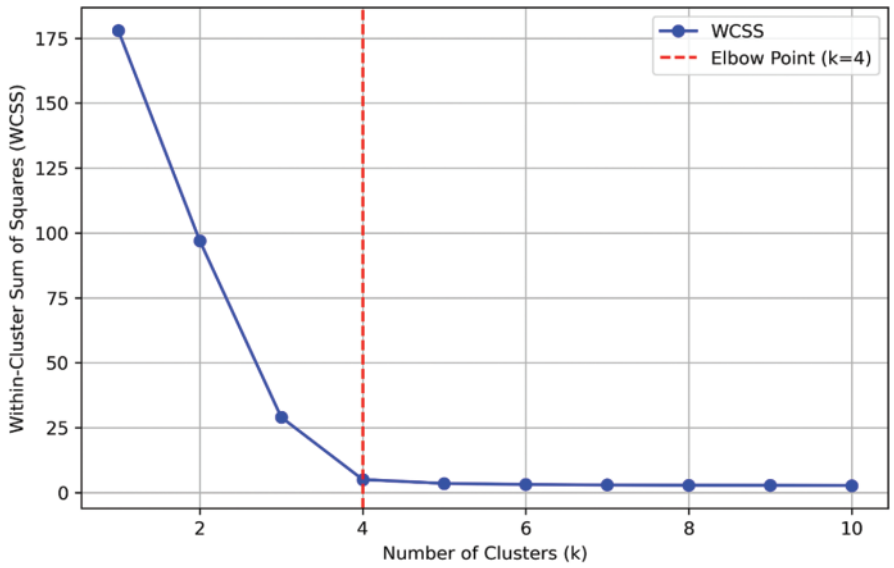

Figure 11. Elbow plot for K-means clustering

and IE frequency) against different values of "k." The point where the curve begins to flatten, referred to as the "elbow," indicates an optimal trade-off between compactness and model complexity. As shown in Fig. 11, the elbow occurs at k = 4, suggesting that four clusters provide an efficient representation of the dataset without overfitting. The Silhouette Score measures how well each data point fits within its assigned cluster relative to other clusters. A higher silhouette score indicates better cohesion within clusters and greater separation between clusters. As shown in Fig. 12, the average silhouette score reaches its maximum value at k = 4, further supporting this choice.

For the GMM, BIC was used to evaluate model fitness while removing excessive complexity. The lowest BIC value was observed at k = 4 (Fig. 13), indicating that this configuration achieved the best balance between data fit and parameter count. In the case of FCM, FPC was used to evaluate the clarity of the clustering structure. As expected,

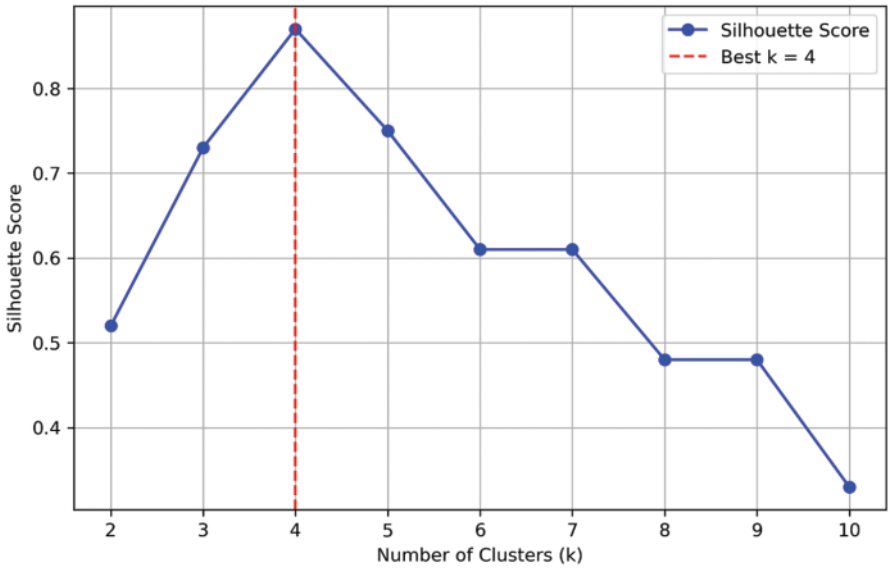

Figure 12. Silhoutte score versus number of clusters (K-means)

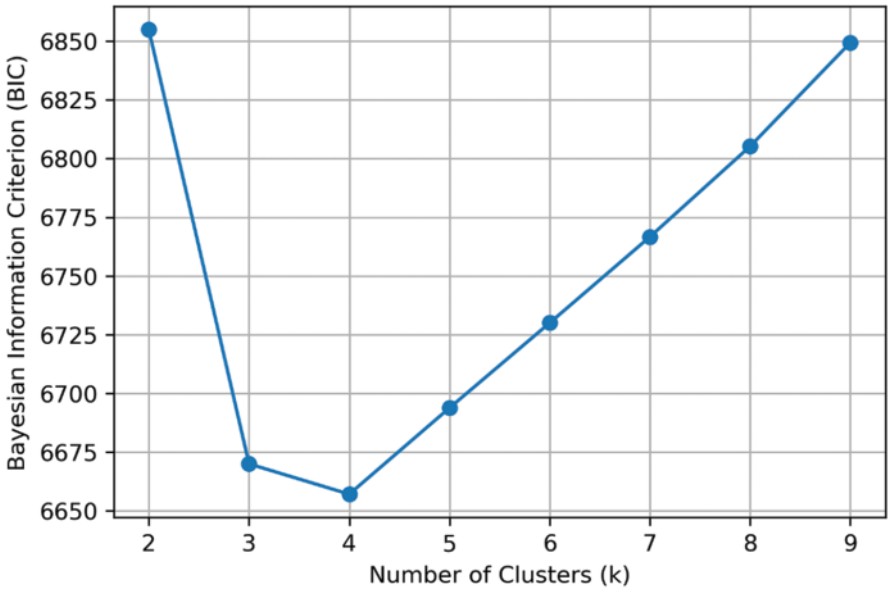

Figure 13. BIC versus number of clusters (GMM)

the FPC decreased as "k" increased, with the highest value observed at k = 2 (Fig. 14). However, the Elbow Method, Silhouette Score, and BIC consistently identified k = 4 as optimal. Thus, this value was used to configure the clustering algorithms in the subsequent analysis.

Clustering Model Development

After determining the optimal number of clusters (k = 4), four different clustering algorithms were used to identify patterns across the combined dataset from the eight bridges: K-Means, DBSCAN, GMM, and FCM. Each algorithm was selected for its unique strengths in identifying patterns and handling different data distributions. K-Means was chosen for its simplicity and efficiency in partitioning well-separated data.[28] DBSCAN was included due to its robustness in identifying clusters of arbitrary shape and handling noise points effectively.[29] The GMM algorithm was employed for its probabilistic clustering capabilities, which allow soft assignment of points to multiple clusters.[30] Finally, FCM was used to model the uncertainty and overlapping nature of bridge condition states, making it suitable for condition assessment applications involving gradual transitions between states.[42,41] The models were developed using Python (version 3.12.2, 2024) with supporting libraries, including Scikit-Learn for clustering, NumPy and Pandas for data manipulation, and Matplotlib for visualization. Parameter tuning was applied for each algorithm to optimize performance and ensure accurate cluster formation.

Collectively, the four clustering algorithms were applied systematically to the eight-bridge dataset to capture different

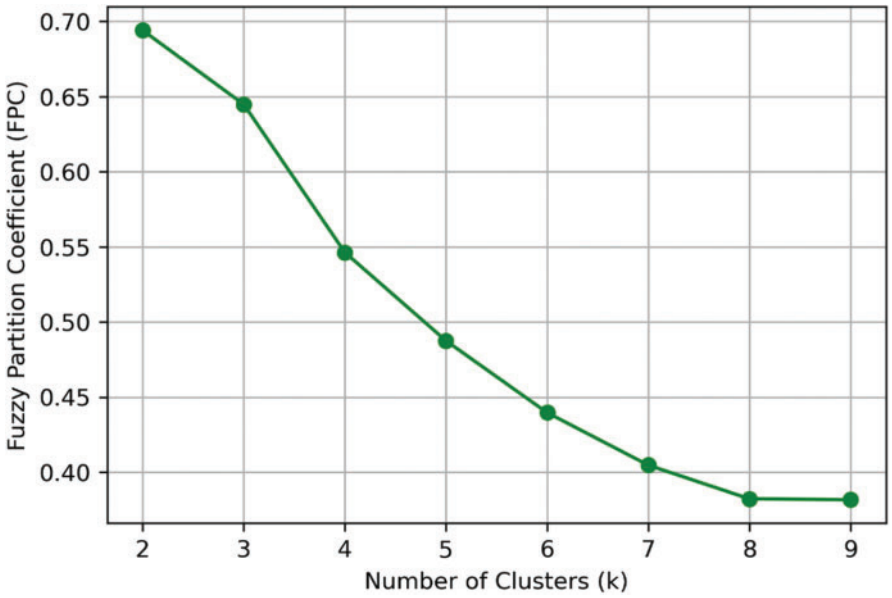

Figure 14. FPC versus number of clusters (FCM)

aspects of the defect patterns, ranging from sharp partitions to ambiguous transitions, providing complementary insights for subsequent analysis. Although the clustering models were trained on the combined data, the resulting cluster labels were also linked to individual bridge decks to show how these patterns manifest on specific bridges. The rationale and mechanics of each clustering method are summarized below.

K-means clustering

The primary objective of K-Means is to minimize WCSS from Eq. (2), which quantifies the total squared distance between each data point and its respective centroid.[28]

$$WCSS = \sum_{i=1}^{K} \sum_{x_j \in C_i} ||x_j - \mu_i||^2 \tag{2}$$

where $C_i =$ is the ith cluster, $\mu_i =$ centroid of cluster I, x_j is the data points in cluster i.

The K-Means algorithm operates in two main steps: (1) assigning each point to the nearest centroid using Euclidean distance; and (2) updating each centroid to the mean of its assigned points. These steps are repeated iteratively until the centroids stabilize and the model converges. On the combined dataset, K-Means separated the data into four clusters, differentiating patterns associated with intact concrete, suspected delamination, and transitional conditions. The algorithm was applied to the whole dataset, and the resulting labels were linked back to individual bridges.

DBSCAN

DBSCAN identifies clusters based on the local density and uses two key parameters: (1) epsilon, ε, which defines the radius of the neighborhood around each point; and (2) minPts, the minimum number of points required to form a dense region. A point is considered a core point if it has at least minPts points within its ε-neighborhood. Points not reachable from any core point are labeled as noise or outliers. DBSCAN is particularly effective for detecting clusters of arbitrary shapes and for handling datasets with noise or spatial variability, such as those found in GPR and IE scanning. However, its performance is highly dependent on selecting appropriate values for ε and minPts.

In this study, DBSCAN was applied to the combined GPR and IE dataset (TWTT, amplitude, and IE frequency) from the eight bridges to identify dense regions in feature space and detect potential outliers. The ε and minPts were tuned through trial and error, guided by the observed density distribution in the dataset. The goal was to isolate densely packed regions corresponding to potential defect zones while minimizing the impact of sparsely distributed noise points. The neighborhood function used by DBSCAN is defined in Eq. (3):[29]

$$\begin{aligned} \text{Neighbor}\,(x_i, \varepsilon) &= \left\{x_j || x_i - x_j| \le \varepsilon\right\} \left(x_i, \varepsilon\right) \\ &= \left\{x_j || x_i - x_j| \le \varepsilon \right. \end{aligned} \tag{3}$$

where x_i and $x_j =$ are the data points, $\|x_i - x_i\|$ is the Euclidean distance between them, and a a point x_i is a core point if |Neighbor (x_i, ε) | ≥ minPts.

GMM

GMM assumes that the dataset is generated from a mixture of multiple Gaussian distributions, where each distribution represents a potential cluster. Unlike K-Means, which exclusively allocates each data point to one cluster, GMM adopts a probabilistic approach, assigning each point a degree of membership across all clusters. This flexibility makes GMM especially effective in situations where cluster boundaries are not well separated. GMM uses the Expectation-Maximization (EM) algorithm, which iteratively refines the model parameters—mean vectors (μ_k),

covariance matrices (Σ_k), and mixture weights (k)—to maximize the likelihood of the observed data. During the Expectation step, the model estimates the responsibility that each Gaussian component takes for each data point. In the Maximization step, these responsibilities are used to update the model parameters until convergence.

In this study, GMM was applied to the combined GPR and IE dataset from the eight bridges. The number of Gaussian components (k = 4) was determined based on the BIC, which balances model fit with complexity. The log-likelihood function maximized by the EM algorithm is given by Eq. (4):[30]

$$\mathcal{L}(\theta) = \prod_{i=1}^{N} \sum_{k=1}^{K} \pi_k N(x_i|\mu_k, \Sigma_k) \tag{4}$$

where $\mathcal{L}(\theta)$ is the likelihood of the observed data, π_k is the weight of the kth Gaussian component, $N(x_i|\mu_k, \Sigma_k)$ is the Gaussian probability density function, with mean μ_k and covariance Σ_k, $x_i =$ is the ith data point, and μ_k and Σ_k the parameters of the kth Gaussian.

FCMs

FCM is a variation of K-Means clustering that allows each data point to belong to multiple clusters with varying degrees of membership. Instead of assigning a point to a single cluster, FCM calculates a membership grade that indicates the degree of association between each data point and every cluster. The objective of FCM is to minimize the weighted sum of distances between each point and the cluster centroids, with each point's contribution to the objective function being weighted by its membership grade. The objective function for FCM is given in Eq. (5)[43]

$$J_m = \sum_{i=1}^{N} \sum_{j=1}^{C} u_{ij}^m ||x_i - C_j||^2 \tag{5}$$

where N is the number of data points, C the number of clusters, u_{ij} the membership grade of data point x_i in cluster c_j, and m is the fuzziness parameter (usually set to 2).

In this study, FCM was applied to the combined GPR and IE dataset (TWTT, amplitude, IE frequency) of the eight bridges. The fuzziness parameter m was set to 2, and the number of clusters was fixed at k = 4 based on prior evaluation criteria.

Results and Discussion

Clustering performance evaluation

The quality of the clustering results was first assessed to ensure they are technically sound and meaningful. Table 2 summarizes the Silhouette Scores and Davies–Bouldin Indices for each algorithm. The former measures how well points fit within their assigned cluster compared to others; higher scores indicate better-defined clusters. The latter measures the average similarity between each cluster and its most similar cluster, with lower values indicating better separation.

Among the algorithms, DBSCAN resulted in the highest Silhouette Score (0.98), reflecting its ability to form tight and dense clusters. However, since it focuses only on dense regions and labels many points as noise, it was less suitable for mapping global bridge deck conditions. Approximately 18% of the data points were considered as noise and excluded from the Silhouette Score calculation, contributing to the high value reported. Due to this limitation, DBSCAN was not used to generate the condition maps.

To ensure complete spatial coverage, K-Means clustering was selected for visualization purposes, as it assigns all data points to clusters and ensures full spatial coverage of the bridge decks. This makes K-Means more appropriate for interpreting overall condition trends across the bridge decks. FCM achieved the lowest Davies–Bouldin Index (0.82), indicating good separation between clusters and smooth transitions across boundaries. Together, these performance metrics validate the robustness of the clustering approaches and justify their application in subsequent condition analysis. The clustering results from DBSCAN, GMM, and FCM were used to validate the consistency of severity zone identification across methods. Despite algorithmic differences, key patterns were consistently observed. Cluster 1 corresponded to areas of severe deterioration, and Cluster 4 indicated sound concrete. This cross-method agreement reinforces the robustness of the K-Means-based condition maps used in the final analysis.

Cluster labeling and interpretation

After confirming their performance, the clusters were analyzed and interpreted to relate them to the physical conditions of the bridge decks. Each cluster generated by the different algorithms was examined in the context of its defining features, and the following interpretations were derived:

1. Cluster 1 (mixed amplitude and TWTT, high-frequency variability): This cluster exhibited signal variability in both GPR and IE data, reflecting heterogeneous rebar condition. Such variability is often associated with localized corrosion, differences in moisture content, or partial delamination. These patterns align with findings on bridge decks affected by progressive deterioration and corrosion.[1,44,45,21]
2. Cluster 2 (low amplitude, high TWTT, low frequency): The low amplitude and high TWTT indicate areas of the bridge decks where there might be voids or delaminations, and rebars are located at greater depths. These regions were marked as potential delamination zones.[46] Though standard IE theory predicts that shallower delamination should yield higher resonant frequencies, several field and lab studies reported that shallow delamination in in-service concrete decks often corresponds to lower IE frequencies.[47,48,26] This is likely due to energy loss, poor bonding at the delaminated interface, and wave scattering, which affect the dominant frequency response.

Table 2. Clustering evaluation metrics and scores

Metrices	K-Means	DBSCAN	GMM	FCM
Silhouette Score	0.72	0.98	0.93	0.96
Davies–Bouldin Index	0.85	0.97	0.95	0.82

Table 3. Summary of cluster labels

Cluster no.	Condition
1	Corrosion-prone/deteriorating areas
2	Potential delamination
3	Sound but shallow rebar
4	Well-bonded concrete

3. Cluster 3 (high amplitude, very low TWTT, high frequency): The high GPR amplitude and very low TWTT point to minimal signal attenuation and minimal concrete cover. Concurrently, high IE frequency responses are indicative of well-bonded, defect-free concrete. These zones may contain shallow rebars that could become exposed in the future, warranting periodic monitoring to ensure long-term durability.[49,24]
4. Cluster 4 (high amplitude, low TWTT, high frequency): High amplitude and low TWTT GPR data indicate dense and well-bonded concrete, characterizing regions with minimal subsurface defects or good quality concrete.[46,50] The corresponding high IE frequency further confirms the material integrity.

These interpretations link the cluster outputs to potential defect zones, rebar issues, or other conditions that may compromise the integrity of the bridges. These findings are summarized in Table 3, which groups the clusters based on their associated conditions.

By mapping the clustering results back to each bridge deck, distinct defect patterns were identified and compared across structures. Fig. 15 presents the proportion of each cluster across the eight bridges, clearly showing how different bridges exhibit distinct dominant condition patterns. For example, Bridge 1 primarily consisted of Cluster 4 (well-bonded concrete), suggesting generally good concrete quality, with scattered areas of Cluster 3 (sound but shallow rebar) and Cluster 1 (corrosion-prone), indicating localized shallow rebar and potential corrosion zones (Fig. 16). Bridge 2 exhibited a predominance of Cluster 3, highlighting areas in good condition but with a reduced rebar cover that warrant periodic monitoring (Fig. 17). In contrast, Bridge 3 was dominated by Cluster 1 (corrosion-prone), followed by noticeable occurrences of Cluster 2 (potential delamination) and a few areas of Cluster 3, indicating widespread deterioration across the deck (Fig. 18). Some clusters were absent or minimal on certain bridges, showing the ability of the clustering to reveal bridge-specific condition patterns. Such findings support the prioritization of inspections and maintenance, as inspectors can focus on bridges with higher proportions of damage-prone clusters, rather than treating all bridges equally.

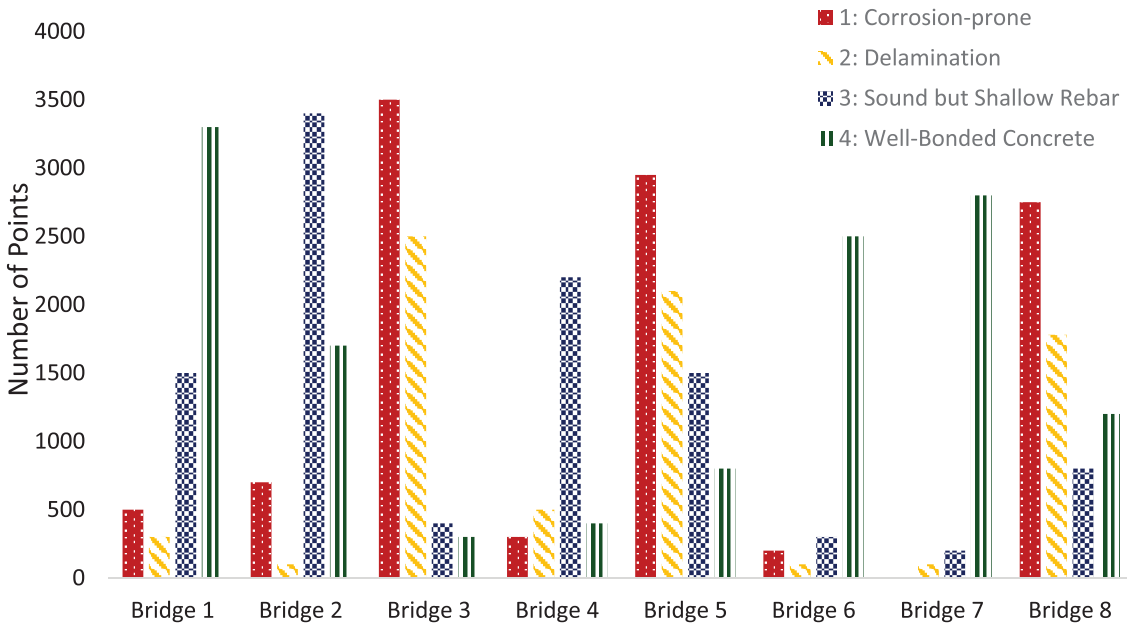

Figure 15. Distribution of clusters across bridges

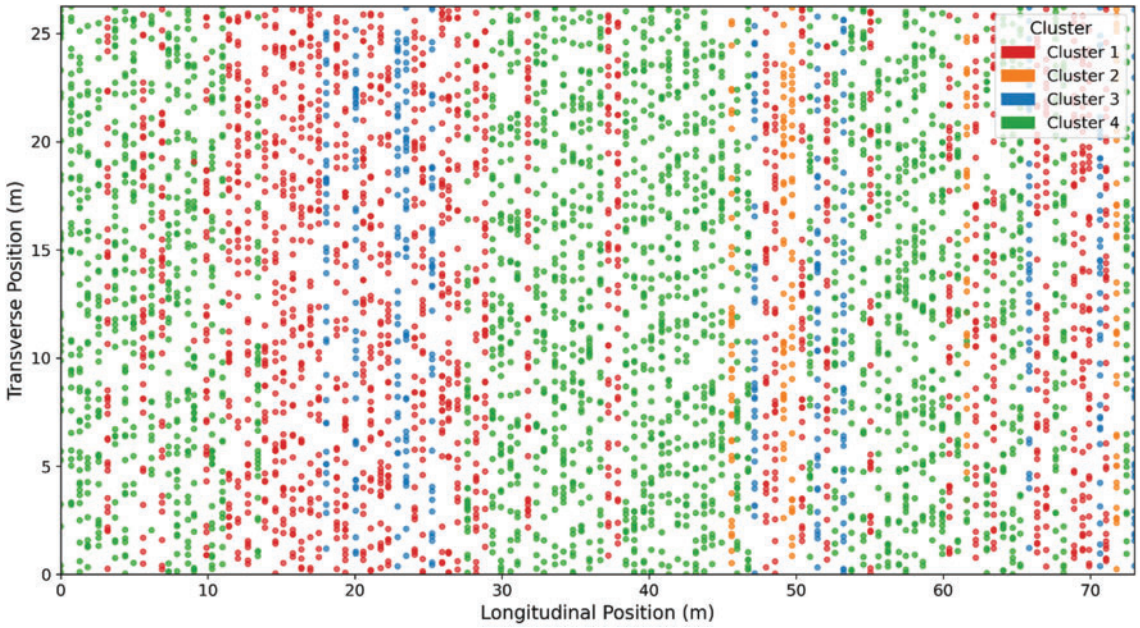

Figure 16. Spatial distribution of clusters for bridge 1

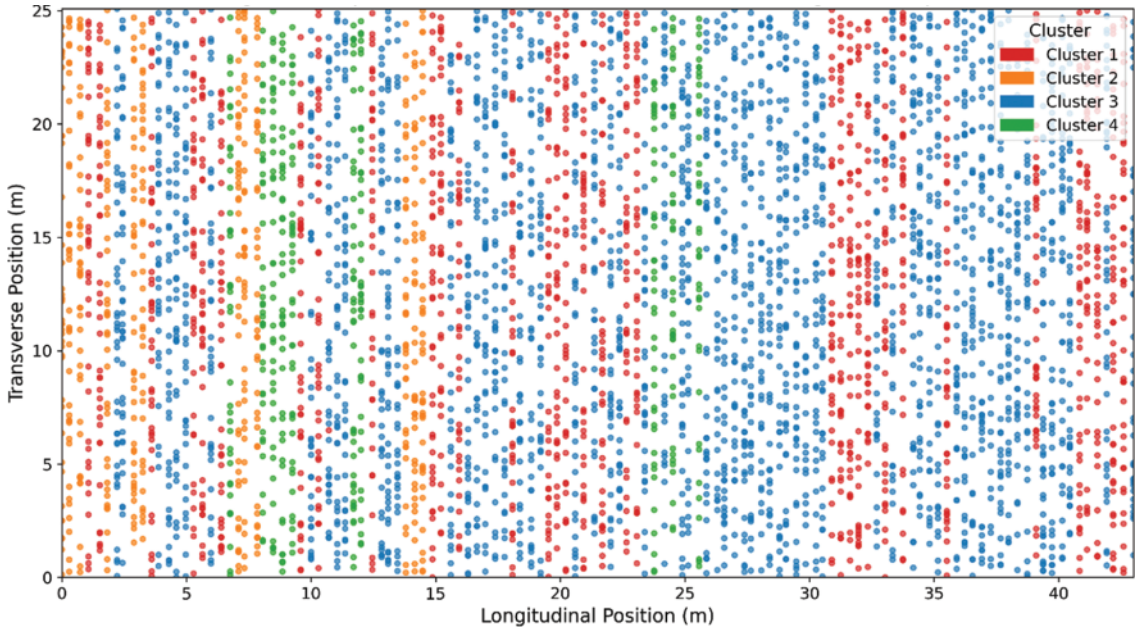

Figure 17. Spatial distribution of clusters for bridge 2

Figs. 16–18 illustrate the spatial distribution of clusters across the deck surfaces of Bridges 1, 2, and 3. These maps help engineers identify localized damage zones. Thus, instead of adopting similar maintenance strategies across the entire bridge deck, more attention may be given to areas most likely to exhibit damage and plan targeted maintenance, thereby improving efficiency and reducing costs.

The clustering approach offers a highly comprehensive and objective interpretation of bridge conditions, surpassing the limitations of traditional contour maps, which often focus on single features. By integrating multiple features and automatically classifying severity levels, clustering enables: (1) enhanced understanding of subsurface conditions; (2) Reduced reliance on subjective visual inspections; (3) targeted field investigations and cost-efficient maintenance; (4) integration into bridge management systems or GIS-based platforms; and (5) foundation for developing consistent condition ratings (e.g., fuzzy logic models). While the clustering framework successfully identified consistent deterioration patterns across eight bridges, most of these structures were relatively new (constructed within the past 10 to 15 years), with only two representing older bridge decks. As such, the generalizability of the four derived clusters to significantly older infrastructure remains uncertain. Bridge decks with long-term deterioration histories may exhibit different signal characteristics and degradation patterns. Therefore, direct

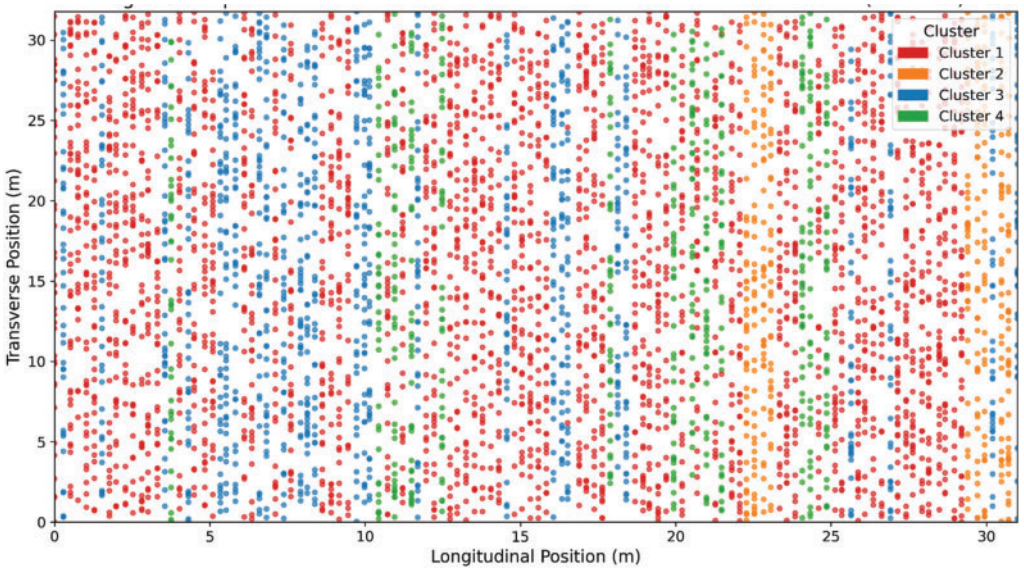

Figure 18. Spatial distribution of clusters for bridge 3

application of these cluster interpretations to older bridges without further validation should be carefully considered.

Conclusions

The following conclusions may be made based on the findings from this study:

1. The clustering-based framework successfully processed and fused GPR and IE data from eight bridges, enabling the automated identification of subsurface condition patterns.
2. By applying four unsupervised clustering algorithms (K-Means, DBSCAN, GMMs, and FCMs), the study successfully identified meaningful subsurface defect patterns.
3. The DBSCAN framework resulted in the highest Silhouette Score (0.98), while FCM recorded the lowest Davies–Bouldin Index (0.82), demonstrating the effectiveness of clustering techniques in identifying distinct defect zones.
4. Four consistent clusters were identified: Cluster 1 (corrosion-prone), Cluster 2 (delamination), Cluster 3 (shallow rebar), and Cluster 4 (well-bonded concrete), with repeatable interpretation across algorithms.
5. Cluster mapping enabled clear visualization of damage zones and supported targeted maintenance planning, surpassing traditional evaluation methods.
6. The spatial distribution of clusters reflected real-world deterioration trends: older bridges exhibited more severe defects, while newer bridges showed predominantly intact concrete.
7. Clustering enhances bridge condition assessments by supplementing visual inspections with objective subsurface data, improving reliability and reducing subjectivity.
8. The framework supports standardization in bridge deck evaluation, offering a scalable tool for DOTs to implement data-driven, transparent decision-making processes.

Recommendations for follow-up work

1. Incorporate the clustered condition labels into fuzzy inference systems or bridge condition rating models to support objective scoring.
2. Expand the dataset by applying the framework to a broader range of bridge types and geographical regions to assess its generalizability.
3. Integrate additional NDE techniques such as half-cell potential or ultrasonic pulse velocity to improve the classification of overlapping or uncertain defects.
4. Embed the clustering framework into GIS platforms to support real-time visualization, condition monitoring, and proactive maintenance scheduling.
5. Conduct periodic scans of bridges over time to explore how clustered patterns evolve, enabling predictive deterioration modeling and lifecycle management.
6. External validation through coring was not feasible for this study due to restrictions on destructive testing of in-service bridges. Instead, the cluster interpretations were guided by known signal behaviors in TWTT, amplitude, and IE frequency, and were consistent with deterioration mechanisms reported in prior studies.[1,46,45] The observed alignment between clustering results and expected field conditions, such as more severe clusters on older decks, supports the reliability of the findings. Future research should incorporate selective destructive or semi-destructive testing to directly confirm subsurface defect states and further validate the clustering predictions.
7. Future research should apply the clustering framework to older bridge decks with more advanced deterioration to evaluate whether the identified cluster patterns

remain consistent across different bridge ages and condition states.

Data availability statement

The data presented in this study are available on request from the corresponding author.

References

[1] Gucunski N, Imani A, Romero F, et al. *Nondestructive Testing to Identify Concrete Bridge Deck Deterioration (SHRP 2 Report S2-R06A-RR-1)*. Transportation Research Board; 2013. doi:10.17226/22771.

[2] American Society of Civil Engineers. *2021 Report Card for America's America's Infrastructure: A Comprehensive Assessment of America's America's Infrastructure (Executive Summary)*. Reston, VA: American Society of Civil Engineers; 2021. https://infrastructurereportcard.org.

[3] Federal Highway Administration (FHWA). *Recording and Coding Guide for the Structure Inventory and Appraisal of the Nation's Bridges* (Report No. FHWA-PD-96-001). U.S. Department of Transportation; 2021. Retrieved from: https://www.fhwa.dot.gov/bridge/mtguide.pdf.

[4] Washer GA, Fuchs PA. Developments in the use of infrared thermography for the condition assessment of concrete. *Proceedings of the International Symposium on Non-Destructive Testing in Civil Engineering (NDT-CE)*; 2015; Berlin, Germany.

[5] Dinh K, Zayed T. GPR-based fuzzy model for bridge deck corrosiveness index. *J Perform Const Facil*. 2015; 29(4):04014101. doi:10.1061/(ASCE)CF.1943-5509.0000815.

[6] Federal Highway Administration. *Improving Bridge Performance with Nondestructive Evaluation Technologies (Report No. FHWA-HRT-25-009)*. McLean, VA: U.S. Department of Transportation, Federal Highway Administration, Turner-Fairbank Highway Research Center; 2024. https://highways.dot.gov/sites/fhwa.dot.gov/files/FHWA-HRT-25-009.pdf.

[7] Omar T, Nehdi ML. Condition assessment of reinforced concrete bridges: current practice and research challenges. *Infrastructures*. 2018;3(3):36. doi:10.3390/infrastructures 3030036.

[8] Gucunski N, Pailes BM, Kim J, Azari H, Dinh K. Capture and quantification of deterioration progression in concrete bridge decks through periodical NDE surveys. *J Infrastruct Syst*. 2017;23(1):04016029. doi:10.1061/(ASCE) IS.1943-555X.0000321.

[9] Gucunski N, Romero F, Kruschwitz S, Feldmann R, Parvardeh H. *Comprehensive Bridge Deck Deterioration Mapping of Nine Bridges by Nondestructive Evaluation Technologies (Final Report)*. Rutgers, The State University of New Jersey, Center for Advanced Infrastructure and Transportation; 2011.

[10] Gucunski N, Romero F, Kruschwitz S, Feldmann R, Abu-Hawash A, Dunn M. Multiple complementary nondestructive evaluation technologies for condition assessment of concrete bridge decks. *Transport Res Rec: J Transport Res Board*. 2010;2201(1):34–44. doi:10.3141/2201-05.

[11] Hugenschmidt J, Mastrangelo R. GPR inspection of concrete bridges. *Cem Concr Compos*. 2006;28(4):384–392. doi:10.1016/j.cemconcomp.2006.02.016.

[12] Brown MC, ElBatanouny M, Bektaş B, Azari H, Foden AJ, Imani A, et al. *Incorporating Nondestructive Evaluation Methods into Bridge Deck Preservation Strategies (FHWA Publication No. FHWA-HRT-24-186)*. McLean, VA: U.S. Department of Transportation, Federal Highway Administration, Turner-Fairbank Highway Research Center; 2024. doi:10.21949/1521524.

[13] Scherr J, Grosse C. Delamination detection on a concrete bridge deck using impact echo scanning. *Struct Concr*. 2021;22(2):806–812. doi:10.1002/suco.202000415.

[14] American Society for Testing and Materials (ASTM). *ASTM D6432-19: Standard Guide for Using the Surface Ground Penetrating Radar Method for Subsurface Investigation*. West Conshohocken, PA: ASTM International; 2019. doi:10.1520/D6432-19.

[15] Geophysical Survey Systems, Inc. (GSSI). *Concrete HandBook: GPR Inspection of Concrete (MN72-367 Rev. H)*. Nashua, NH: Geophysical Survey Systems, Inc.; 2017.

[16] Hasan MI, Yazdani N. Ground penetrating radar utilization in exploring inadequate concrete covers in a new bridge deck. *Case Stud Construct Mat*. 2014;1:104–114. doi:10.1016/j.cscm.2014.04.003.

[17] Hugenschmidt J. Concrete bridge inspection with a mobile GPR system. *Construct Build Mat*. 2002;16(3):147–154. doi:10.1016/S0950-0618(02)00003-4.

[18] Gagarin N, Goulias D, Mekemson J. Condition rating of bridge decks with fuzzy sets modeling for SF-GPR surveys. *Remote Sens*. 2023;15(14):3631. doi:10.3390/rs15143631.

[19] Ibrahim A, Abdelkhalek S, Zayed T, Qureshi AH, Abdelkader EM. A comprehensive review of the key deterioration factors of concrete bridge decks. *Buildings*. 2024;14(11):3425. doi:10.3390/buildings14113425.

[20] La HM, Gucunski N, Kee SH, Nguyen LV. Data analysis and visualization for the bridge deck inspection and evaluation robotic system. *Visualizat Eng*. 2015;3(1):6. doi:10.1186/s40327-015-0017-3.

[21] Mohamadi S, Lattanzi D, Azari H. Fusion and visualization of bridge deck nondestructive evaluation data via machine learning. *Front Mat*. 2020;7:576918. doi:10.3389/fmats.2020.576918.

[22] Python Software Foundation. *Python Language Reference, version 3.12.2*; 2024. https://www.python.org.

[23] Yoon Y-G, Kim C-M, Oh T-K. A study on the applicability of the impact-echo test using semi-supervised learning based on dynamic preconditions. *Sensors*. 2022;22:5484. doi:10.3390/s22155484.

[24] Zhang Y, Yin E, Li F, et al. Hierarchical feature fusion framework for frequency recognition in SSVEP-based BCIs. *Neur Netw*. 2019;119:1–9.

[25] Hoxha E, Feng J, Sanakov D, Gjinofci A, & Xiao J. Robotic inspection and characterization of subsurface defects on concrete structures using impact sounding. arXiv preprint arXiv:2208.06305; 2022.

[26] Jafari F, Dorafshan S. Comparison between supervised and unsupervised learning for autonomous delamination detection using impact echo. *Remote Sensing*. 2022;14(24):6307. doi:10.3390/rs14246307.

[27] Völker C, Shokouhi P. Clustering based multi sensor data fusion for honeycomb detection in concrete. *J Nondestruct Evaluat*. 2015;34(4):32. doi:10.1007/s10921-015-0307-7.

[28] Jain AK. Data clustering: 50 years beyond K-means. *Pattern Recognit Lett*. 2010;31(8):651–666. doi:10.1016/j.patrec.2009.09.011.

[29] Schubert E, Sander J, Ester M, Kriegel HP, Xu X. DBSCAN revisited, revisited: Why and how you should (still) use DBSCAN. *ACM Transact Database Syst*. 2017;42(3):1–21. doi:10.1145/3068335.

[30] Reynolds DA. Gaussian mixture models. In: Li SZ. (Ed.), *Encyclopedia of Biometrics*. Springer; 2015:827–832. doi: 10.1007/978-1-4899-7488-4_196.

[31] Fang F, Ouyang L, Meng Y, Xu Q, Chen J, Qiu L. Structural adaptive damage detection under uncertainty based on probability dissimilarity and moving average control chart. *Measurement*. 2024;225(1):114023. doi:10.1016/j.measurement.2023.114023.

[32] Pedram M, Taylor S, Hamill G, Robinson D. Quantification of subsurface defects in reinforced concrete of bridges by unsupervised segmentation of IR images. In: *Proceedings of the IABSE Symposium Istanbul 2023: Long Span Bridges*. Istanbul, Turkey: International Association for Bridge and Structural Engineering (IABSE); 2023:835–845. doi: 10.2749/istanbul.2023.0835.

[33] Omar T, Nehdi ML. Remote sensing of concrete bridge decks using unmanned aerial vehicle infrared thermography. *Automat Construct*. 2017;83(11):360–371. doi:10.1016/j.autcon.2017.06.024.

[34] Liu H, Zhang Y. Bridge condition rating data modeling using deep learning algorithm. *Struct Infrastruct Eng*. 2020;16(2):1–14. doi:10.1080/15732479.2020.1712610.

[35] Solla M, Fernández N, Elseicy A, Pais J. Clustering approach for crack detection in GPR data: influence of infilling material on detectability. *Case Stud Construct Mat*. 2025;22(10):e04782. doi:10.1016/j.cscm.2025.e04782.

[36] Han J, Kamber M, Pei J. *Data Mining: Concepts and Techniques*. 3rd ed. Burlington, MA: Morgan Kaufmann; 2011. doi:10.1016/C2009-0-61819-5.

[37] Zhou F, Chen Z, Liu H, Cui J, Spencer BF, & Fang G. Simultaneous estimation of rebar diameter and cover thickness by a GPR-EMI dual sensor. *Sensors*. 2018;18(9):2969. doi:10.3390/s18092969.

[38] Cotič P, Niederleithinger E, Stoppel M. *Unsupervised Fusion of Scattered Data Collected by a Multi-Sensor Robot on Concrete*. BAM, Berlin: GZfP-Jahrestagung 2014–Di.2.C.1; 2014.

[39] Pashoutani S, Zhu J, Sim C, Ramseyer C. Multi-sensor data collection and fusion using autoencoders in condition evaluation of concrete bridge decks. *J Infrastruct Preservat Resil*. 2021;2(1):18. doi:10.1186/s43065-021-00032-3.

[40] Lu GY, Wong DW. An adaptive inverse-distance weighting spatial interpolation technique. *Comput Geosci*. 2008;34(9):1044–1055. doi:10.1016/j.cageo.2007.07.010.

[41] Jiao Y, Liu H, Zhang P, Wang X, & Wei H. Unsupervised performance evaluation strategy for bridge superstructure based on fuzzy clustering and field data. *J Perform Constr*. 2020. doi:10.1061/(ASCE)CF.1943-5509.0001455.

[42] Sasmal S, Ramanjaneyulu K, & Gopalakrishnan S. Fuzzy logic-based condition rating of existing reinforced concrete bridges. *J Perform Constr Facil*. 2006;20(3):261–273. doi:10.1061/(ASCE)0887-3828(2006)20:3(261).

[43] Chang S-C, Chuang W-C, Jeng J-T. New interval improved fuzzy partitions fuzzy C-means clustering algorithms under different distance measures for symbolic interval data analysis. *Appl Sci*. 2023;13(22):12531. doi:10.3390/app132212531.

[44] Marzorati S, Todaro R, Cocco G, & Guadagnini M. Fusion and visualization of bridge deck nondestructive evaluation data for corrosion assessment. *Materials*. 2020;13(24):5769. doi:10.3390/ma13245769.

[45] Faris N, Zayed T, Abdelkader EM, Fares A. Corrosion assessment using ground penetrating radar in reinforced concrete structures: influential factors and analysis methods. *Automat Construct*. 2023;158:105130. doi:10.1016/j.autcon.2023.105130.

[46] Dinh K, Gucunski N, Kim J, Duong TH. Understanding depth–amplitude effects in assessment of GPR data from concrete bridge decks. *NDT & E Int*. 2016;83(2):48–58. doi:10.1016/j.ndteint.2016.06.004.

[47] Gucunski N, Imani A, Romero F, Kruschwitz S. Automated impact echo testing of concrete bridge decks: towards faster and more objective evaluations. In: *Transportation Research Board 94th Annual Meeting Compendium of Papers*. Washington, DC: Transportation Research Board; 2015.

[48] Momo MM. *Quantifying Shallow Depth Concrete Delaminations Using Impact Echo*. Master's thesis. The University of Texas at Arlington; 2020. https://rc.library.uta.edu/uta-ir/handle/10106/29606.

[49] Pashoutani S, Zhu J. Real depth-correction in ground penetrating radar data analysis for bridge deck evaluation. *Sensors*. 2023;23(2):1027. doi:10.3390/s23021027.

[50] Sengupta A, Guler SI, Shokouhi P. Interpreting impact echo data to predict condition rating of concrete bridge decks: a machine-learning approach. *J Bridge Eng*. 2021; 26(8):04021054. doi:10.1061/(ASCE)BE.1943-5592.0001744.

BER the international journal of bridge engineering management and research

Influence of Nose Position of Edge Fairing on Aerodynamic Characteristics of Box-Girder Bridge Deck

Md. Naimul Haque[1,*]; Hiroshi Katsuchi[2]; and Md. Basir Zisan[3]

Submitted: 10 June 2025 **Accepted:** 24 August 2025 **Publication date:** 10 October 2025

DOI: 10.70465/ber.v2i4.43

Abstract: Edge fairing is often applied to box-girder bridge decks to improve their aerodynamic performance, particularly in long-span bridges. A thorough understanding of the aerodynamic response and flow behavior of bridge decks with edge fairings is essential for optimal design and ensuring wind-induced safety. This study presents a numerical investigation into the influence of the nose position of edge fairings on the aerodynamic behavior of box-girder bridge decks. Two-dimensional unsteady Reynolds-averaged Navier–Stokes (URANS) simulations were performed using the *k-ω-SST* turbulence model, supported by appropriate validation studies. Both static and dynamic simulations were conducted for two configurations: edge fairings with nose-up and nose-down positions. The static analysis showed that the nose-down configuration offered superior aerodynamic performance compared to the nose-up configuration. In the nose-down position, the deck experienced reduced static wind forces with smaller fluctuations. The dynamic simulations further revealed that the nose-down fairing configuration has improved aerodynamic damping in both torsional and heaving modes. In particular, leading-edge flow reattachment was identified as the primary contributor to enhanced aerodynamic damping in the nose-down configuration. Further, the relatively larger bottom plate slope had better aeroelastic responses in the nose-down position of the edge fairing.

Author keywords: aerodynamic response; box girder; fairing; nose location; CFD; unsteady RANS; flutter derivatives; damping

Introduction

Long-span cable-supported bridges are often favored by engineers to provide wide navigation clearances. However, as the span length increases, the bridge deck becomes more flexible, raising concerns about its aeroelastic performance. To improve the aerodynamic behavior of long-span bridges, various aerodynamic countermeasures are applied to the deck. Among these, edge fairings are one of the most common and effective methods. They are used to reduce along-wind loads and suppress after-body vortex shedding, as seen in bridges such as the Deer Isle (USA), Bronx–Whitestone (USA), Hakucho (Japan), and Tempozan (Japan).

In the case of edge fairings, several shaping parameters significantly influence aerodynamic performance, including the top plate slope (θ_T), bottom plate slope (θ_B), and nose location (h/D), as illustrated in Fig. 1. Previous studies[1–3] have shown that the aerodynamic response is highly sensitive to the shape of the fairing. These studies primarily focused on experimental investigations of θ_T and θ_B, using a limited number of shape combinations due to the high cost of testing. While these efforts demonstrated the effectiveness of edge fairings in enhancing aerodynamic performance, they did not provide definitive recommendations for fairing shape design.

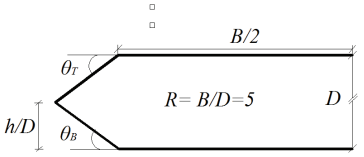

Figure 1. Geometric configuration and important shaping parameters of the considered bridge deck

Later, Haque et al.[4] conducted a comprehensive numerical study exploring a wider range of θ_T and θ_B values. They found that, for a specific range of bottom plate slopes (θ_B), the bridge deck exhibited reduced aerodynamic responses. Their study also suggested that the nose location (h/D) influences aerodynamic behavior, but its effects were not fully clarified. Interestingly, a fairing with a given combination of θ_T and θ_B can be installed either in the lower or upper half

*Corresponding Author: Md. Naimul Haque.
Email: naimul@ewubd.edu
[1]Department of Civil Engineering, East West University, Aftabnagar, Dhaka-1212, Bangladesh
[2]Department of Civil Engineering, Yokohama National University, Yokohama 240-8501, Japan
[3]Department of Civil Engineering, Chittagong University of Engineering and Technology, Raojan, Chittagong-4349, Bangladesh

Discussion period open till six months from the publication date. Please submit separate discussion for each individual paper. This paper is a part of the Vol. 2 of the International Journal of Bridge Engineering, Management and Research (BER), ISSN 3065-0569.

of the deck, referred to hereafter as the "nose-down" and "nose-up" configurations, respectively, as shown in Fig. 2. Therefore, in addition to θ_T and θ_B, the nose location (h/D) should be investigated in detail, as it may lead to practical recommendations for shaping edge fairings and optimizing bridge deck geometry. Thereafter, another study by Haque et al.[5] showed that the mean static force coefficients of bridge decks are sensitive to the nose location of the edge fairing. However, many aspects remain unexplored. In particular, the impact of nose location on the flow field and dynamic responses of the deck needs further investigation to support the design process of bridge geometries.

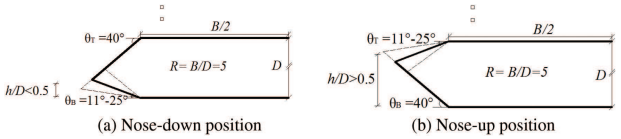

Figure 2. Considered shapes of the edge fairing and the influence of nose position (h/D) on the geometric configuration of the bridge deck

Recently, computational fluid dynamics (CFD) has become a popular and effective tool in various fields of engineering, including bridge and bluff body aerodynamics, due to its balance of accuracy and computational efficiency. The unsteady Reynolds-averaged Navier–Stokes (URANS) approach offers moderate accuracy with high efficiency. Several researchers have validated its performance and reliability,[6–16] with successful applications in the field of bridge aerodynamics.[4,6–8,16–18]

Against this background, the present study investigates the influence of the nose location (h/D) of edge fairings on the aerodynamic performance of a closed box-girder bridge deck using CFD. Two-dimensional URANS simulations employing the *k-ω-SST* turbulence model were conducted to analyze both steady-state and dynamic aerodynamic responses, as well as the associated flow fields. A comparative analysis was performed for fairings in the nose-up ($h/D > 0.5$) and nose-down ($h/D < 0.5$) configurations. For both configurations, the top (θ_T) and bottom (θ_B) plate slopes were varied from 11° to 25°, as shown in Fig. 2. Initially, force coefficients and flow field characteristics, such as pressure and velocity distributions, were examined in detail to understand the underlying aerodynamic behavior. Subsequently, for a selected fairing shape, flutter derivatives were computed to assess the influence of nose location (h/D) on the dynamic characteristics of the bridge deck. All simulations were conducted at a Reynolds number (Re) of 1.2×10^4.

Numerical Procedure

The URANS equations were used to model the flow around the bridge deck. Flow was assumed to be two-dimensional and incompressible in nature. The governing equations are as follows:

$$\frac{\partial \overline{U}_i}{\partial x_i} = 0 \tag{1}$$

$$\frac{\partial \overline{U}_i}{\partial t} + \overline{U}_j \frac{\partial \overline{U}_i}{\partial x_j} = -\frac{1}{\rho}\frac{\partial \overline{P}}{\partial x_i} + \frac{\partial}{\partial x_j}\left[\nu\left(\frac{\partial \overline{U}_i}{\partial x_j} + \frac{\partial \overline{U}_j}{\partial x_i}\right) - \left(\overline{u_i' u_j'}\right)\right] \tag{2}$$

where $\overline{U}_i$ and x_i are the averaged velocity and position vectors, respectively, t is the time, $\overline{P}$ is the averaged pressure, ρ is the air density, and ν is the fluid viscosity. Due to the time-averaging process, a new variable $\overline{u_i' u_j'}$ appeared, known as Reynolds stress, which needs modeling to close the equation, a process known as turbulence modeling. Turbulence modeling was attained by *k-ω-SST*, a two-equation turbulence model.[19]

A forced vibration dynamic simulation was also conducted to extract the flutter derivatives. In these simulations, the motion of the bridge deck boundaries was modeled by adapting the computational grid, implemented through the arbitrary Lagrangian–Eulerian formulation of the URANS equations.[20,21] This approach allowed the mesh to move with the oscillating structure, capturing the fluid–structure interaction more accurately. As a result, the governing equations were modified accordingly

$$\frac{\partial \left(\overline{U}_i - \overline{U}_{gi}\right)}{\partial x_i} = 0 \tag{3}$$

$$\frac{\partial \overline{U}_i}{\partial t} + \overline{U}_j \frac{\partial \left(\overline{U}_i - \overline{U}_{gi}\right)}{\partial x_j} = -\frac{1}{\rho}\frac{\partial \overline{P}}{\partial x_i} + \frac{\partial}{\partial x_j}\left[\nu\left(\frac{\partial \overline{U}_i}{\partial x_j} + \frac{\partial \overline{U}_j}{\partial x_i}\right) - \left(\overline{u_i' u_j'}\right)\right] \tag{4}$$

where $\overline{U}_{gi}$ is the grid velocity in the ith direction.

All the governing equations described above were discretized using the finite volume method, and the open-source CFD software OpenFOAM was used as the solver. The convective and diffusive terms in the governing equations were discretized using second-order accurate central differencing schemes. For time integration, the second-order accurate backward differentiation formula method was employed. The PISO (Pressure Implicit with Splitting of Operator) algorithm was used to solve the discretized equations. During the dynamic simulations, the pressure–velocity coupling was achieved using the PIMPLE (Pressure Implicit with Momentum Prediction and Localized Enrichment) algorithm, a hybrid of the PISO and SIMPLE (Semi-Implicit Method for Pressure-Linked Equations) methods, offering improved stability and convergence for transient simulations. To ensure numerical stability, the maximum Courant number (C_o) was maintained well below 1 throughout the simulations.

The computational domain size and mesh layout are illustrated in Fig. 3. The domain size was chosen based on recommendations from previous studies and validated in[16,22]. It was made sufficiently large to minimize boundary interference with the flow field. A no-slip boundary condition ($\partial u/\partial y \neq 0$, $v = 0$) was applied on the bridge deck surface. At the domain inlet, a Dirichlet boundary condition

was applied for velocity ($u = U$, $v = 0$), and a Neumann condition ($\partial p/\partial n = 0$) was used for pressure. At the outlet, Neumann conditions were applied for velocity, and Dirichlet conditions for pressure. Slip boundary conditions ($\partial u/\partial y = 0$, $v = 0$) were applied at the top and bottom boundaries of the domain.

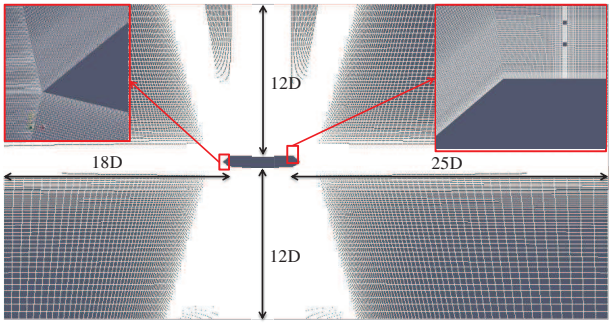

Figure 3. Meshing details of the bridge deck section. All the dimensions are normalized with the height of the bridge deck (D)

A body-fitted structured grid system was used for spatial discretization, as shown in Fig. 3. The first grid height (y) normal to the deck surface was selected such that the wall-adjacent cells remained within the viscous sub-layer ($y^+ \leq 5$). Grid spacing was gradually increased away from the surface using a constant growth factor of 1.05 in all directions. Overall, the bridge deck maintained an average y^+ value well below 5. Only in a small region near the leading edge corner of the top surface did the maximum y^+ slightly exceed 5. Since the primary objective of this study was to compare the relative aerodynamic responses of various deck shapes, maintaining a consistent grid resolution, particularly in terms of y^+ values, was essential for a valid comparison. Accordingly, all simulations ensured that the variation in y^+ values remained within approximately 5%, regardless of fairing shape variations.

Aerodynamic Analysis

In the static analysis, the main parameter of interest was the steady-state force coefficients. The steady-state force coefficients such as drag (C_D), lift (C_L), moment (C_M), and Strouhal number (S_t) were defined as follows:

$$C_D = \frac{F_D}{1/2\rho U^2 D} \text{ (downstream positive)} \tag{5}$$

$$C_L = \frac{F_L}{1/2\rho U^2 B} \text{ (upward positive)} \tag{6}$$

$$C_M = \frac{F_M}{1/2\rho U^2 B^2} \text{ (anticlockwise positive)} \tag{7}$$

$$S_t = \frac{fB}{U} \tag{8}$$

where F_D, F_L, and F_M are the drag, lift, and moment forces acting per unit length on the bridge deck, respectively, and f is the shedding frequency. Both the mean and root mean square (rms) values of the time-varying force coefficients were evaluated. In all cases, the rms values were calculated from the zero-mean force coefficient time histories.

The main goal of dynamic simulation is to extract the flutter derivatives to judge the aerodynamic characteristics of the bridge deck. The aerodynamic lift and moment forces are expressed by the following expression, as mentioned in Simiu and Scanlan:[23]

$$L(t) = \frac{1}{2}\cdot\rho\cdot U^2\cdot B_1\cdot\left[k\cdot H_1^*\cdot\frac{\dot{\eta}}{U} + k\cdot H_2^*\cdot B_1\cdot\frac{\dot{\alpha}}{U} + k^2\cdot H_3^*\cdot\alpha + k^2\cdot H_4^*\cdot\frac{\eta}{B_1}\right] \tag{9}$$

$$M(t) = \frac{1}{2}\cdot\rho\cdot U^2\cdot B_1^2\cdot\left[k\cdot A_1^*\cdot\frac{\dot{\eta}}{U} + k\cdot A_2^*\cdot B_1\cdot\frac{\dot{\alpha}}{U} + k^2\cdot A_3^*\cdot\alpha + k^2\cdot A_4^*\cdot\frac{\eta}{B_1}\right] \tag{10}$$

where $L(t)$ and $M(t)$ are the time-varying self-excited lift force and moment per unit span of the bridge deck, respectively; ρ is the air density; U is the mean wind speed; k is the reduced frequency, ($k = B_1.\omega/U$); ω is the circular frequency, ($2.\pi.f$); B_1 is the full width of the bridge deck; η is the heaving displacement; α is the torsional displacement; the dot ($\dot{}$) represents first time derivatives; and H_i^* and A_i^* are the aerodynamic coefficients known as flutter derivatives in heaving and torsional motions, respectively. The methodology to extract the flutter derivatives through forced vibration simulation was discussed in detail in previous numerical works;[9,12–15,24,25] hence, the discussion is not deepened here. The work done by the unsteady pressure provides an in-depth understanding of the complex fluid–structure interaction under torsional mode and was calculated by the following equation:

$$C_{PI}\cdot r = \left(\frac{x}{B_1}\right)\cdot|C_P(x)|\cdot Sin\,\varphi(x) \tag{11}$$

Here, r represents the normalized distance from the center of the bridge deck toward either side. The function $\varphi(x)$ denotes the phase difference between the maximum relative angle of attack of the bridge deck and the maximum negative pressure at a distance x from the deck center. $C_p(x)$ is the magnitude of the unsteady pressure, and C_{pi} is the imaginary component of the unsteady pressure. A positive value of the product $C_{pi}\cdot r$ indicates an excitation force acting at the leading edge of the top surface of the bridge deck, while a negative value indicates damping. At the trailing edge of the top surface, the sign convention is reversed. For the bottom surface of the deck, the sign convention is also reversed relative to the top surface, both at the leading and trailing edges.

The model was excited with a one degree of freedom torsional (α) motion of periodic vibration to extract the flutter derivatives. A torsional (α_o) amplitude of 1° was utilized. The reduced velocity (U/fB_1) was altered by changing the frequency of vibration (f_α) only. The heaving motion flutter derivatives were calculated from the interdependency

relationships among the flutter derivatives proposed by Matsumoto[26] to reduce time and computational cost. Previously, Tubin[27] also checked this type of interdependency relationship among the flutter derivatives experimentally and found very good compatibility for a streamlined bridge deck. Later, Nieto et al.[9] checked those relationships given by Tubin[27] numerically and recommended for further applicability to reduce the computational load due to their high efficiency.

Validation

The performance of the utilized numerical model and setup for simulating steady-state responses had already been checked previously.[4,16,18,22,25,28] However, in the present study, along with the steady-state response, the dynamic response, such as the flutter derivatives, was also taken into consideration. Therefore, the performance of the present numerical method should be checked for simulating dynamic responses such as the flutter derivatives around a bluff section.

We conducted the simulation for the rectangular cylinder with a side ratio (R) of 5. Normally, the rectangular cylinder experiences quite a large flow separation as compared to the bridge deck with fairing. Therefore, if the present numerical setup can reproduce the dynamic responses accurately for the rectangular cylinder of a side ratio (R) of 5, that would be sufficient for the considered bridge deck with fairing. Simulations were carried out at a Reynolds number (R_{eB}) of 5.0×10^4 with a torsional amplitude (α_o) of 1°.

The extracted flutter derivatives are presented in Fig. 4 and compared with the experimental results reported by Matsumoto.[26] A reasonable agreement can be observed between the present numerical results and the past experimental data. However, noticeable discrepancies are found in the flutter derivatives H_2^* and A_2^* when compared to other derivatives. Similar discrepancies have also been reported in previous studies,[7,9,13,29] suggesting this may be a common challenge in numerical–experimental comparisons. Despite these differences, the overall trends and general behavior of the flutter derivatives were accurately reproduced. Furthermore, the flutter derivatives for the heaving mode calculated using interdependency relationships also show good agreement with the experimental data, similar to the torsional mode derivatives.

In particular, as seen in Fig. 4, the present results show closer agreement with the flutter derivatives reported by Sarker et al.,[30] while some differences are observed between the results of Matsumoto[26] and Sarker et al.[30] themselves. Nonetheless, since the primary objective of this study is to perform a relative comparison of flutter derivatives across different bridge deck configurations, the level of accuracy achieved is sufficient to evaluate the influence of the nose location (h/D) on aerodynamic responses.

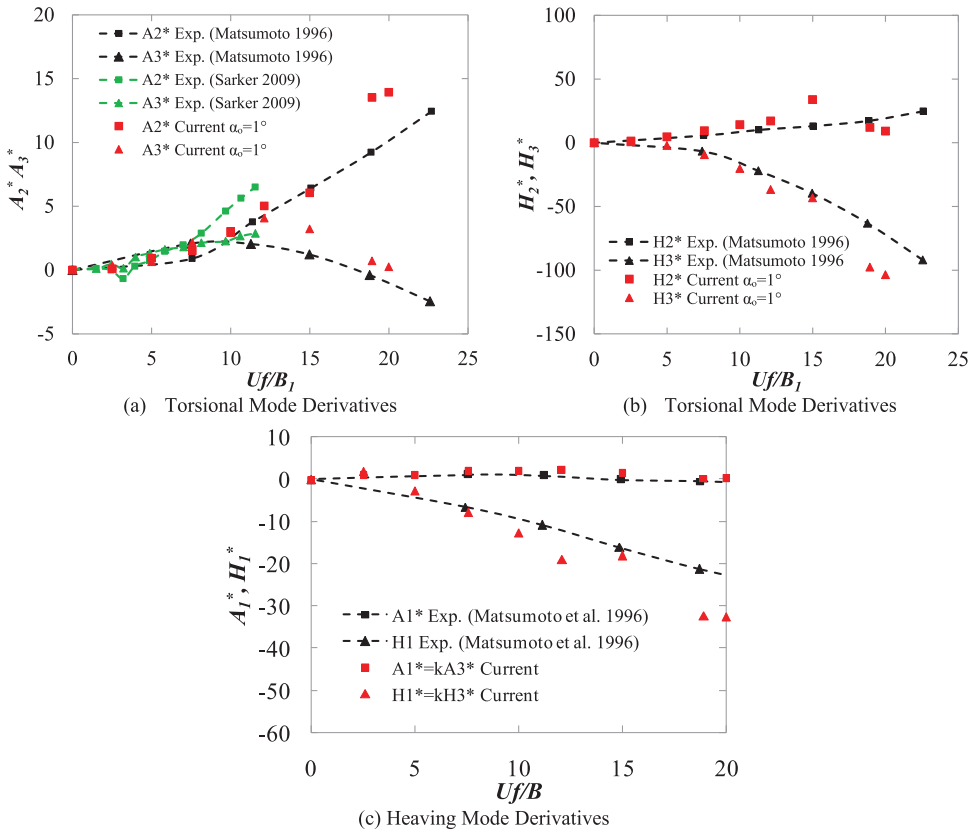

Figure 4. Important flutter derivatives of the rectangular cylinder having side ratio (R) of 5: (a, b) Calculated from the forced torsional oscillation and compared with the experimental results of Matsumoto[26] and Sarkar et al.[30] and (c) calculated from the interdependency relationships[26]

Steady-State Response

Steady-state force coefficient

Simulations were conducted for the bridge deck configurations shown in Fig. 2. In the nose-down configuration, the top plate slope (θ_T) was fixed at 40°, while the bottom plate slope (θ_B) was varied from 11° to 25°. Conversely, in the nose-up configuration, the bottom plate slope (θ_B) was fixed at 40°, and the top plate slope (θ_T) was varied within the same range (11°–25°).

Fig. 5 compares the mean values of static aerodynamic coefficients for these two configurations. The results clearly indicate that the nose location (h/D) has a significant influence on the steady-state force coefficients. For any given value of θ_T or θ_B, the fairing in the nose-down position consistently shows lower aerodynamic responses than that in the nose-up position. Both the mean drag coefficient (C_D) and the mean lift coefficient (C_L) demonstrate improved performance in the nose-down configuration, characterized by reduced drag and more favorable lift behavior. For the nose-down position, the bridge deck experiences a counterclockwise aerodynamic moment, whereas in the nose-up position, it experiences a clockwise moment. The magnitude of this moment increases as the plate slope decreases in both configurations. While the sign of the moment coefficient (C_M) has limited aerodynamic significance, the sign of the lift coefficient (C_L) is particularly important in bridge aerodynamics. A negative lift force (downward acting) is beneficial, as it increases cable tension and enhances the aerodynamic stability of the bridge deck. This effect is more pronounced in the nose-down configuration, indicating superior aerodynamic performance.

The rms values of the aerodynamic coefficients, which reflect the deck's dynamic response to wind excitation, are compared in Fig. 6. Similar to the mean values, the rms coefficients are generally lower for the nose-down configuration. As shown in Figs. 6a and 6b, for any value of θ_T or θ_B, the nose-down configuration exhibits slightly smaller fluctuations caused by after-body vortex shedding. The Strouhal number (S_t), which represents the vortex shedding frequency, exhibits comparatively lower sensitivity to changes in the nose location. However, for smaller plate slopes (θ_T or θ_B), the nose-down configuration shows higher Strouhal numbers, indicating a more streamlined behavior and a higher vortex shedding frequency.

This section has quantitatively discussed the influence of nose location (h/D) on the steady-state aerodynamic force coefficients. In the following section, a detailed analysis of the steady-state flow field is presented for a specific fairing shape, since the observed influence of nose location on force coefficients remains consistent across different values of θ_T and θ_B.

Flow behavior of bridge deck

The flow field was analyzed for two shapes of fairings viz.: i) Nose-up position (θ_T12–θ_B40; $h/D > 0.5$) and ii) nose-down position (θ_T40–θ_B12; $h/D < 0.5$). The mean surface pressures for these cases are shown in Fig. 7. The nose

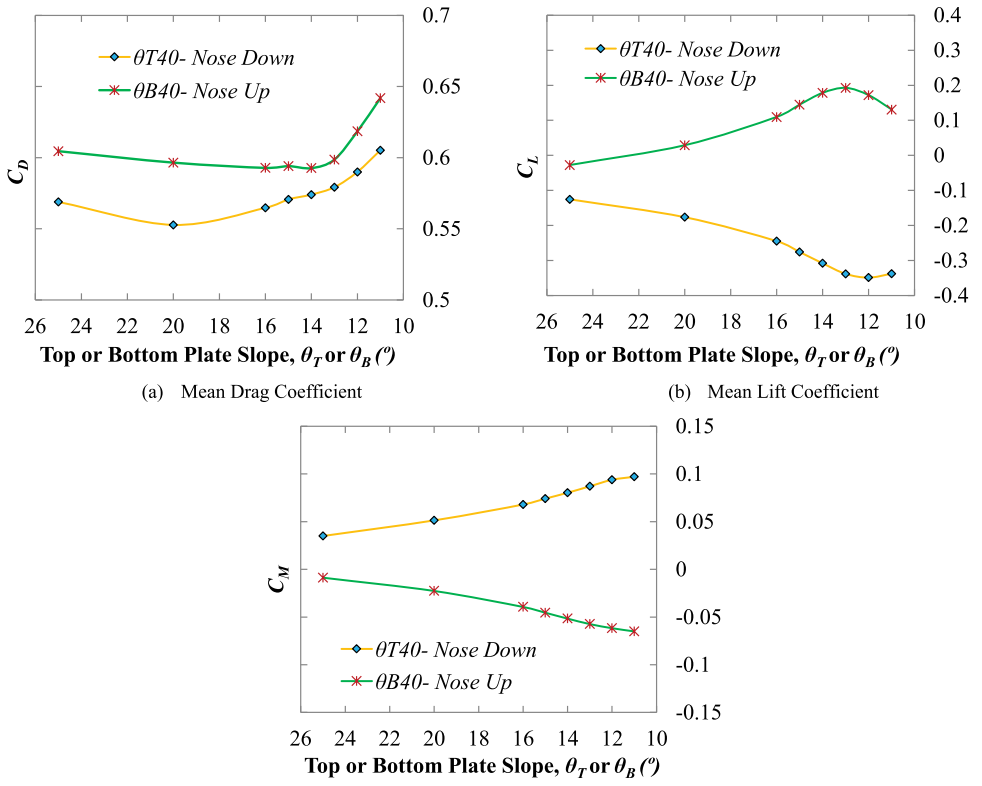

Figure 5. Mean force coefficients for variation fairing's angle with nose-down and nose-up positions

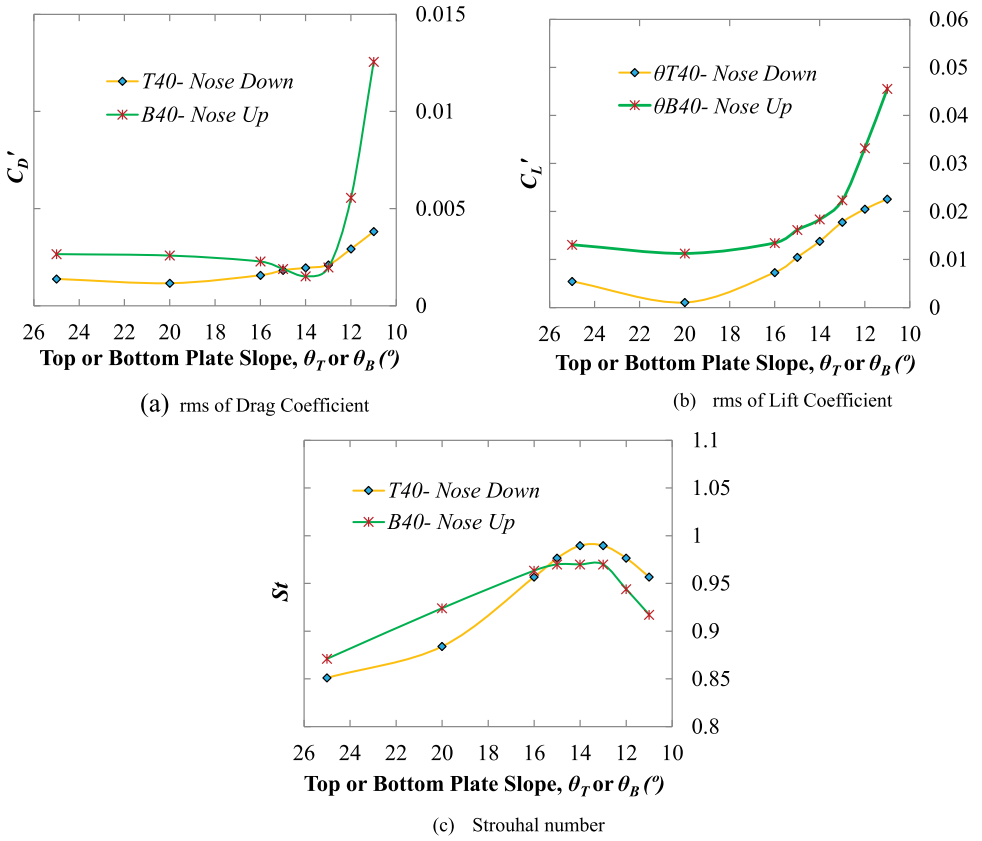

Figure 6. rms of force coefficients and Strouhal number for variation fairing's angle with nose-down and nose-up positions

location (h/D) primarily influences the pressure distribution near the leading edge of the deck, while the trailing edge is less affected. In the nose-down configuration ($h/D < 0.5$), a strong negative pressure appears on the leading-edge bottom surface, accompanied by positive pressure on the leading-edge top surface, resulting in a positive moment coefficient (counterclockwise moment). Conversely, in the nose-up configuration ($h/D > 0.5$), the moment coefficient is negative (clockwise moment) due to reversed pressure patterns.

When the fairing is in the nose-down position, the entire bottom surface of the deck experiences negative pressure (suction), which generates a negative lift force coefficient. Shifting the nose to the upper side reverses this effect, producing a positive lift due to suction on the top surface. The rms surface pressures, compared in Fig. 8, exhibit a contrasting behavior. The rms values are mainly influenced near the trailing edge, where the nose-up configuration ($h/D > 0.5$) shows slightly higher-pressure fluctuations than the nose-down case ($h/D < 0.5$). Instantaneous velocity fields over one lift cycle for the nose-down and nose-up configurations are illustrated in Figs. 9 and 10, respectively. These figures clearly show the leading-edge shear layer separation and reattachment, along with after-body vortex shedding. For the nose-down position ($h/D < 0.5$), significant suction occurs due to flow separation on the bottom surface near the leading edge. This bottom surface separation is more pronounced than the leading-edge top surface separation in the same configuration. Between the two positions, the

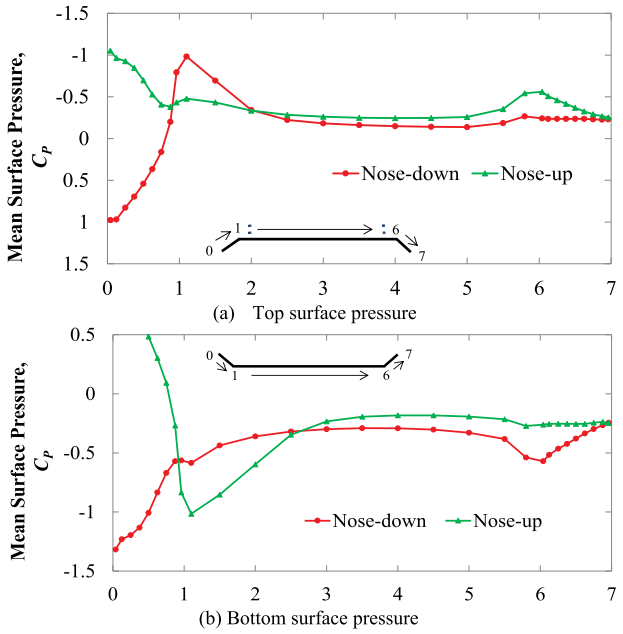

Figure 7. Mean surface pressure distribution around the bridge deck

nose-up configuration ($h/D > 0.5$) exhibits more prominent leading-edge flow separation compared to the nose-down case. Notably, the nose location also influences the size of the after-body vortex. It is observed that the vortex on the

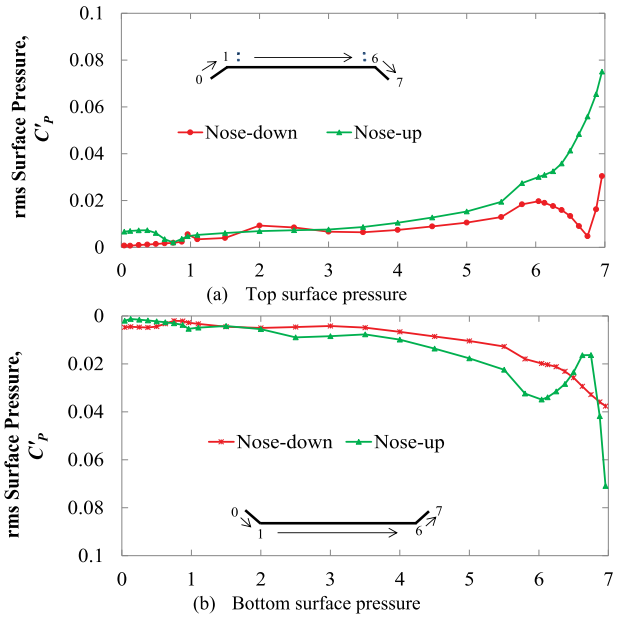

Figure 8. rms surface pressure distribution around the bridge deck

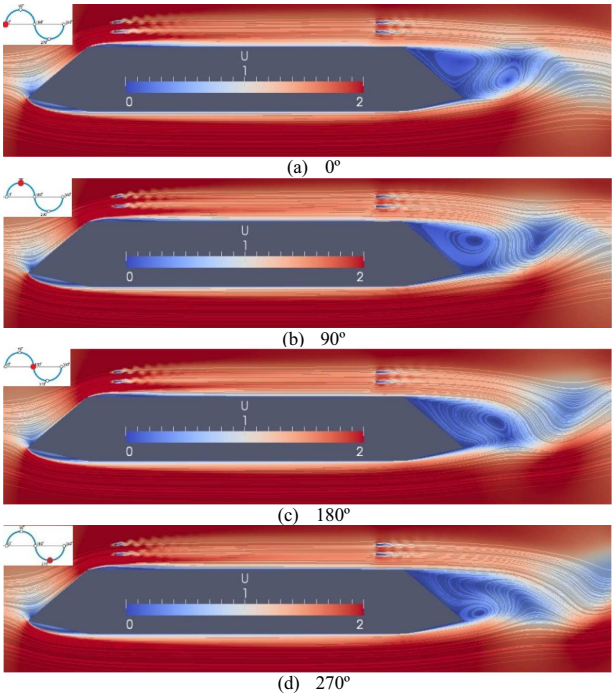

Figure 9. Velocity field around the bridge deck for nose-down condition along one lift cycle

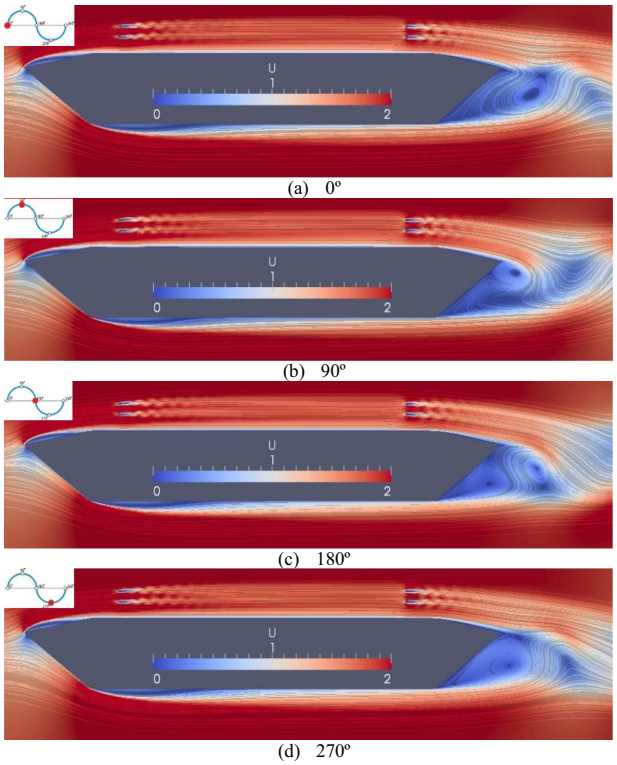

Figure 10. Velocity field around the bridge deck for nose-up condition along one lift cycle

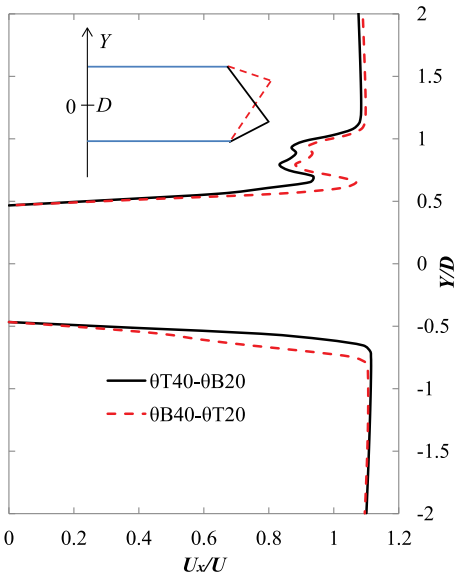

Figure 11. Velocity field around the bridge deck for nose-up condition along one lift cycle

side where the nose is located is smaller than the vortex on the opposite side.

Fig. 11 shows the velocity distributions along the vertical line at the mid-deck section. In both configurations, the velocity distribution along the bottom surface is relatively smooth, while the top surface distribution is more irregular due to the presence of the handrail. As the nose moves downward, the flow velocity along the bottom deck surface increases, enhancing suction and thereby increasing the deck's negative lift. For the nose-down position ($h/D < 0.5$), the shear layer on the bottom surface of the deck is thinner than that on the top surface. These shear layers separate at the trailing edge and roll up to form vortex shedding. The bridge deck with a nose-up position exhibits similar shear layer behavior but in the opposite sense.

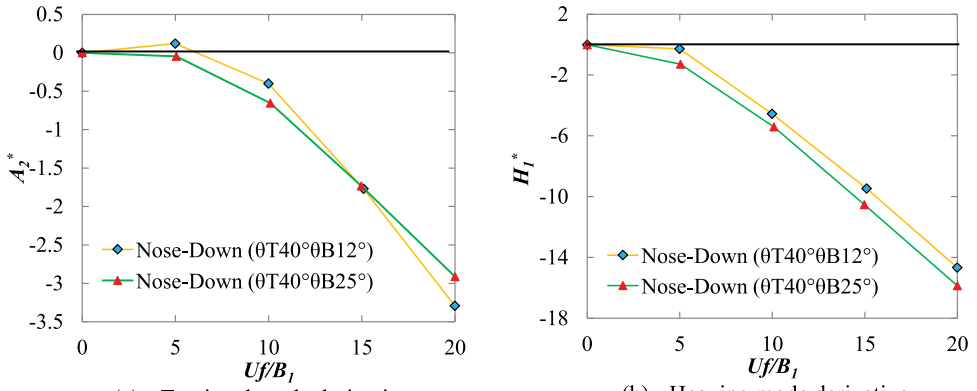

(a) Torsional mode derivative (b) Heaving mode derivative

Figure 12. Flutter derivatives for nose-down positions for two configurations (θ_T40–θ_B12 *and* θ_T40–θ_B25): a) torsional mode derivative (computed directly), and b) heaving mode derivative (computed based on interdependency relationship)

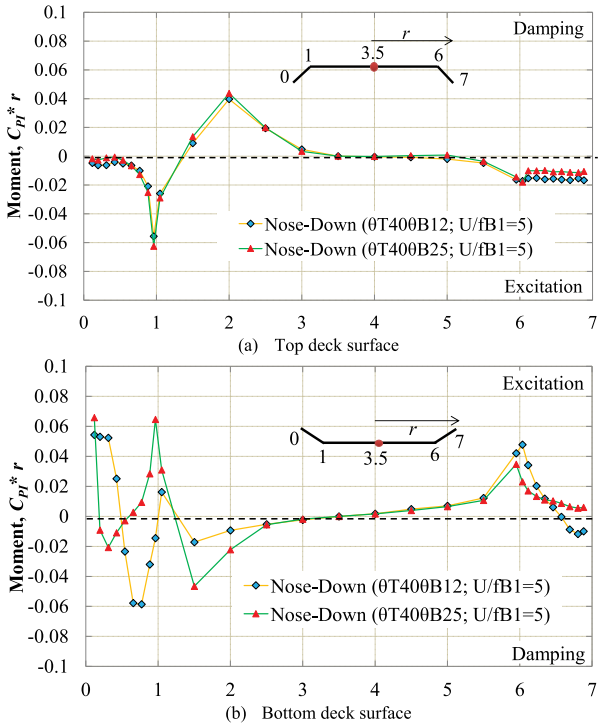

Figure 13. Influence of bottom plate slope (θ_B) for nose-down position on work done by unsteady pressure in torsional mode at low reduced velocity ($U/fB_1 = 5$)

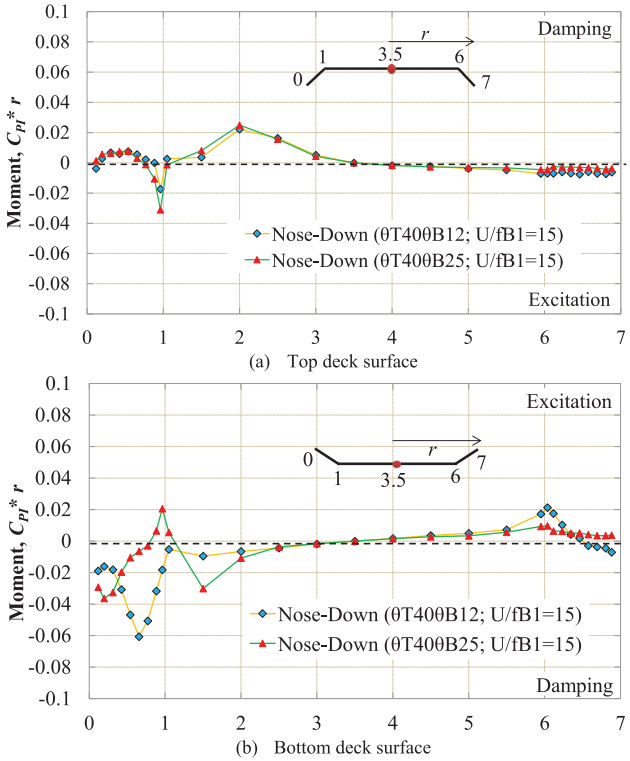

Figure 14. Influence of bottom plate slope for nose-down position on work done by unsteady pressure in torsional mode ($U/fB_1 = 15$)

Dynamic Responses

In the previous section, the static aerodynamic responses of the bridge deck with both nose-up and nose-down configurations were analyzed, revealing that the nose-down position offers improved static aerodynamic performance. Based on this finding, dynamic simulations were conducted for the nose-down configuration only, due to the high computational cost of such simulations. Two orientations of nose-down positions were selected with different bottom plate slopes (θ_B). Dynamic simulations were carried out for the nose-down configurations of $\theta_T40°$–$\theta_B12°$ and $\theta_T40°$–$\theta_B25°$ to evaluate flutter derivatives and the work done by unsteady pressure. The $\theta_T40°$–$\theta_B25°$ orientation has a relatively higher nose position as compared to the $\theta_T40°$–$\theta_B12°$ orientation. To simplify the analysis, handrails were excluded, and the forced vibration simulation was carried out on the basic deck section only.

Fig. 12 presents the key flutter derivatives A_2^* and H_1^* for the nose-down configurations ($\theta_T40°$–$\theta_B12°$ and $\theta_T40°$–$\theta_B25°$). The derivative A_2^* was calculated directly through numerical simulation, while H_1^* was obtained using

interdependency relationships. These two derivatives are particularly important, as they provide critical insights into the torsional and heaving mode vibrations of bridge decks. The results demonstrate that both of the nose-down configurations exhibit improved flutter performance. At a low reduced velocity ($U/fB_1 = 5$), the nose-down configuration with a smaller bottom plate slope ($\theta_T = 40°$, $\theta_B = 12°$) exhibited a positive value of A_2^*, indicating torsional instability. In contrast, the bridge deck with a steeper bottom plate slope ($\theta_T = 40°$, $\theta_B = 25°$) in the nose-down position remained aerodynamically stable across the entire range of considered reduced velocities. At higher reduced velocities, both torsional and heaving mode stabilities improve, confirming the favorable dynamic response of the bridge deck.

The work done by unsteady pressure in the torsional mode, as discussed in Section 3, is presented in Figs. 13 and 14 for both low ($U/fB_1 = 5$) and high ($U/fB_1 = 15$) reduced velocities. These figures show that leading-edge flow separation on both the top and bottom surfaces of the deck contributes to aerodynamic excitation, while flow reattachment acts as a source of aerodynamic damping. Additionally, trailing-edge flow separation near the fairing on both surfaces serves as another source of excitation.

At the lower reduced velocity ($U/fB_1 = 5$), variations in the bottom plate slope (θ_B) primarily affect the bottom surface near the leading edge. Increasing θ_B while maintaining the nose-down configuration enhances the damping magnitude at the bottom surface reattachment region. This results in improved torsional stability due to stronger aerodynamic damping. At higher reduced velocity ($U/fB_1 = 15$), the overall excitation and damping patterns remain similar, although the magnitudes are generally reduced. The most noticeable changes occur near the leading edge on the bottom surface, where almost all the area becomes aerodynamic damping and enhances the torsional stability further. In the nose-down position, θ_B has minimal impact on the top surface flow but significantly influences the bottom surface. As θ_B increases from 15° to 25°, the region of leading-edge damping shifts downstream (in the direction of flow) and grows in magnitude, while excitation near the trailing edge decreases. These effects collectively enhance the aerodynamic performance of the bridge deck.

Conclusions

The influence of the edge fairing's nose location (h/D) on the aerodynamic response of a box-girder bridge deck was investigated using two-dimensional unsteady RANS simulations. The fairing shapes were varied by altering the top (θ_T) and bottom (θ_B) plate slopes to assess the effect of nose location on both static and dynamic aerodynamic behaviors. The results demonstrated that the nose-down configuration provides superior aerodynamic performance. In this configuration, the bridge deck experiences reduced aerodynamic forces and smaller fluctuations, contributing to improved stability. When the fairing nose is positioned downward, flow separation at the leading-edge bottom surface is minimized. The flow reattaches downstream and then separates again at the trailing edge, forming a controlled after-body vortex shedding pattern. Additionally, the bottom surface of the deck experiences faster flow and a thinner shear layer, which generates a stronger downward lift force and further reduces aerodynamic fluctuations.

In terms of dynamic behavior, the nose-down configuration offers clear advantages, providing greater aerodynamic damping in both heaving and torsional vibration modes. This damping effect is sustained and even enhanced at higher reduced velocities, indicating improved aeroelastic stability. Analysis of the unsteady pressure distributions reveals that aerodynamic damping primarily originates in the leading-edge flow reattachment zone, while aerodynamic excitation is associated with flow separation at both the leading and trailing edges. Among the nose-down configurations, a higher bottom plate slope of 25° was found to be more advantageous compared to a slope of 12°. At this larger bottom plate slope (θ_B) of the edge fairing, the region of damping on the bottom deck surface shifts inward in the direction of the flow, with increased magnitude. Simultaneously, excitation at the trailing edge is reduced, resulting in improved aerodynamic performance.

Acknowledgements

Not applicable.

Authors' Contributions

The first author was responsible for the formulation of the problem, the analyses of numerical results, and the writing. The second author directed the whole work, and the third author helped in writing and formatting.

Funding

Not applicable.

Competing Interests

The authors declare that they have no competing interests.

References

[1] Nagao F, Utsunomiya H, Oryu T, Manabe S. Aerodynamic efficiency of triangular fairing on box girder bridge. *J Wind Eng Ind Aerodyn*. 1993;49(1-3):565–574. doi:10.1016/0167-6105(93)90050-x.

[2] De Miranda M, Bartoli G. Aerodynamic optimization of decks of cable-stayed bridges. Cable-supported bridges—challenging technical limits. In: *Proceeding of the IABSE Conference*; June 12–14, 2001; Seoul Korea, pp. 34–41.

[3] Sukamta, Nagao F, Noda M, Muneta K. Aerodynamic stabilizing mechanism of a cable stayed bridge with two edge box girder. In: *Proceedings of the 6th International Colloquium on Bluff Body Aerodynamics and Applications*; July 20–24, 2008; Milano, Italy.

[4] Haque MN, Katsuchi H, Yamada H, Nishio M. Investigation of edge fairing shaping effects on aerodynamic response of long-span bridge deck by unsteady RANS. *Arch Civil Mech Eng*. 2016;16(04):888–900. doi:10.1016/j.acme.2016.06.007.

[5] Haque MN, Katsuchi H, ZisanNagao MB. Geometric effects of edge fairing on aerodynamic characteristics of box girder bridge deck: influence of nose position. In: *Proceedings of International Conference on Structural Engineering Research (iCSER-2019)*; January 19–23, 2019; Dhaka, Bangladesh.

[6] Bruno L, Mancini G. Importance of deck details in bridge aerodynamics. *Struct Eng Int*. 2002;12(4):289–294. doi:10.2749/101686602777965234.

[7] Sarwar MW, Ishihara T, Shimada K, Yamasaki Y, Ikeda T. Prediction of aerodynamic characteristics of a box girder bridge section using the LES turbulence model. *J Wind Eng Ind Aerodyn*. 2008;96(10-11):1895–1911. doi:10.1016/j.jweia.2008.02.015.

[8] Sarwar MW, Ishihara T. Numerical study on suppression of vortex-induced vibrations of a box girder bridge section by aerodynamic countermeasures. *J Wind Eng Ind Aerodyn*. 2010;98(12):701–711. doi:10.1016/j.jweia.2010.06.001.

[9] Nieto F, Owen JS, Hargreaves DM, Hernandez S. Bridge deck flutter derivatives: efficient numerical evaluation exploiting their independencies. *J Wind Eng Ind Aerodyn*. 2015;136(4):138–150. doi:10.1016/j.jweia.2014.11.006.

[10] Mannini C, Šoda A, Ralph V, Schewe G. Unsteady RANS simulation of flow around a bridge section. *J Wind Eng Ind Aerodyn*. 2010;98(12):742–753. doi:10.1016/j.jweia.2010.06.010.

[11] Mannini C, Šoda A, Schewe G. Unsteady RANS modeling of flow past a rectangular cylinder: investigation of Reynolds number effects. *Comput Fluids*. 2010;39(09):1609–1624. doi:10.1016/j.compfluid.2010.05.014.

[12] Brusiani F, De Miranda S, Patruno L, Ubertini F, Vaona P. On the evaluation of bridge deck flutter derivatives using RANS turbulence model. *J Wind Eng Ind Aerodyn*. 2013;119:39–47. doi:10.1016/j.jweia.2013.05.002.

[13] Miranda SD, Patruno L, Ubertini F, Vairo G. On the identifications of the flutter derivatives of bridge deck via RANS turbulence models: benchmarking on rectangular prisms. *Eng Struct*. 2014;76:359–370. doi:10.1016/j.engstruct.2014.07.027.

[14] Patruno L. Accuracy of numerically evaluated flutter derivatives of bridge deck sections using RANS: effects on the flutter onset velocity. *Eng Struct*. 2015;89:49–65. doi:10.1016/j.engstruct.2015.01.034.

[15] Šarkić A, Fisch R, Höffer R, Bletzinger K. Bridge flutter derivatives based on computed, validated pressure fields. *J Wind Eng Ind Aerodyn*. 2012;104–106(2–3):141–151. doi:10.1016/j.jweia.2012.02.033.

[16] Haque MN, Katsuchi H, Yamada H, Nishio M. Strategy to develop efficient grid system for flow analysis around two-dimensional bluff bodies. *KSCE J Civil Eng*. 2015;20(05):1–12. doi:10.1007/s12205-015-0696-2.

[17] Shirai S, Ueda T. Aerodynamic simulation by CFD of flat box girder of super-long span suspension bridge. In: *Proceedings of Fifth Asia-Pacific Conference on Wind Engineering*; 2001; Kyoto, Japan, pp. 21–24.

[18] Haque MN, Katsuchi H, Yamada Y. Bottom plate slope effects on aerodynamic behaviour of hexagonal cross-section bridge deck. Wind engineering for natural hazards: modeling, simulation and mitigation of windstorm impact on critical infrastructure. *Trends Eng Mech Spec Publ No 3*. 2018:205–223. doi:10.1061/9780784415153.ch11.

[19] Menter FR. Two-equation eddy-viscosity turbulence models for engineering application. *AIAA J*. 1994;32(8):1589–1605. doi:10.2514/3.12149.

[20] Donea J, Huerta A, Ponthot Ph J, Rodríguez-Ferran A. Encyclopedia of computational mechanics, Volume 2 solids and structures. In: *Chapter Arbitrary Lagrangian–Eulerian Methods*. Chichester: Wiley; 2004:413–438.

[21] Ferziger JH, Perić M. *Computational Methods for Fluid Dynamics*. 2nd ed. Berlin, Heidelberg: Springer; 2002.

[22] Haque MN, Katsuchi H, Yamada Y, Nishio M. Flow field analysis of a pentagonal-shaped bridge deck by unsteady RANS. *Eng Appl Comput Fluid Mech*. 2015;10(1):1–16. doi:10.1080/19942060.2015.1099569.

[23] Simiu E, Scalan RH. *Wind Effects on Structures: Fundamentals and Applications to Design*. 3rd ed. New York: John Wiley & Sons Publisher; 1996.

[24] Larsen A, Walther JH. Discrete vortex simulation of flow around five generic bridge deck sections. *J Wind Eng Ind Aerodyn*. 1998;77–78:591–602. doi:10.1016/s0167-6105(98)00175-5.

[25] Haque MN, Katsuchi H. Influence of separation interference method on aerodynamic responses of a pentagonal shaped bridge deck. *Structures*. 2018;16(3):27–35. doi:10.1016/j.istruc.2018.08.010.

[26] Matsumoto M. Aerodynamic damping of prisms. *J Wind Eng Ind Aerodyn*. 1996;59(2-3):159–175. doi:10.1016/0167-6105(96)00005-0.

[27] Tubin F. Relationships among aerodynamic admittance functions, flutter derivatives and static coefficients for long-span bridges. *J Wind Eng Ind Aerodyn*. 2005;93(12):929–950. doi:10.1016/j.jweia.2005.09.002.

[28] Haque MN, Katsuchi H, Yamada H, Kim H. Influence of geometric configuration on aerodynamics of streamlined bridge deck by unsteady RANS. *Wind Struct*. 2019;28:331–345.

[29] Huang L, Liao H, Wang B, Li Y. Numerical simulation for aerodynamic derivatives of bridge deck. *Simul, Model, Pract Theor*. 2009;17(4):719–729. doi:10.1016/j.simpat.2008.12.004.

[30] Sarkar PP, Caracogila L, Haan FL, Sato H, Murakoshi J. Comparative and sensitivity study of flutter derivatives of selected bridge deck sections, Part 1: analysis of inter-laboratory experimental data. *Eng Struct*. 2009;31(1):158–169. doi:10.1016/j.engstruct.2008.07.020.

BER the international journal of bridge engineering management and research

Seismic Isolation in Newly Built Bridges in Italy: Historical Development, Regulations, and Recent Applications

Federico Scafati[1,*]; Chiara Ormando[2]; Paolo Clemente[3]; and Giacomo Buffarini[4]

Submitted: 09 August 2025 **Accepted:** 15 September 2025 **Publication date:** 10 October 2025

DOI: 10.70465/ber.v2i4.51

Abstract: Seismic isolation is a well-mature technique to protect structures against earthquakes, allowing to achieve a level of safety not possible with conventional systems. The Somplago Viaduct on the Udine–Tarvisio highway, built in 1976, was the first seismically isolated bridge in Italy. Its good performance during the strong shocks, which hit the viaduct when it was still under construction, encouraged the use of seismic isolation in bridges. The development of applications in Italy was initially quite slow, due to the delay in considering this new technology in technical standards. Significant developments occurred following the major seismic events that affected the country. Today, seismic isolation is almost always used for new construction projects and, especially, in major cases such as those illustrated in this paper, whose aim is to document the Italian experience and illustrate applications.

Author keywords: Newly built bridges; Seismic isolation; State-of-the-art in Italy

Introduction

An appropriate anti-seismic protection system is fundamental to obtaining good performance of a structure during earthquakes. The choice depends on the structural characteristics of the bridge and the seismic hazard of the site. With these premises, seismic isolation is a well-mature technique to protect structures against earthquakes and can be used in most cases, allowing for a level of safety not achievable with traditional technologies.

It is well known that a seismic isolation system consists of a set of isolation devices placed between the substructure, which remains anchored to the ground, and the superstructure, which will be seismically isolated. The isolation strategies to achieve the reduction of the horizontal seismic response, regardless of the typology and structural materials of the structure, are:

- Increasing the fundamental period of vibration to bring it into a range with lower response accelerations.
- Limiting the maximum horizontal force transmitted.

In both strategies, the isolation performance can be improved by dissipating a significant portion of the mechanical energy transmitted from the ground to the structure.

After some non-engineered proposals and realizations in ancient eras and some pioneering devices patented at the end of the nineteenth century and the first decades of the twentieth century, seismic isolation started in Europe in the 1970s.[1] Interesting applications were realized in Italy in bridges. The very first one referred to the Somplago Viaduct, along the Udine–Tarvisio highway, in Friuli, Northeastern Italy. It was hit by two severe seismic events on September 15, 1976 (M = 5.9 and M = 6.0, respectively), with the epicenter just a few kilometers from the bridge. The viaduct was under construction, and its excellent behavior favored a rapid increase in the application of anti-seismic systems in newly built bridges and viaducts. Italy became a leading country in the field, with more than 150 applications by the beginning of the 1990s.[2]

Seismically isolated buildings appeared later in Italy. The first was the fire command building in Naples, completed in 1981. In order to leave as much space as possible on the ground floor for vehicle movement, the steel structure is suspended from reticular beams, which rest on reinforced concrete towers by means of neoprene supports. Floor dampers and shock transmitter units were also used. The second building was the Telecom Italia Centre at Ancona, completed in 1991. A release test was performed on one of the five buildings, with an initial displacement equal to 110 mm, to test the performance of the 297 high-damping rubber bearings isolation system.[3]

The good performance of seismic isolation systems has been demonstrated during strong earthquakes all over the world. In Italy, however, the behavior under low-energy

*Corresponding Author: Federico Scafati.
Email: federico.scafati@guest.univaq.it
[1]Visiting Engineer, University of L'Aquila, 67100 L'Aquila, Italy
[2]Researcher, ENEA Casaccia Research Centre, 00123 Rome, Italy
[3]Research Director, Formerly ENEA Casaccia Research Centre, 00123 Rome, Italy
[4]Research Director, ENEA Casaccia Research Centre, 00123 Rome, Italy

Discussion period open till six months from the publication date. Please submit separate discussion for each individual paper. This paper is a part of the Vol. 2 of the International Journal of Bridge Engineering, Management and Research (BER), ISSN 3065-0569.

earthquakes has pointed out the necessity of considering this condition in the design phase and checking the correct working of the different types of devices.[4–9] Design criteria and optimization have also been developed for both elastomeric and sliding devices (SDs).[10–12]

The use of seismic isolation in Italy was slowed by the absence of a technical code. In the absence of a technical code that defines the rules to follow, it was not possible to implement seismic isolation. As usual, the seismic events have provided significant impulse to the development and issuance of new seismic standards. The first standard issued in Italy followed the 1997 Umbria–Marche seismic sequence and was not a proper code, which in Italy is legally binding, but simple guidelines for seismically isolated structures.[13] These were issued in 1998 and required a very long and complicated approval process by a special committee of the Ministry of Infrastructures.

After the earthquake that struck the Molise region in 2002 (M = 5.4), with an ordinance of the presidency of the council of ministers (OPCM 3274),[14] a new seismic code was issued, which accounted for the most recent European standards. It included design rules for seismic isolation and energy dissipation systems, whose use was from then on permitted without specific approvals. The new code encouraged the use of new anti-seismic technologies, especially in high seismicity areas and for structures for which a very high level of safety was required.

Finally, in 2008 the new Italian Technical Code for Constructions (NTC-2008)[15] was issued, which included all the technical codes that had been issued separately in the past. Seismic isolation had become a common anti-seismic technique, the use of which was well regulated within the standards both in terms of design aspects and those regarding the devices to be used and the related materials. The Italian code was updated in 2018 (NTC-2018)[16] and will probably be updated in the next years.

This paper traces the development of seismic isolation in bridges in Italy and reports the main regulatory aspects, highlighting the differences with buildings. The aim is to document the Italian experience and illustrate applications, rather than to provide new analytical and experimental insights. Finally, some of the major projects completed in recent years are illustrated as examples of the most commonly used types and devices.

Seismically Isolated Bridges in Italy

In Fig. 1, the development of the number of seismically isolated structures in Italy is plotted, classified as bridges, buildings, and other structures. It should be first noted that applications in bridges began earlier, and their number grew much more rapidly than in buildings and other structures.

Focusing on bridges, after a timid start between the second half of the 1970s and the first half of the 1980s, a significant increase in the number of seismic-isolated bridges was recorded starting in the mid-1980s. This was followed by a period of gradual but slow increase, primarily due to the mentioned reasons related to the lack of a standard. Then,

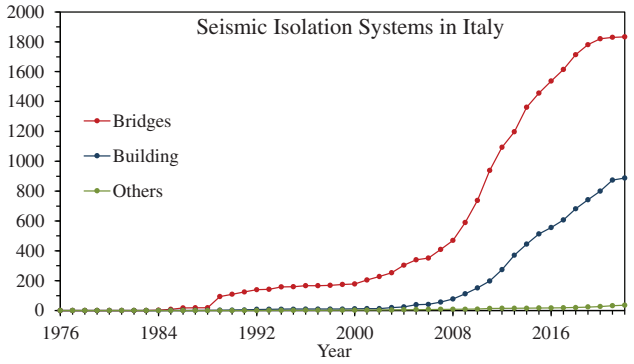

Figure 1. Development of the number of seismically isolated structures in Italy

after 2002, the year of the Molise earthquake and, above all, the issuance of OPCM 3274, a certain increase occurred. However, it was after 2009, the year of the L'Aquila earthquake and the definitive entry into force of the NTC-2008, that the number of applications increased significantly.

Nowadays, the application of new anti-seismic technologies in bridges is more than 2000 in Italy. The number of applications in existing bridges is quite low compared with the applications in new structures, but a significant number of applications has occurred in the recent years.[17]

SDs associated with dampers of different types were first used on a large scale in Italy, especially since 1988. Lead rubber bearings (LRBs) appeared in the same period, but their use has been limited. After 2004, high damping rubber bearings (HDRBs) were used extensively and then, after 2009, also curved surface sliders (CSSs). These are still the most common isolator types used.

Among the experimental tests conducted in Italy, noteworthy are those performed on a 1:5 scale model of a seismically isolated bridge span at the shake table laboratory of ENEA.[18] Different isolation devices were used in the tests, such as rubber isolators and CCSs with varying friction coefficients, in addition to bearings made of simple neoprene simulating the original ones.

Notes on the Italian Standards for Seismic Isolation in Bridges

In bridges, isolation devices are usually inserted in place of the common support devices, between the vertical structures, that is, the piers and abutments, and the deck. Thus, the seismic actions that affect the deck are significantly reduced. Obviously, the substructure also benefits, because the seismic actions that the deck transmits to the vertical structures, and therefore to the foundations, will also be reduced. The set of devices defines the isolation interface. The choice and distribution of devices must optimize the distribution of horizontal seismic forces from the deck to the various support structures. The isolation system includes the connection elements and any additional constraints arranged to limit horizontal displacements due to non-seismic actions,

such as wind. The substructure, in general, cannot be considered infinitely rigid, contrary to what normally occurs in buildings.

As for buildings, also for bridges the superstructure and the substructure must remain in a substantially elastic range even for the actions to be considered for the check at the ultimate limit state (ULS). A higher reliability is required for the isolation devices due to their critical role.

Unlike buildings, the effects of accidental eccentricity of the masses in isolated bridges can usually be neglected. To allow the free movement of the different parts, and thus the correct working of the isolation system, the separation joints between the different portions of the deck and between the deck and the substructure must be correctly sized. Furthermore, the spatial variability of the ground motion must be taken into account as specified for non-isolated bridges.

As regards the mechanical properties of the isolation system and the modelling of the substructure and superstructure, the same requirements apply as for buildings. Linear dynamic analysis can be used if the device behavior can be modelled with its equivalent characteristics; otherwise, the nonlinear dynamic analysis is to be preferred and sometimes mandatory. Linear static analysis is allowed only if specific conditions are satisfied, while nonlinear static analysis cannot be used. In the case of linear analysis, a behavior factor $q = 1$ must be assumed.

The check at the ULS of the isolation devices subject to the combinations inherent in the horizontal variable actions (such as wind) must be carried out and could sometimes be decisive. Particular attention must be paid to avoid hammering between different adjacent parts of the structure.

Referring to construction, maintenance, and replaceability issues, and the testing phase, there are no additional requirements with respect to buildings.

It should be noted that seismic isolation is also particularly suitable for the retrofitting of existing bridges, where often the only replacement of the existing bearings with seismic isolators could be sufficient for the seismic retrofit. In both cases, seismic isolation allows obtaining very high performance, in accordance with the new severe design standards, and is becoming a must in the construction and retrofit of bridges.

Recent Notable Newly Built Bridges

Bearing manufacturers and construction companies, as well as engineering firms, were invited to provide information on the main applications of seismic isolation systems in newly built bridges in Italy in recent years. Thanks to their contribution, some of these are described in the following paragraphs.

San Giorgio bridge

The San Giorgio Bridge in Genoa (Fig. 2) replaced the Polcevera Viaduct, designed by Riccardo Morandi, which partially collapsed on August 14, 2018, and was then demolished in June 2019. It was designed, built, and tested in only sixteen months. This result was achieved thanks to its structural simplicity but also by optimizing all the phases, ensuring rapid and high-quality work. It was opened to traffic on August 3, 2020.

The bridge is a continuous beam, with a total length of 1067.17 m, consisting of 19 spans. The three main spans are 100 m each; all the others are 50 m, except the last two, which are 40.9 and 26.27 m, respectively. The deck is composed of a steel multi-box beam, which has the shape of a ship hull, and a reinforced concrete slab (Fig. 3).[19]

The 18 hollow reinforced concrete piers have an elliptical cross-section with maximum dimensions in plan of 9.50 × 4.0 m to improve aerodynamic properties against wind action (Fig. 3). Their height varies from 32.0 to 39.0 m, except for the first pier P1 and the last pier P18, whose heights are 19.50 and 11.0 m, respectively. The bridge foundations are deep, resting on 1.50 m diameter piles.

At the east end of the viaduct, a three-span ramp accessing the bridge is connected to the main structure. It is composed of three spans of 35.1, 44.79, and 37.82 m,

Figure 2. View of the San Giorgio Bridge

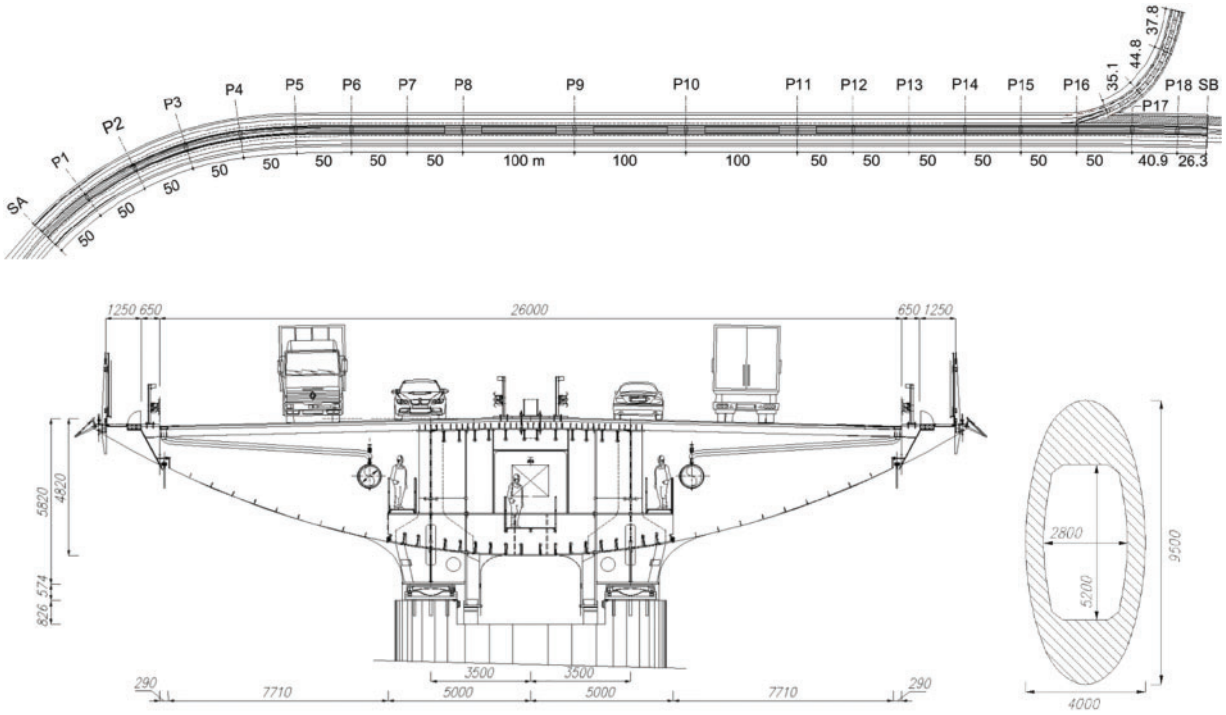

Figure 3. San Giorgio Bridge: Plan, cross-section of the deck and the piers

respectively, having a total length of 117.71 m. The ramp is supported by an abutment and three piers, 11.55, 26.3, and 35.8 m high, respectively, and has dimensions in plan of 4.75 × 2.10 m. The last pier is very close to the main deck.

The designer conceived a slender bridge with narrow piers to emphasize the lightness of the new structure. For this reason, the distance between the upper surface of the piers and the deck intrados is 1.4 m, greater than the conventional one.

The San Giorgio Bridge is also an example of advanced technology. It was designed to be an efficient and smart structure, with its integrated monitoring system, which allows:

- The monitoring of the service facilities, the environmental conditions, the structural behavior, and the degradation phenomena.
- The automatic inspection of the deck condition and the washing of the windbreaks and the solar panels.
- The creation of a database to better schedule the maintenance.

The isolation system is made up of 51 devices, two for each pier and three for each of the three abutments. The main bridge is seismically isolated by means of 42 devices, whose characteristics are shown in Table 1:

- At each of the two abutments: Two multidirectional bearings and one longitudinal prismatic guide.
- At both end piers P1 and P18: Two multidirectional bearings.
- On each of the piers from P2 to P7 and from P12 to P17, which support the 50 m spans: Two single CSSs (i.e., with a single surface, in total 12 of B type and 12 of B + S type).
- On each of the central piers from P8 to P11, which support the 100 m spans: Two single CSSs with a higher vertical load capacity (in total 4 of A type and 4 of A + S type).

The deck of the accessing ramp has nine devices:

- On the abutment: Two multidirectional bearings and one elastomeric bearing.
- On each of the three piers: Two single CSSs.

The cross-section of the deck (Fig. 3) has a total width of 29.8 m, while the spacing between the devices is 7.0 m. The structural analysis proved the good performance of the isolation system both in static and dynamic conditions. The use of single CSS allowed optimizing the project. All checks, including the overturning one, were satisfied.

One of the two CSSs at each pier is equipped with a transverse fuse or S-plug (A + S and B + S CSS types), as shown in Fig. 4, to avoid transverse movements of the deck in service conditions under non-seismic loads, such as wind action (i.e., ULS and service limit state). At the same time, longitudinal guides located in the same position allow expansion and contraction of the deck, also because the fuses are placed inclined with respect to the piers, to minimize the effects due to the thermal action.

The S-plugs will still be working in low-intensity seismic conditions (i.e., operation limit state SLO and damage limit state SLD, according to the Italian code), not allowing transverse movements nor modifying the dynamic response of the isolation system. The fundamental oscillation period is 2.0 s.

In extreme seismic conditions (i.e., life safeguard limit state SLV and collapse limit state SLC, according to the Italian code), all the S-plugs break, and the anti-seismic

Table 1. Main bridge: Characteristics of the devices

	Device type	Max vertical force (kN)	Max longitudinal horizontal force (kN)	Max trasversal horizontal force (kN)	Max longitudinal displacement (mm)	Max transverse displacement (mm)
SA abutment	Longitudinal prismatic guide	—	—	4000	±400	—
	Multidirectional bearings	15000	—	—	±400	±50
P1	Multidirectional bearings	35000	—	—	±375	±100
From P2 to P7	Curved surface sliders "B + S"	35000		3300		±350
	Curved surface sliders "B"	35000		1720		±350
From P8 to P11	Curved surface sliders "A + S"	60000		4400		±200
	Curved surface sliders "A"	60000		2450		±200
From P12 to P17	Curved surface sliders "B + S"	35000		3300		±350
	Curved surface sliders "B"	35000		1720		±350
P18	Multidirectional bearings	35000	—	—	±375	±100
SB abutment	Multidirectional bearings	15000	—	—	±400	±50
	Longitudinal prismatic guide	—	—	4000	±400	—

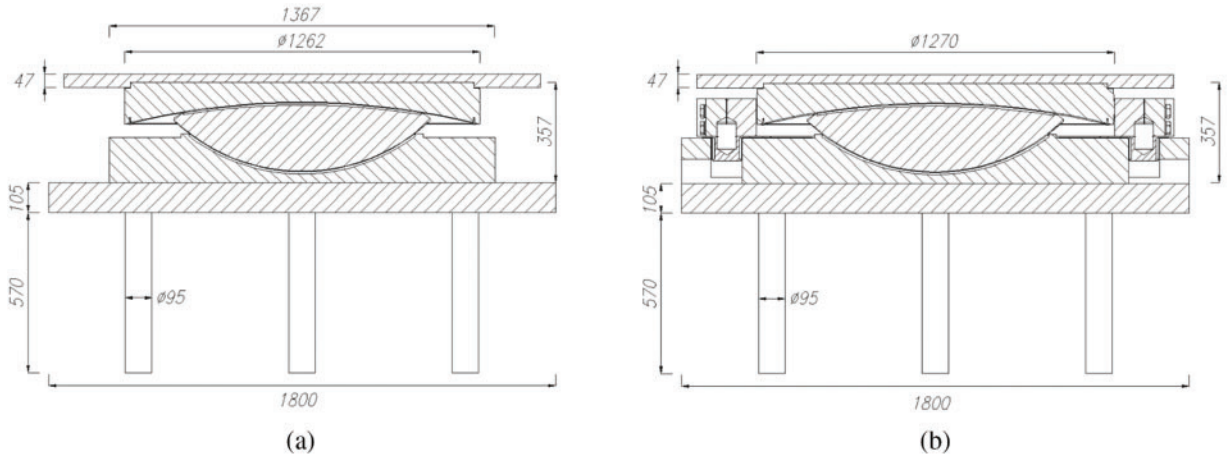

Figure 4. San Giorgio Bridge: CSS devices, (a) type A and (b) type A + S

protection is ensured by the devices, which have the following characteristics: Radius of curvature R = 3.0 m, fundamental vibration period T_{is} = 3.0 s, dynamic friction coefficient μ = 1%, and maximum displacement d = ±350 mm.

A + S- and B + S-type devices were designed to absorb the maximum shear force at ULS. This value is higher than the capacity of the S-plugs, which was determined by SLV analysis in upper bound conditions. For A- and B-type devices, without S-plugs, the maximum shear force is obtained from the constitutive law of the devices and using the friction coefficient in upper bound condition.

The dynamic response of the structure was analyzed both with and without the contribution of S-plugs. For this reason, these elements were also subjected to fatigue checks

for a 300 kN force. The most severe condition is that at ULS, both in terms of stress and deformation. In fact, thanks to the use of the isolation system, the stresses on piers due to the seismic actions in the transversal direction are lower than those due to wind actions. In the same condition, longitudinal thermal displacements are also higher than the seismic ones. It is worth reminding that friction shall not be used to relieve this effect.

The re-centering capacity of the isolation system was verified. Inspection, maintenance, and replacement of the devices have also been guaranteed. For these reasons, vertical steel elements were placed (Fig. 5). These legs were designed to:

- Lift the deck with hydraulic jacks for isolator maintenance and replacement.
- Reposition the deck in case of imperfect re-centering of the isolation system after an extraordinary event.
- Guarantee a higher level of safety by acting as a constraint in case of displacements exceeding the design values, even if the CSS were dimensioned for the worst conditions.

Finally, at the shortest piers P1 (19.50 m) and P18 (11.0 m), only multidirectional bearings were located to make the stiffness characteristics of the entire structure as uniform as possible and to guarantee the optimal behavior of the isolation system both in static and dynamic conditions.

The use of multidirectional bearings and longitudinal guides on the main bridge abutments limits the transversal displacements, optimizing the joints' behavior (±400 mm in the longitudinal direction). The maximum vertical load for this kind of device is 35000 kN at P1 and P18, while the longitudinal guides are designed for a transversal load of 4000 kN. With reference to the single CSSs, the devices of the 50 m spans are characterized by a vertical capacity of 35000 kN, a maximum horizontal force of 3300 kN, and a design displacement of ±350 mm. For the isolators of the 100 m spans, the previous values become 60000 kN, 4400 kN, and ±200 mm, respectively. On the ramp, due to the presence of elastomeric bearings on the abutments, the joint is bidirectional (±400 mm in the transversal direction, ±350 mm in the longitudinal direction).

The Albiano Magra bridge

The Albiano Bridge over the Magra River (Fig. 6) between the villages of Caprigliola and Albiano Magra in the town of Aulla, Tuscany, replaced the previous five-span arch bridge along the SS330 road, built in 1948 and suddenly collapsed on April 8, 2020. Due to the coronavirus quarantine then in

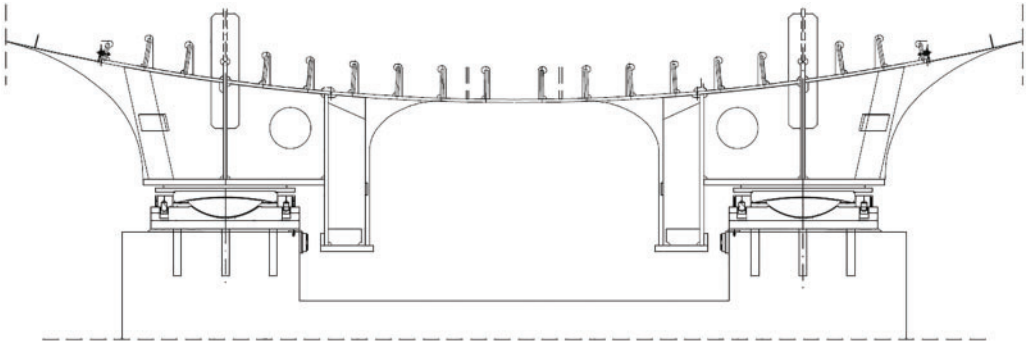

Figure 5. San Giorgio Bridge: Vertical steel "legs," which are a safe system in case of displacements exceeding the design values but also allow lifting the deck with hydraulic jacks for maintenance and replacement of isolators, and the repositioning of the deck in case of imperfect re-centering after an extraordinary event

Figure 6. The Albiano Bridge over the Magra River

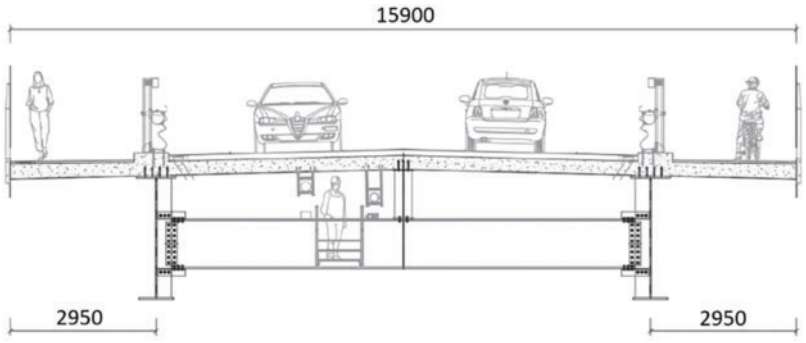

Figure 7. The Albiano Bridge: Cross-section

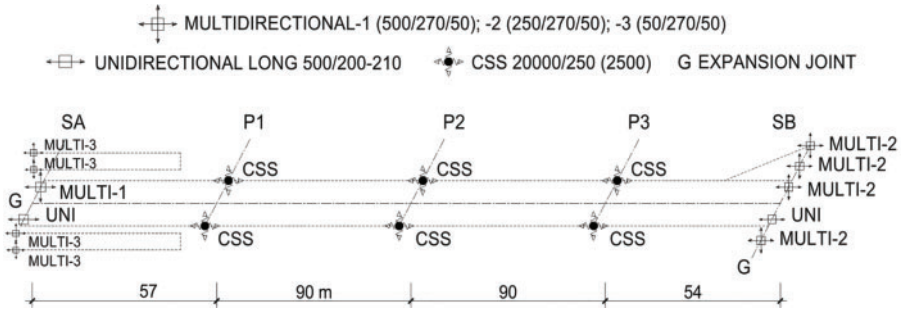

Figure 8. The Albiano Bridge: Anti-seismic devices

force, the traffic on the bridge was absent, so the collapse caused no injuries.

The new bridge, which was opened to traffic on April 30, 2022, has a continuous deck with a total length of 291.0 m and four spans. The two central spans have a length of 90 m, and the side ones are 57 and 54 m, respectively. The cross-section is composed of two main steel beams, having a variable height and spaced 10 m apart, a secondary beam between them, and a concrete slab. The deck, including the external pedestrian and cycle lanes, is 15.9 m wide at the piers (Fig. 7) and 27.0 m wide at Abutment B (Caprigliola side). Immediately after pier P1 and up to Abutment A (Albiano side), there are external lanes, independent from the main deck and running at different heights.[20]

The isolation system is made of 13 devices for the bridge plus four for the external pedestrian and cycle lanes, deployed as follows (Fig. 8):

- Abutment A (SA): One confined elastomeric disc multidirectional bearing (MULTI-1) and one unidirectional longitudinal bearing (UNI).
- On both sides of Abutment A: Two multidirectional bearings for the external paths (MULTI-3).
- On each of piers P1, P2, and P3: Two double CSSs, with $R = 2.5$ m and $\mu = 0.055$.
- Abutment B (SB): Four confined elastomeric disc multidirectional bearings (MULTI-2) and one unidirectional longitudinal bearing (UNI).

The design of the new bridge had to consider the presence of multiple risks, such as hydraulic, structural, and seismic risks. For this reason, the anti-seismic devices were located at a height such as to be protected against 200-year design floods and projected to guarantee their best behavior against wind and braking actions.

The main characteristics of the devices are shown in Table 2. In the longitudinal direction, the abutments are not loaded because of the presence of longitudinal and multidirectional bearings. Abutment B (Caprigliola side) is located on an unstable slope, subject to a monitored landslide. For this reason, the maximum displacement values obtained from the structural analysis were increased by ±70.0 mm to prevent the risk of low movements of the slope. At the same time, low piers are only 2.0 m high with rounded edges in the transversal direction, to offer the minimal resistance to the river flow.

In the transversal direction, the choice was not to allow movements at the abutments to optimize the behavior of the joints and to guarantee a driving comfort. Even construction details benefit from this limitation. In fact, bridge parapets, gas and water pipes, telephone lines, and so forth, were designed to absorb only longitudinal displacements at lower costs. On the other hand, higher solicitations in the transversal direction do not cause problems in these elements. Transversal displacements at the piers are allowed by the deformability of the deck. According to the designers, the effectiveness of the isolation system in these conditions is guaranteed for bridges with more than three spans, as in the present case.[20]

The CSS radius of curvature equal to 2.5 m allows recentering in seismic conditions and absorption of braking and wind actions while neglecting friction.

A nonlinear dynamic analysis was performed, considering the local seismic response. In the lower bound design properties analysis (μ reduced by 20%), the fundamental

Table 2. Albiano Magra Bridge: Characteristics of devices

	Device type	Max vertical force (kN)	Max longitudinal horizontal force (kN)	Max trasversal horizontal force (kN)	Max longitudinal displacement (mm)	Max transverse displacement (mm)
SA abutment	Multidirectional bearing	5000	—	—	±200	±50
	Unidirectional bearing	5000	—	2100	±200	—
P1-P3	Curved surface sliders	20000	2000			±250
SB abutment	Unidirectional bearing	5000	—	2100	±270	—
	Multidirectional bearing	2500	—	—	±270	±50

Figure 9. The Filomena Delli Castelli bridge

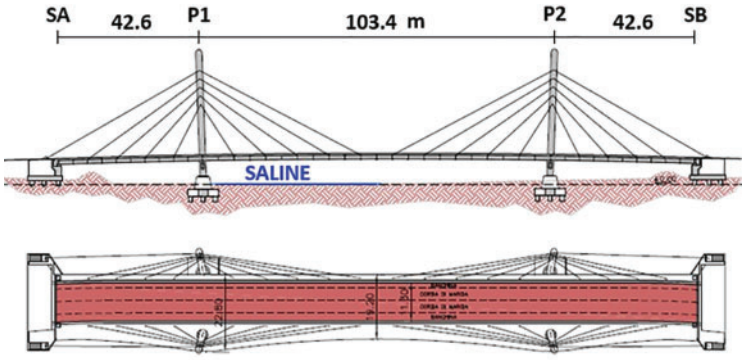

Figure 10. Filomena Delli Castelli Bridge: Longitudinal view and plan

period is 2.3 s in the longitudinal direction and 1.8 s in the transversal direction. In the upper bound design properties analysis (μ increased by 50%), the maximum forces acting on the piers are 1600 and 1150 kN, respectively.

The abutment multidirectional and unidirectional bearings are designed for a vertical load of 5000 kN with a displacement capacity of ±200 mm, considering the SLC seismic condition with a thermal effect increased by 50%. In the same condition, the maximum transversal force acting on unidirectional bearings is 2100 kN. About double CSSs, the maximum vertical load is 20000 kN with a horizontal displacement equal to ±250 mm.

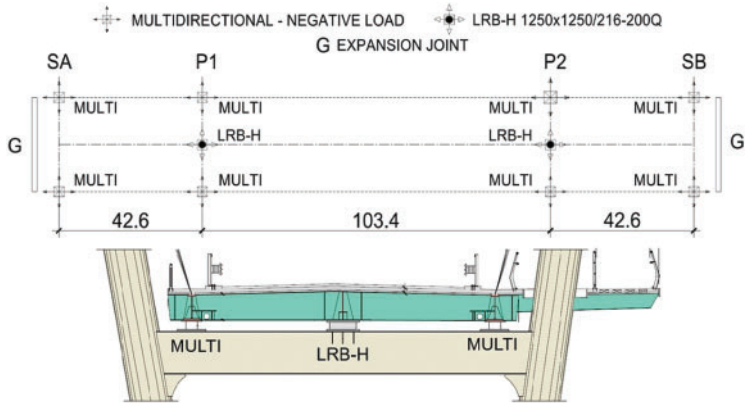

Figure 11. Filomena Delli Castelli Bridge: Layout of the constraints and detail at the pylons

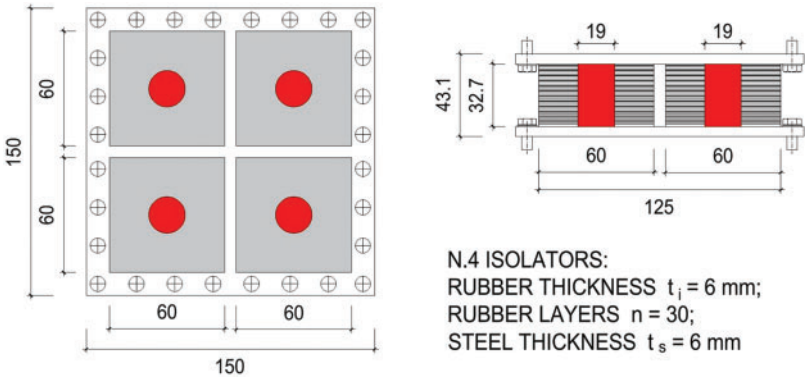

Figure 12. Filomena Delli Castelli Bridge: Elastomeric isolators

The Filomena Delli Castelli bridge

The Filomena Delli Castelli Bridge (Fig. 9), spanning the Saline River near its mouth at Montesilvano, Abruzzo, is a cable-stayed bridge with a central span of 103.4 m and two lateral spans of 42.6 m. Both the deck and the pylons are made of a mixed steel-concrete system (Fig. 10).

The deck has an overall width varying from 19.20 to 22.70 m. It consists of two longitudinal double-T steel beams, 1.20 m high and spaced 14.10 m apart, and a reinforced concrete slab with Predalles slabs arranged longitudinally on the transverse beams. These, with a height varying from 0.80 to 1.20 m, are placed at a longitudinal distance of 4.70 m in the central span and 4.26 m in the lateral ones and extend beyond the beams, cantilevering for a length varying between 4.00 m and 7.50 m at the upstream side and for 1.10 m at the downstream side.[21]

Each of the two pylons consists of two circular steel antennas with a diameter of 1.90 m and a height of 33.45 m at the upstream side and 36.40 m at the downstream side. The antennas are filled with concrete, reinforced with studs for the first 16 m of height. They are connected transversally by a steel transverse beam placed underneath the deck. Each antenna is inclined outward transversally by 10° for the upstream two antennas and 8° for the downstream two antennas, and longitudinally by 2°. At the base, each antenna is fixed to a truncated cone-shaped concrete element, which in turn is constrained to a foundation plinth supported by nine piles (diameter = 1.20 m, length = 35 m). The plinths of the two antennas are connected by a concrete beam.

The stays are arranged in a semi-fan shape, anchored to the pylons on five levels, and to the deck spaced 9.40 m apart in the central span and 8.52 m in the lateral ones. The two pairs of outer stays are anchored to the abutment walls. The transverse distance of the anchor points increases from 14.10 to 26.10 m, thus ensuring a reduction in transverse bending.

The bearings of the main beams on the transverse beams connecting the two antennas and on the abutments are multidirectional PTFE bearings able to support negative loads.

One LRB is positioned between each transverse beam connecting the two antennas of each pylon and the corresponding transverse beams of the deck (Fig. 11). These bearings control the horizontal displacements of the deck and guarantee an increase in the vibration period and energy dissipation. For construction reasons, each bearing is composed of four isolators, each with a lead core and an equivalent horizontal stiffness of 4.25 kN/mm, thus ensuring a total equivalent horizontal stiffness of 17 kN/mm, equivalent viscous damping greater than 25%, and a maximum horizontal displacement of ±200 mm (Fig. 12).

The Genzano Viaduct

The Genzano Viaduct (Fig. 13) is located near L'Aquila, at 722 m a.s.l., on a limestone rock geological site. It is part of the seismic retrofitting project that involves more than 20

Figure 13. View of the new Genzano Viaduct

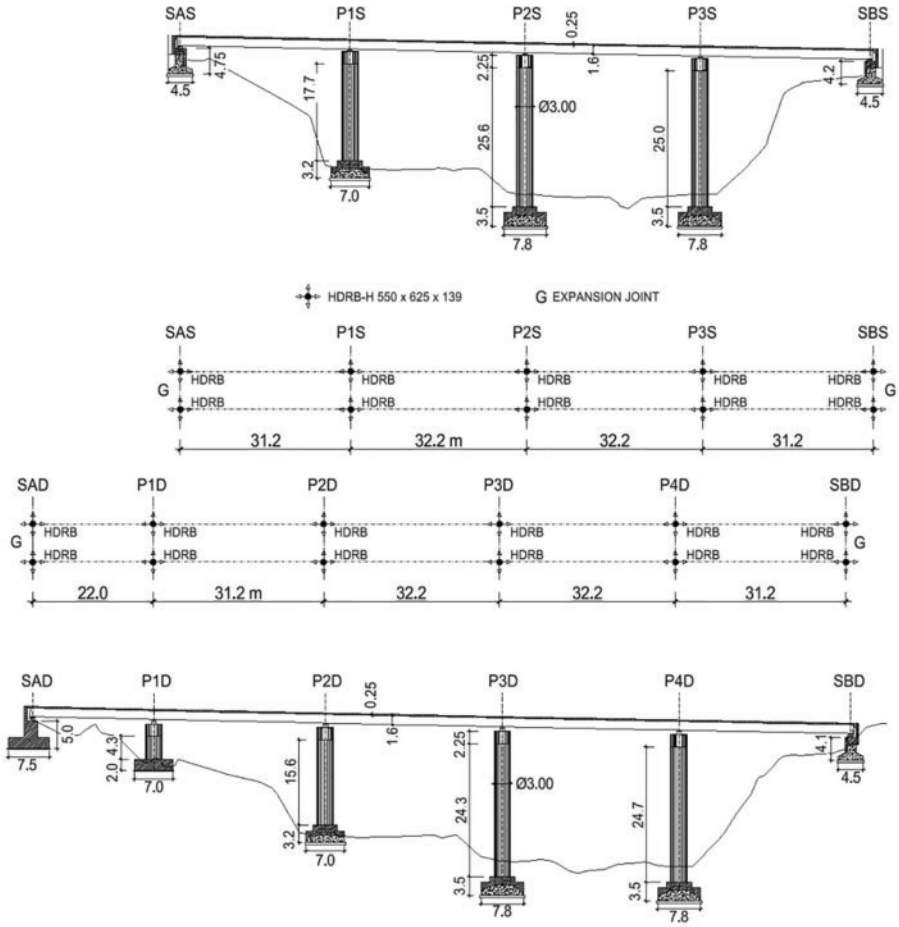

Figure 14. Genzano Viaduct: Longitudinal view and plan

viaducts along the A24 Rome–L'Aquila–Teramo highway. The design phase started at the end of 2017, so it was one of the first projects in accordance with the Italian Technical Code NTC2018. Furthermore, according to the indication of the Italian Ministry of Infrastructure and Transport, new viaducts had to guarantee a nominal life of 100 years due to their strategic importance for Civil Protection purposes, as demonstrated during the 2009 L'Aquila earthquake. This translates into considering a design seismic event having a return period of at least 950 years for the structure, and a design seismic event with a return period of at least 1950 years for the design of the isolation devices.

The new Genzano Viaduct consists of two separate structures that replace the previous ones (Fig. 14).

They maintain the position of abutments and piers and, therefore, the number of spans and their lengths, except for

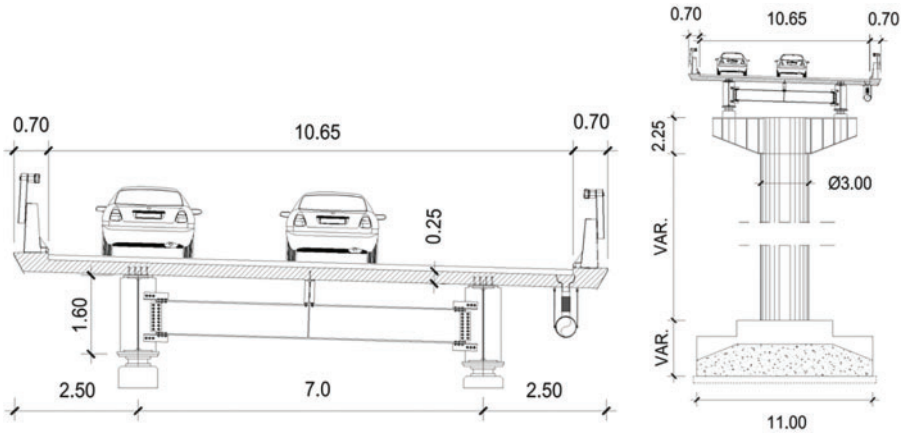

Figure 15. Genzano Viaduct: Transversal section and pier

Figure 16. Isolation devices of Genzano Viaduct: Panoramic view, scheme, and during deck launching

the first on the road toward Teramo, where a new abutment was realized to obtain a longer span of 22 m compared to the existing one of 18 m. The viaduct toward Rome has four spans, two of 31.2 m and two of 32.2 m, for a total length of 126.8 m. The viaduct toward Teramo has five spans, one of 22 m, two of 31.2 m, and two of 32.2 m, for a total length of 148.8 m.

Each deck is a continuous mixed steel-concrete girder made of two main beams spaced 7.0 m apart, with a secondary one in the central position and transverse beams. The new piers are full-section reinforced concrete and Cor-Ten steel. All the abutments are in reinforced concrete; the existing ones were retrofitted with tie rods to absorb the higher longitudinal forces transmitted by the new deck (Fig. 15). The direct foundations were retrofitted in all cases, except for the pier P1D, which was rebuilt.

The new structure was realized using crane trucks located at the base and the highway operation was always guaranteed thanks to the adjacent carriageway and to the night launching of the decks.

The seismic isolation system is composed of two HDRBs for each pier and abutment. The maximum vertical load in static condition is 6355 kN, while the maximum horizontal force in seismic conditions is 750 kN. Each device has an effective horizontal stiffness of 2.84 kN/mm and an equivalent viscous damping of 15%. A linear analysis, according to the Italian technical code, was performed obtaining a maximum displacement of 225 mm (Fig. 16).

The left carriageway was opened to traffic on June 29, 2021, and the right carriageway on June 10, 2022.

Conclusions

One of the world's first applications of seismic isolation in bridges was realized in Italy in 1976 with the Somplago Viaduct. Starting from this application, which is part of the history of seismic isolation, the development and application of this technology in Italy in the field of bridges and viaducts has been retraced. This process was linked to the development of appropriate technical standards that allowed its use, establishing the main rules to be observed in design, construction, and testing, and the use of new devices. Finally, four notable recent examples were selected and shown, each with unique characteristics, which demonstrate the potential of seismic isolation in protecting bridges against earthquakes.

The cases illustrated highlight how seismic isolation represents an optimal solution in various situations and for various structural, architectural, and functional needs that are difficult to achieve with traditional techniques. Among these, seismic safety must be foremost. Indeed, strategically important bridges must be operational even during and immediately after a strong seismic event.

Safety and rapid construction times are a perfect match for the San Giorgio Bridge, thanks also to its structural simplicity, characteristics that meet the need for an effective and safe infrastructure.

The same characteristics are found in the Albiano Magra Bridge and the Genzano Viaduct, structures located along major roads, subject to heavy traffic and connecting important and densely populated parts of the country.

But seismic isolation also allows for the right balance between functionality and elegance in naturalistic settings, always respecting the safety and resilience of the structure, as in the case of the Filomena Delli Castelli Bridge.

However, these are just a few examples of the multitude of seismically isolated bridges and viaducts present in Italy today from the perspective of documenting the Italian applications. Other challenges, not covered by this analysis, should be considered, such as maintenance, durability, and limitations, which will be the subject of a future paper.

Acknowledegments

The authors are grateful to all those who provided data, articles, photos, and project drawings used in this paper. They thank particularly: Eng. M. Orlandini and Eng. G.M. Aluffi of Webuild S.p.A. for the San Giorgio Bridge; Eng. S. Isani of Matildi + Partners for the Albiano Magra Bridge; Prof. L. Dezi and Dezi Steel Design Srl for the Filomena Delli Castelli Bridge; Carlo Toto, President of Toto Holding, for the Genzano Viaduct.

References

[1] Clemente P. Seismic isolation: past, present and the importance of SHM for the future. *J Civ Struct Health Monit*. 2017;7(2):217–231. doi:10.1007/s13349-017-0219-6.

[2] Clemente P, Martelli A. Seismically isolated buildings in Italy: state-of-the-art review and applications. *Soil Dynam Earthquake Eng*. 2019;119:471–487. doi:10.1016/j.soildyn.2017.12.029.

[3] Clemente P. New challenges in the development and application of seismic isolation. In: Kasimzade A, et al. ed. *Earthquake Resistant Design, Protection, and Performance Assessment in Earthquake Engineering, AERS 2023. Geotechnical, Geological and Earthquake Engineering*. Cham: Springer; 2024;54:44–60. doi:10.1007/978-3-031-65407-7_2.

[4] Clemente P, Bongiovanni G, Buffarini G, Saitta F, Castellano MG, Scafati F. Effectiveness of HDRB isolation systems under low energy earthquakes. *Soil Dynam Earthquake Eng*. 2019;118:207–220. doi:10.1016/j.soildyn.2018.12.018.

[5] Clemente P, Di Cicco A, Saitta F, Salvatori A. Seismic behaviour of base isolated civil protection operative centre in Foligno, Italy. *J Perform Construc Facilit*. 2021;35(4):04021027. doi:10.1061/(ASCE)CF.1943-5509.0001589.

[6] Salvatori A, Bongiovanni G, Clemente P, Ormando C, Saitta F, Scafati F. Observed seismic behaviour of a HDRB and SD isolation system under far fault earthquakes. *Infrastructures*. 2022;7(2):13. doi:10.3390/infrastructures7020013.

[7] Ormando C, Clemente P, Iannirubertо U, Scafati F. Onset of motion of curved surface sliders used in seismic isolation systems. *Pract Period Struct Des Construct*. 2021;26(3):04021015. doi:10.1061/(ASCE)SC.1943-5576.0000580.

[8] Saitta F, Clemente P, Bongiovanni G, Buffarini G, Salvatori A, Grossi C. Base isolation of buildings with curved surface sliders: basic design criteria and critical issues. *Adv Civil Eng*. 2018;2018:1569683. doi:10.1155/2018/1569683.

[9] Scafati F, Ormando C, Clemente P, Bongiovanni G. Observed behavior of buildings seismically isolated with CSSs under a low energy earthquake. *J Civil Struct Health Monit*. 2022;12(2):225–243. doi:10.1007/s13349-021-00539-z.

[10] Clemente P, Buffarini G. Base isolation: design and optimization criteria. *Seismic Isolat Protect Syst*. 2010;1(1):17–40. doi:10.2140/siaps.2010.1.17.

[11] Tripepi C, Clemente P. Graphic procedure for the optimum design of elastomeric isolators. *Pract Period Struct Des Construct*. 2021;26(1):04020058, ASCE. doi:10.1061/(ASCE)SC.1943-5576.0000547.

[12] Tripepi C, Ormando C, Clemente P. On the preliminary design of CSS isolation systems. In: *Proceeding of the 19th World Conference on Seismic Isolation 19WCSI*; Sep 15–19, 2025; Berkeley, California USA: PEER.

[13] Consiglio Superiore dei Lavori Pubblici. Linee guida per progettazione, esecuzione e collaudo di strutture isolate dal sisma. LG-1998. *Ingegneria Sismica*. 1997;1.

[14] Presidenza del Consiglio dei Ministri (PCM). Primi elementi in materia di criteri generali per la classificazione sismica del territorio nazionale e di normative tecniche per le costruzioni in zona sismica. OPCM 3274 of 20.03.2003. Supplemento Ordinario No. 72 of Gazzetta Ufficiale No. 105 of 08.05.2003.

[15] MIT (Ministero Infrastrutture e Trasporti). Norme Tecniche per le Costruzioni. NTC-2008, Decreto Ministeriale MIT of 14.01.2008, Supplemento Ordinario No. 30 of Gazzetta Ufficiale No. 29 of 04.02.2008 Serie Generale.

[16] MIT (Ministero Infrastrutture e Trasporti). Aggiornamento delle Norme Tecniche per le Costruzioni. Decreto Ministeriale MIT of 17.01.2018. Supplemento Ordinario No. 8 alla Gazzetta Ufficiale No. 42 of 20.02.2018 Serie Generale.

[17] Clemente P. Applications and recent studies on seismic isolation in Italy. In: Cimellaro GP, ed. *Seismic*

Isolation, Energy Dissipation and Active Vibration Control of Structures. WCSI 2022. Lecture Notes in Civil Engineering. Cham: Springer; 2023;309:3–16. doi:10.1007/978-3-031-21187-4_1.

[18] Ormando C, Clemente P, Roselli I, et al. Shake table tests of a bridge model with different seismic isolation devices. In: Sadan B, Tuzun C, Erdik M. eds. *Seismic Isolation, Energy Dissipation and Active Vibration Control of Structures. WCSI 2023. Lecture Notes in Civil Engineering*. Cham: Springer; 2024;533:101–117. doi:10.1007/978-3-031-66888-3_9.

[19] Vittozzi A, Bonifacio F, Isani S, Cammarota G, Barrasso P. The Genova's San Giorgio bridge. The history of the deck project from concept to testing. *Costruzioni Metalliche*. 2020;4:9–23.

[20] Matildi G, Antoniani V, Bertoncelli A, Isani S. The new Albiano bridge: from fast design to rapid reconstruction. *Costruzioni Metalliche*. 2023;1:22–31.

[21] Dezi L, Dezi G, Innocenzi RD, Traversini M. The Filomena Delli Castelli Bridge over the Saline River (PE). *Costruzioni Metalliche*. 2023;1:46–58.

BER the international journal of bridge engineering management and research

Smart Acoustic Sounding for Automated Delamination Detection in Concrete Bridge Decks

Deepak Kumar[1,*]; Anil K. Agrawal[2]; and Ran Cao[3]

Submitted: 14 August 2025 **Accepted:** 15 September 2025 **Publication date:** 10 October 2025

DOI: 10.70465/ber.v2i4.54

Abstract: Concrete bridge decks are susceptible to subsurface defects such as delamination, caused by aging, corrosion, and environmental stressors, underscoring the need for timely, reliable nondestructive evaluation. While traditional acoustic methods, such as hammer or chain drag, remain widely used, they suffer from subjectivity, inconsistent impact forces, and limited applicability on overhead or vertical surfaces.

This study introduces a novel Smart Acoustic Sounding System that modernizes impact sounding through an integrated framework consisting of a broadband electronic chirp excitation source, high-sensitivity Micro-Electro-Mechanical Systems microphones with acoustic shielding, and a tracking camera for automated and location-aware inspections. Advanced signal processing techniques, such as empirical mode decomposition, power spectral density, and the Hilbert–Huang transform, are employed to filter noise, extract frequency-based features, and support machine learning–based defect classifications. Laboratory testing on a full-scale concrete slab embedded with known artificial defects (e.g., shallow and deep delamination, voids, and honeycombing), as well as a deteriorated concrete beam, confirmed the system's ability to accurately identify defect zones, particularly shallow delamination with characteristic frequency signatures in the range of 1–3 kHz. The system produced real-time defect maps with minimal human input, demonstrating its potential to improve the accuracy, repeatability, and efficiency of bridge deck inspections and support data-driven maintenance decisions.

Author keywords: Structural health monitoring; delamination detection; concrete bridge decks; acoustic impact sounding; machine learning; nondestructive evaluation; signal processing

Background and Motivation

Concrete structures, especially bridges, are critical components of transportation infrastructure. Their timely inspection and maintenance are essential to ensure public safety and uninterrupted service. In the United States, the American Society of Civil Engineers (ASCE) estimates that over 42,000 bridges (approximately 6.8%) are in poor condition, and nearly 45% have exceeded their original 50-year design life.[1] These statistics underscore the urgent need for scalable, accurate, and objective inspection methods to assess structural health, particularly for aging concrete bridge decks prone to subsurface deterioration. Among various deterioration mechanisms, delamination, a separation of concrete layers typically caused by corrosion of steel rebars, is one of the most prevalent and structurally significant. These hidden defects compromise the durability of bridge decks and can progress to spalling and eventual degradation in the structural performance. Since delamination is not visually observable, inspectors have traditionally relied on impact acoustic methods, where variations in sound (such as ringing versus hollow) indicate the presence of defects. Manual sounding techniques, such as hammer tapping and chain dragging, remain widely used by state Departments of Transportation (DOTs) due to their simplicity and low cost.

However, conventional acoustic sounding methods suffer from critical limitations. The process is inherently subjective and depends heavily on an inspector's auditory interpretation and experience. It is also labor-intensive, requiring surface gridding and individual point-wise testing, making it time-consuming, inconsistent, and prone to human error. Environmental noise, variable impact forces, and limited accessibility to vertical or overhead surfaces further reduce the reliability and efficiency of these methods. Uncontrolled broadband impact sounding may fail to capture frequency-specific signatures from defects such as shallow delamination, which often resonate within the 1–3 kHz range.

Despite these challenges, impact-based sounding remains one of the most trusted nondestructive evaluation (NDE) methods for concrete decks in practice. According to a

*Corresponding Authors: Deepak Kumar.
Email: dkumar@ataneconsulting.com
[1]Engineer, ATANE Consulting, New York, NY 10005
[2]Professor of Civil Engineering, The City College of New York, NY 10031
[3]Associate Professor, Hunan University, Hunan, China

Discussion period open till six months from the publication date. Please submit separate discussion for each individual paper. This paper is a part of the Vol. 2 of the International Journal of Bridge Engineering, Management and Research (BER), ISSN 3065-0569.

2024 Federal Highway Administration (FHWA) survey of state highway agencies, methods such as hammer sounding, chain dragging, and impact echo are among the most commonly used and are perceived as reliable for concrete deck evaluation.[2] Fig. 1 shows a comparison of the performance of various methods based on the FHWA study. These findings highlight the continued relevance of traditional acoustic methods while pointing to the need for modernization of the sounding approach to improve its consistency, objectivity, and data capture.

Advances in acoustic sounding and automation

Over the past two decades, researchers have sought to automate and improve acoustic sounding through better hardware and signal processing. Tong et al.[3] and Luk et al.[4,5] applied wavelet transforms and hidden Markov models to impact-acoustic signals for defect detection in bonded structures. Popovics[6] introduced a rolling cart with multiple hammers and microphones that used power spectral density (PSD) analysis to map delamination, though it required the cart to remain stationary during each strike. Sun et al.[7] introduced a continuous scanning device using smooth steel "ball-chain" drags and short-time Fourier transform analysis. This design reduced low-frequency noise (<5 kHz) and increased coverage speed, but it still required contact and was limited to horizontal surfaces. Larsen et al.[8] implemented a multichannel impact mechanism for continuous deck inspection from a moving vehicle, while Hendricks et al.[9] demonstrated high-speed, impact-echo testing for rapid data collection. These systems significantly reduced human involvement, but their mechanical complexity introduced challenges related to weight, power demands, and operational stability. In a more unconventional approach, Blaney and Gupta[10] explored using drones to drop small hammers and record acoustic responses. However, payload limitations and flight stability hindered practical implementation. Despite their promise, fully autonomous mechanical impact systems remain constrained by size, payload, and the need for physical contact at each test point. These limitations restrict deployment on small or airborne robotic platforms and confine inspections to accessible, contact-friendly surfaces.

Noncontact excitation and chirp-based methods

To overcome the contact-related limitations, researchers have explored noncontact acoustic sources. Noncontact NDE techniques aim to excite vibrations in the structure without direct impact, thereby avoiding some constraints of mechanical systems. High-power speakers and even focused electric spark discharges have been studied as impact alternatives that can launch stress waves into concrete from a standoff distance.[11,12] Such approaches can potentially enable fast, continuous scanning since no physical reset is needed between test points. Dabous and Feroz[13] further reviewed the state-of-the-art noncontact testing technologies for condition monitoring of bridges, highlighting the potential for automated data acquisition and processing, an area that Smart Acoustic Sounding System (SASS) directly builds upon. Among these, broadband chirp signals offer significant advantages: they excite a wide range of structural resonant modes in a single sweep, and post-processing

Figure 1. Reported confidence levels of various NDE methods used for concrete bridge deck evaluations, based on FHWA's 2024 survey

allows for targeted frequency-band analysis. Michaels et al.[14] demonstrated the effectiveness of chirp excitation in guided wave testing, showing improved defect imaging through multifrequency excitation. Michaels et al.[15,16] expanded on this by demonstrating how chirp-generated acoustic wavefield images can be used for high-resolution defect visualization, validating the use of chirp excitations in complex structural materials. Similarly, Feng et al.[17] and Mizutani and Inokawa[18] used chirp-excited Lamb waves for delamination detection in composite plates, an approach that translates well to concrete bridge decks. Chirp-based excitation provides standardized, repeatable inputs that are independent of operator variability. It also supports rapid repetition and is well-suited for integration with robotic systems. By covering a wide frequency range, chirp signals can excite multiple resonant modes simultaneously. Preliminary studies suggest that shallow delamination in concrete responds strongly in the 1–3 kHz range, while pristine areas exhibit energy at higher frequencies, an insight that informed the detection algorithms developed in this study.

ML and AI integration

In parallel, machine learning (ML) has emerged as a powerful tool for pattern recognition in acoustic NDE. Muramatsu et al.[19] proposed a noncontact approach for flaw detection using neural network classification of signals from laser Doppler vibrometers, showing the growing influence of artificial intelligence (AI)–driven feature classification in vibration and acoustic analysis. Ye et al.[20] implemented an online learning system where human inspectors' classifications were used to train an algorithm in real time. More recent efforts include the application of deep learning. For example, Alhebrawi et al.[21] used AI to identify concrete cracks from acoustic hammer data with high accuracy. Convolutional neural networks (CNNs), combined with acoustic emission sensors, have shown effectiveness in recognizing time–frequency patterns of crack signals.[22,23] Jafari and Dorafshan[24] applied Naïve Bayes classifiers to features extracted from impact-echo signals, while Barbosh et al.[25] used wavelet-enhanced deep learning for damage localization. Another emerging trend is the integration of multiple NDE modalities with autonomous data collection. Hoxha et al.[26] combined impact-echo and ground-penetrating radar with visual SLAM (Simultaneous Localization and Mapping) for navigation, creating a robotic platform capable of generating three-dimensional defect maps through sensor fusion. Lavadiya and Dorafshan[27] reviewed deep learning applications across NDE domains and emphasized the importance of data consistency and sensor integration. They noted that variability across acquisition systems hampers reproducibility, highlighting the value of standardized excitation and processing. Similarly, Scherr and Grosse[28,29] argued that inconsistent signal quality undermines the comparability of NDE results and advocated for improved data quality control.

This technological convergence of advanced sensing and AI was summarized in our recent review,[30] which outlined the role of hybrid approaches where decomposed acoustic signals (e.g., via empirical mode decomposition [EMD], PSD) are fed into ML models such as CNNs, support vector machines (SVMs), or ensemble classifiers to enhance the detection of delamination, cracking, and other anomalies. However, a significant challenge remains in developing generalizable AI models that can adapt to variable field environments and data sources. Lehman[31] similarly stressed the importance of data-driven inspection tools in national infrastructure assessments.

Gap and study objective

Despite advances in mechanized and AI–driven methods, current approaches to bridge deck inspection continue to face key challenges: heavy reliance on operator skills, the mechanical complexity of contact-based systems, and inconsistent data interpretation across different platforms. To address these limitations, this study introduces a SASS, which is a portable and fully integrated framework that reimagines conventional sounding. SASS incorporates:

- a programmable broadband chirp excitation source for consistent, repeatable impacts,
- Micro-Electro-Mechanical Systems (MEMS) microphones with acoustic shielding for robust noise suppression,
- visual SLAM cameras for location-aware defect mapping, and
- real-time signal processing and ML algorithms (EMD, Hilbert–Huang transform [HHT], PSD) for automated classification.

This system is designed for pole-mountable or portable deployment, enabling reliable inspection of both horizontal and overhead surfaces with minimal human input. Laboratory and field experiments on slabs with artificial defects and deteriorated beams validate its performance.

The key contributions of this work are:

- Development of a standardized, broadband chirp-based sounding method for operator-independent delamination detection.
- Integration of acoustic, visual, and computational modules into a single automated inspection device.
- Demonstration of real-time defect mapping and classification accuracy through laboratory and field experiments.

Methodology

Overview of research approach

This study follows a two-phase experimental approach to develop and validate the SASS. The methodology integrates system development, laboratory testing, and comparative evaluation against conventional manual sounding methods. In the first phase, a large-scale concrete slab embedded with engineered defects, including shallow and deep delamination, honeycomb regions, and voids, was tested

using traditional hammer-based acoustic methods. A handheld hammer was used to apply impacts across the slab surface, and the resulting acoustic signals were recorded and analyzed. This baseline evaluation served to characterize the frequency responses of each defect type while also documenting the challenges of manual inspection, such as subjectivity, inconsistent impact force, and the absence of automated localization. In the second phase, the same specimen was tested using the SASS developed in this study. The system integrates an electronic chirp excitation device, which generates a broadband acoustic pulse in a controlled and repeatable manner. A high-sensitivity MEMS microphone captures the resulting structural response, and a visual SLAM–based tracking camera logs the spatial coordinates of each impact location. This hardware combination enables real-time, location-aware defect mapping without requiring manual surface gridding or positioning.

Signal data collected from both traditional and smart methods were processed using advanced signal processing algorithms. These techniques filter noise, isolate dominant frequency content, and extract relevant features for automated classification. A supervised ML model was then trained to classify each acoustic response based on these features. This two-phase design enabled direct, side-by-side comparison of manual and smart methods under identical conditions, and allowed for assessment of how automation improves repeatability, objectivity, and efficiency in field inspections.

Test specimen and defect configuration

A full-scale concrete slab in the NDE laboratory of the FHWA Turner Fairbank Highway Research Center has been used as a controlled test bed for acoustic sounding experiments. The slab measures 40 inches by 120 inches in plan, with a thickness of 8 inches. Within this slab, four types of artificial defects were embedded during casting to simulate common defects simulating deterioration in bridge decks: a shallow delamination, a honeycomb, a void, and a deep delamination. The delamination defects were simulated using thin plexiglass inserts placed at specific depths below the top surface (approximately 2.5 inches for the shallow delamination and 6 inches for the deep delamination). The honeycomb region was created by deliberate poor consolidation in one area to create air pockets, and the void was simulated by an inflated bladder that was later removed, leaving an air cavity. The locations and sizes of these defects are shown in Fig. 2, along with a schematic of the slab's reinforcement and construction joints. This controlled specimen allows direct comparison of acoustic signals from known defect areas versus solid (intact) concrete areas. Detailed information about the construction of the slab with defects can be found in Lin et al.[32].

To further validate the applicability of the system under more realistic conditions, an additional concrete beam approximately 6 feet in length was evaluated. Unlike the slab, this beam contained unknown, naturally visible deteriorated regions including cracks and spalls. Its surface was divided into a reference grid and was visually inspected to mark damage-prone areas. This secondary test helped assess how well the system generalized to in situ conditions and to defects not explicitly pre-labeled.

Evaluation of traditional acoustic sounding techniques

In the initial testing phase, traditional manual acoustic sounding using a hammer was employed on the slab. The acoustic response at each impact point was recorded using a high-sensitivity MEMS microphone placed near the test location. Different locations on the slab were impacted multiple times to ensure statistical reliability. Impact signals were recorded at a sampling rate of 44.1 kHz over a 1-second window. In an effort to standardize the excitation and improve signal repeatability, additional tests were conducted using a steel ball mounted on a flexible rod. This setup produced consistent, high-energy impacts and allowed for rapid resetting between tests. The steel ball's sharp acoustic

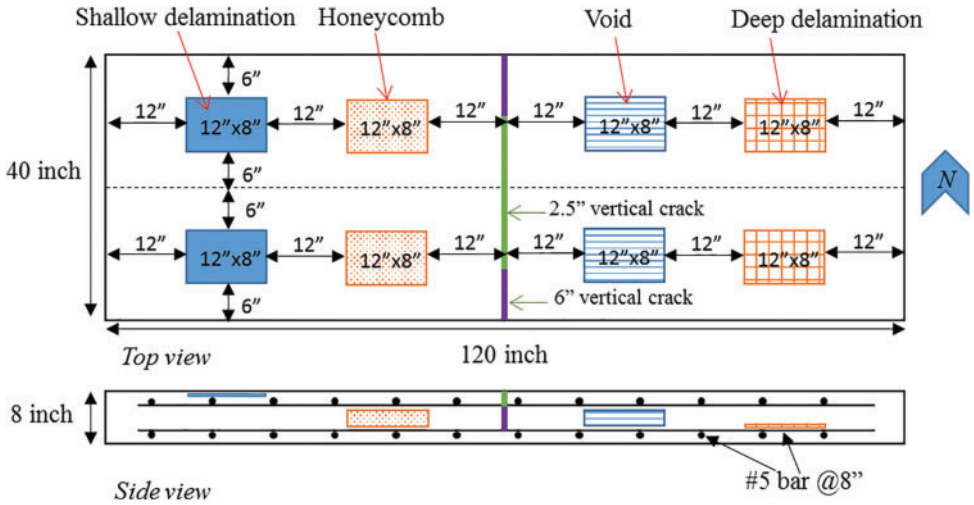

Figure 2. Schematic of the concrete slab specimen with embedded artificial defects, including shallow and deep delamination, honeycombing, and voids

signature and repeatability made it ideal for collecting high-quality reference signals. Across all methods, care was taken to replicate outdoor-like conditions, including the presence of ambient noise and handling variations, to assess signal robustness in practical inspection scenarios.

Signal processing and feature extraction

As data acquisition becomes increasingly automated, the primary challenge in acoustic delamination detection shifts from signal collection to accurate and efficient real-time interpretation. Traditional field methods often rely on auditory cues or basic frequency-domain metrics such as peak frequency. However, these approaches are inherently subjective and highly susceptible to environmental noise and inconsistencies in impact conditions. To overcome these limitations, this study adopted a hybrid signal processing strategy that began with EMD as a front-end noise filter,[33,34] followed by feature extraction using either PSD or Hilbert marginal spectrum (HMS) for frequency-domain analysis, and HHT for energy-based interpretation.

EMD is an adaptive data analysis tool that is commonly used to break down any complicated signal set into several components, which usually pertain to different vibration modes and different physical meanings. These components can also be described as intrinsic mode functions (IMFs), which build a nearly orthogonal basis for the original data

$$y(t) = \sum_{i=1}^{n} x_i(t) + r_n \tag{1}$$

where $y(t)$ is the original signal, $x_i(t)$ is the i_{th} IMF and r_n is the residue.

PSD is a frequency-domain analysis tool that quantifies how the power (energy per unit frequency) of a signal is distributed across different frequencies. It helps identify dominant frequencies and is commonly used in vibration and acoustic analysis. PSD assumes signal stationarity and is calculated as

$$P(f) = \lim_{T\to\infty} |X_T(f)|^2 \tag{2}$$

where $X_T(f)$ is the Fourier transform of the time-limited signal. Although useful for identifying peaks and comparing energy content, PSD does not preserve the time variation of frequency components, which limits its utility in analyzing short, nonstationary signals like impact sounds.

HHT is a two-step method for analysis of nonlinear and nonstationary signals.[35] The first step uses EMD that decomposes the original signal into a finite number of IMFs as shown in Eq. (1). The second step of HHT is the Hilbert transform, which produces an orthogonal pair for each IMF that is phase-shifted by 90°

$$H[x_i(t)] = \frac{1}{\pi}\int_{-\infty}^{\infty} \frac{x_i(\tau)}{t-\tau}\, d\tau \tag{3}$$

The analytic function $A_i(t)$ of any real signal $x(t)$ can be defined as

$$A_i(t) = x_i(t) + jH[x_i(t)] \tag{4}$$

or

$$A_i(t) = a_i(t)\, e^{j\theta_i(t)} \tag{5}$$

where

$$a_i(t) = \sqrt{x_i^2(t) + H^2[x_i(t)]} \tag{6}$$

$$\theta_i(t) = \arctan\frac{H[x_i(t)]}{x_i(t)} \tag{7}$$

The instantaneous frequency can be defined as

$$\omega_i(t) = \frac{d\theta_i(t)}{dt} \tag{8}$$

After performing the Hilbert transformation, the original signal can be obtained from the real part of the analytic function $A_i(t)$. The frequency-time distribution of the amplitude is designated as the Hilbert spectrum $H(\omega, t)$,

$$H(\omega, t) = \mathrm{Re}\left(\sum_{i=1}^{n} a_i(t)\, e^{j\int \omega_i(t)dt}\right) \tag{9}$$

From the Hilbert spectrum, HMS[36] can be defined as

$$H(\omega) = \int_0^T H(\omega, t)\, dt \tag{10}$$

The HMS offers a measure of the amplitude contribution from each frequency over time, while the marginal spectrum provides a measure of the total amplitude (or energy) contribution from each frequency value.

In this study, all acoustic signals recorded by the SASS were first processed using EMD. This adaptive technique separated each raw signal into a finite set of IMFs, each representing local oscillatory behavior. Among these, the first IMF (IMF1) consistently captured the primary transient response triggered by the impact, while the higher-order IMFs typically contained environmental noise, wind-induced vibrations, and mechanical handling artifacts. These noise-dominated IMFs were excluded from further analysis. As a result, EMD functioned as a powerful front-end filter, isolating the most physically meaningful components of the signal prior to spectral interpretation.

With IMF1 extracted, two parallel spectral analysis approaches were applied. First, PSD was computed to quantify how signal energy was distributed across frequencies. This helped identify dominant spectral peaks and allowed for comparative energy-level assessment under different defect conditions. However, PSD assumes stationarity and does not account for time-dependent variations in frequency content. This made it less effective in fully capturing the dynamics of impact-based acoustic signals. To address this limitation, HHT was applied to IMF1, generating the corresponding HMS, which retained the temporal evolution of frequency content while integrating it over time. This provided a more informative view of nonstationary acoustic responses, particularly useful for short-duration events typical of hammer-sounding inspections. Both PSD and HMS revealed distinct frequency bands consistently associated with defect types; for instance, shallow delamination was characterized by elevated energy in the 1.5–3 kHz range. From these processed spectra, a comprehensive set of quantitative features was extracted. These included peak frequency, spectral centroid, mean frequency, and energy content within

predefined diagnostic bands (e.g., 1.5–3, 2–4, and 5–7 kHz). These features were chosen to capture subtle yet consistent spectral differences between sound and defective zones, thereby enhancing the discriminative power of the system.

Although both PSD– and HMS–derived features proved effective in characterizing signal behavior, HMS features consistently provided sharper separation between healthy and defective areas, particularly under noisy or variable field conditions. The combined use of PSD and HMS, both derived from EMD–filtered IMF1, enabled a robust and flexible feature extraction process across varying signal qualities. This integrated framework established a reliable foundation for the subsequent ML–based classification of delamination and other defects.

ML for automated defect classification

A supervised ML approach[37,38] was developed to automatically classify each measurement point as either "defect" or "sound," with the ability to further differentiate specific defect types based on extracted acoustic features. A dataset comprising over 1,100 sample points was compiled from controlled testing on the concrete slab. Each sample corresponded to a known physical location with ground truth labels, such as shallow delamination, deep delamination, honeycomb, void, or intact concrete, and was paired with a set of features extracted from the corresponding acoustic response.

Building on the spectral analysis of signals processed through PSD and the HMS of EMD–filtered IMF1, the features for ML were derived. Several diagnostic frequency ranges were identified: a low-frequency band (~1.5–3 kHz) associated with shallow delamination, a mid-frequency band (~2–4 or 2–5 kHz) often linked with general defect behavior, and higher-frequency bands (5–7 and 6–10 kHz) where intact concrete typically exhibited stronger responses. For each sample, the area under the normalized spectrum within these bands, representing band-limited energy, was computed as input features. Additional features included the dominant frequency, which proved effective in differentiating between sound and defective zones.

Various classification algorithms were tested, including decision trees,[39] SVMs,[40] and ensemble methods.[41] Among these, a decision tree classifier was selected for its strong balance between predictive accuracy and interpretability. The model was trained using 70% of the labeled dataset and evaluated on the remaining 30%. The ML model achieved high accuracy in distinguishing between sound and defective points. Remarkably, the model was also able to identify an unlabeled surface crack on the slab, which was not included in the training dataset. This "unseen" region was correctly flagged as damaged, demonstrating the model's ability to generalize learned patterns beyond explicitly defined categories.

Although more advanced models such as neural networks could be explored in future work, the current dataset size favored simpler classifiers. The decision tree model also offered the advantage of real-time execution on the embedded processor, aligning with the system's design goals of portability and on-device analytics for field deployment.

Design and integration of smart sounding system

Building upon insights from conventional impact testing, a portable SASS was developed to deliver consistent excitation, suppress ambient noise, and automate both data acquisition and defect classification. The system is designed for use on both flat and overhead concrete surfaces, addressing key limitations of traditional methods such as operator subjectivity, inconsistent impact force, and physical fatigue associated with manual chain drag or hammer sounding.

Fig. 3a illustrates the system components and operation. A high-power vibration speaker embedded in a cylindrical acoustic waveguide (approximately 0.5 m in length) functions as the broadband chirp excitation source. When

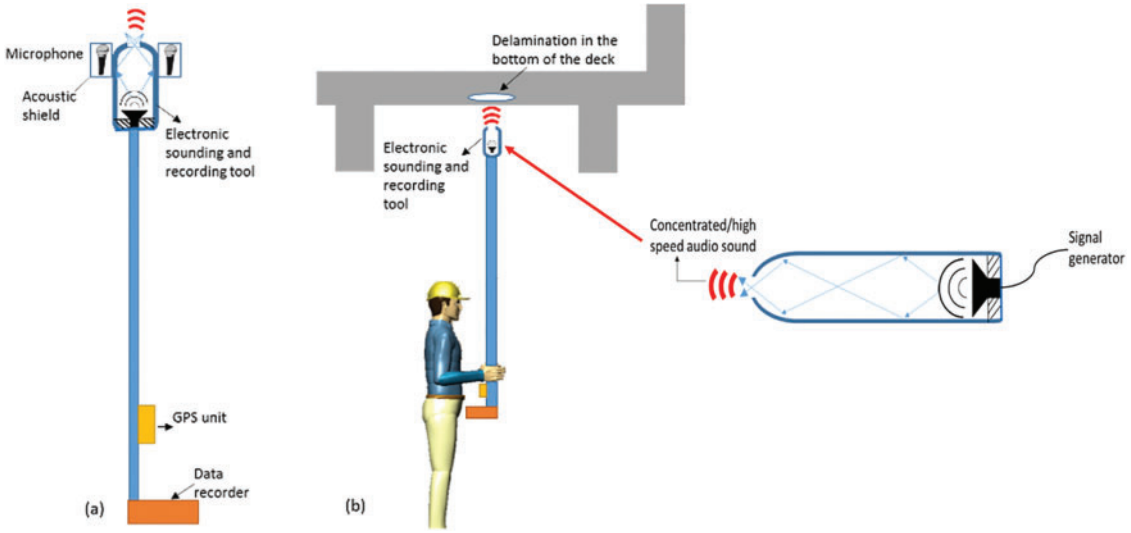

Figure 3. Overview of the Smart Acoustic Sounding System (SASS): (a) system components including chirp speaker, MEMS microphone, and SLAM camera; (b) pole-mounted setup for inspecting overhead concrete surfaces

the tube is pressed against a concrete surface, it concentrates acoustic energy into the material, analogous to a localized shock wave. A programmable signal generator emits chirp signals sweeping from approximately 500 Hz to 16 kHz, covering the key resonance frequencies for typical defects like delamination (~1–3 kHz), while also capturing higher-frequency reflections from intact areas. The chirp signal can be initiated via a graphical user interface or a remote-control interface, ensuring consistency and eliminating manual impacts.

A MEMS microphone, positioned near the tube opening and enclosed within an acoustic shield, records the structural response. Foam gaskets at the rim provide sealed contact, minimizing airborne noise and improving signal-to-noise ratio. A stereovision tracking camera mounted near the device captures the spatial coordinates of each test point using visual SLAM. As the system is swept across a surface, a virtual inspection grid is automatically generated, eliminating the need for manual marking or gridding.

On-board hardware manages signal generation, data acquisition, and real-time processing. Once activated, the system executes the full inspection loop: chirp emission, acoustic response recording, EMD–based signal filtering, spectral feature extraction, defect classification, and real-time visualization of results. This workflow typically completes within a few seconds per test point. The unit is lightweight, battery-powered, and designed for field use. It can be operated by hand or mounted on an extendable pole, as illustrated in Fig. 3b, for testing the undersides of bridge decks or other overhead surfaces. Its integrated processing and sensing capabilities remove the need for external computing tools or surface preparation, enabling rapid and repeatable inspections.

Results and Discussion

Laboratory testing of the developed detection algorithm

To establish baseline performance and identify acoustic signatures for various defect types, laboratory experiments were conducted using manual hammer sounding. The test setup is shown in Fig. 4. A handheld hammer was used to strike the surface of a large concrete slab embedded with engineered defects. A common vocal microphone wrapped with foam to suppress ambient noise was positioned near the impact point to capture the structural acoustic response. The microphone was connected via USB to a laptop for signal acquisition and real-time recording at a sampling rate of 44.1 kHz (Fig. 4a). The basic defect detection mechanism is illustrated in Fig. 4b, where impact-induced stress waves reflect off subsurface anomalies, and the returning signal is recorded for analysis.

Fig. 5 presents the Fourier spectra of acoustic responses from five distinct test locations: a sound area (no delamination), a shallow delamination, a honeycomb region, a void, and a deep delamination. The spectrum corresponding to the intact (sound) area (Fig. 5a) shows distinct high-frequency peaks, primarily above 4 kHz, indicating strong resonant behavior of solid concrete. In contrast, shallow delamination (Fig. 5b) and honeycomb (Fig. 5c) cases exhibit broader, flatter spectra with most energy concentrated below 4 kHz. These low-frequency components are associated with disrupted wave propagation caused by internal defects. The spectrum for the void (Fig. 5d) also displays prominent energy in the low-frequency range, with reduced high-frequency response. Notably, deep delamination (Fig. 5e) shows spectral characteristics more similar to intact concrete than to shallow defects, suggesting that manual sounding may be less sensitive to defects located deep beneath the surface. In all defect cases, multiple low-frequency peaks appear below 2.5 kHz, likely corresponding to flexural modes and environmental or residual noise.

To further isolate and interpret these signals, EMD was applied. The results, shown in Fig. 6, decompose each raw signal into IMFs, enabling adaptive separation of signal and noise content. The original PSD plots (first column) reveal total frequency content. In most cases, the IMF1 (second column) captures the dominant acoustic signal corresponding to the actual impact response. Subsequent IMFs (IMF2 and IMF3) (third and fourth columns) primarily capture low-amplitude noise, confirming the effectiveness of EMD as a noise filtering tool. Across all defect types, the IMF1

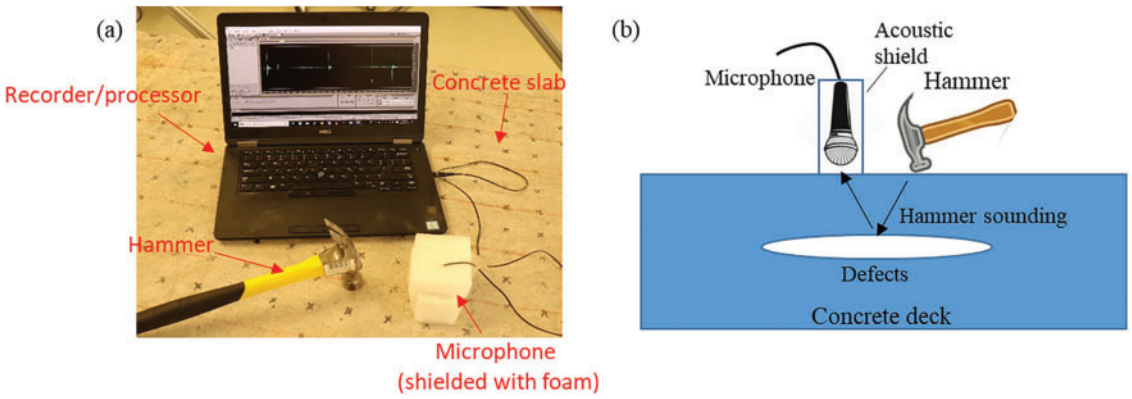

Figure 4. Manual acoustic sounding setup: (a) sounding instruments; (b) conceptual illustration of acoustic wave propagation

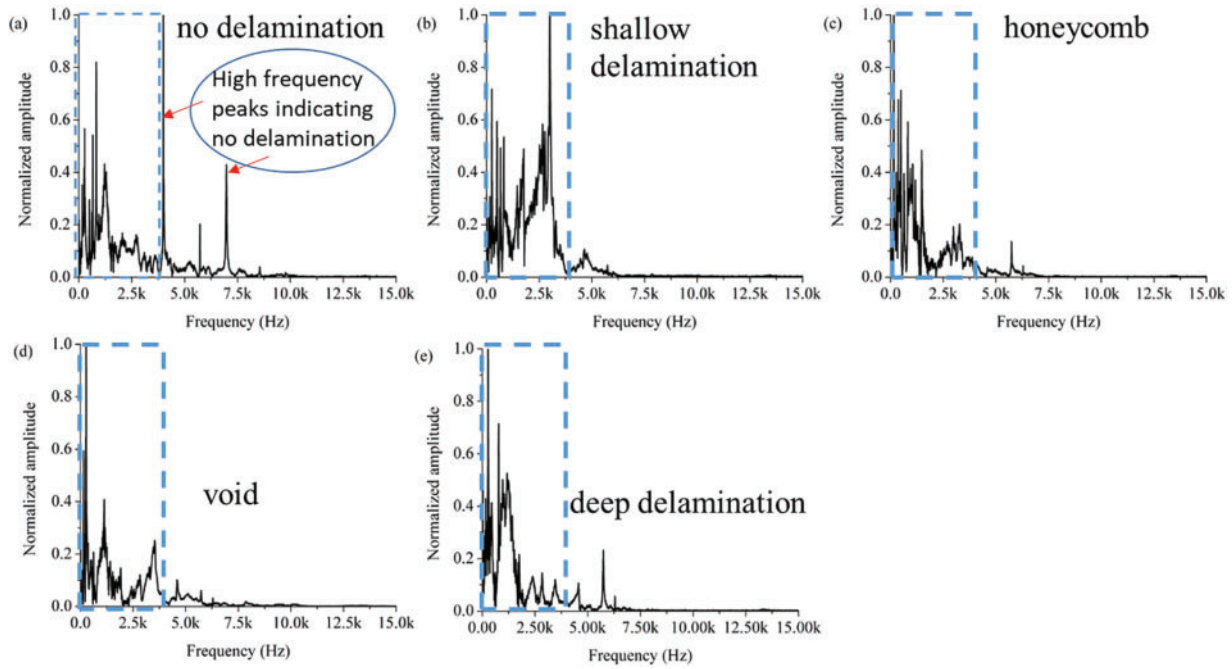

Figure 5. Frequency spectra from hammer sounding at five locations: (a) intact concrete, (b) shallow delamination, (c) honeycomb, (d) void, and (e) deep delamination

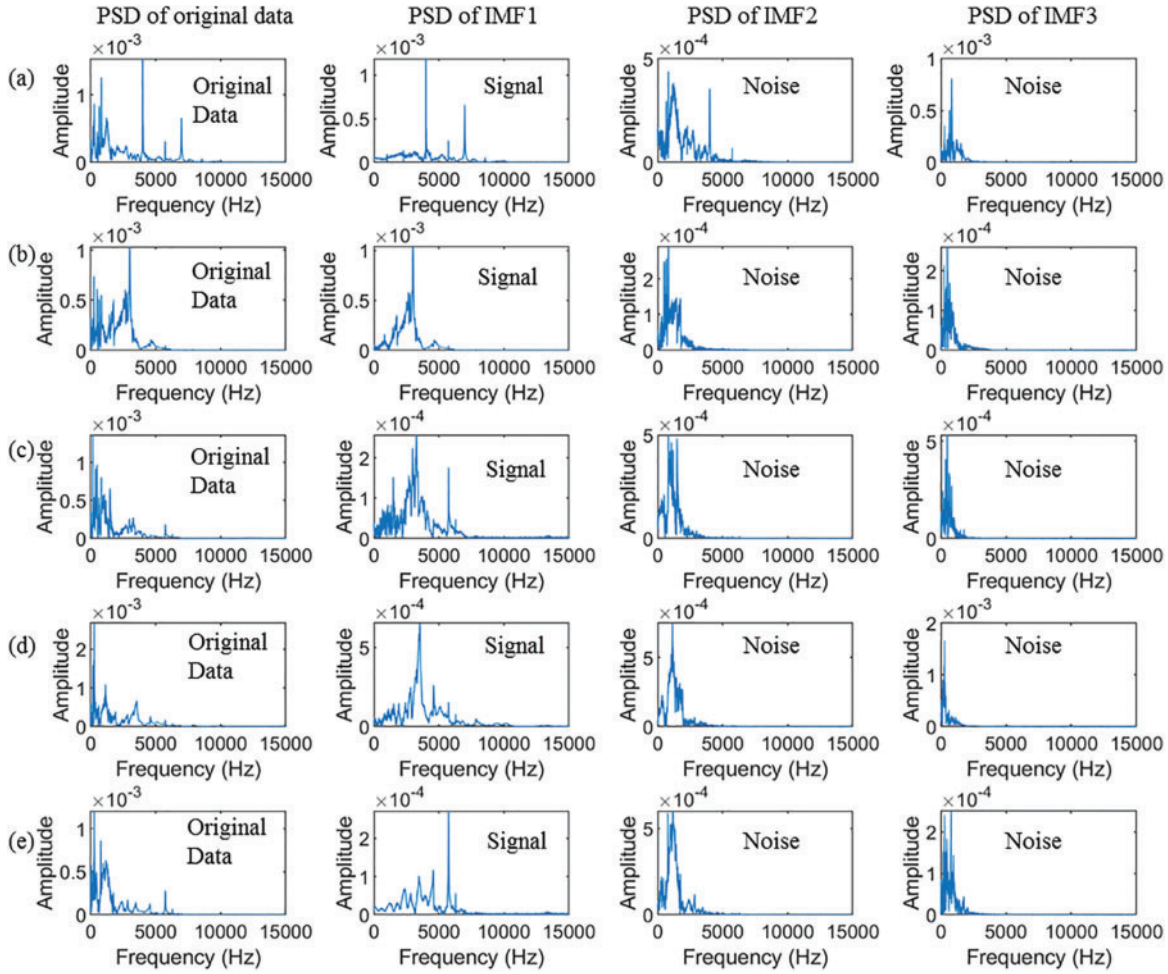

Figure 6. EMD results for hammer sounding signals across five defect conditions: (a) intact, (b) shallow delamination, (c) honeycomb, (d) void, and (e) deep delamination

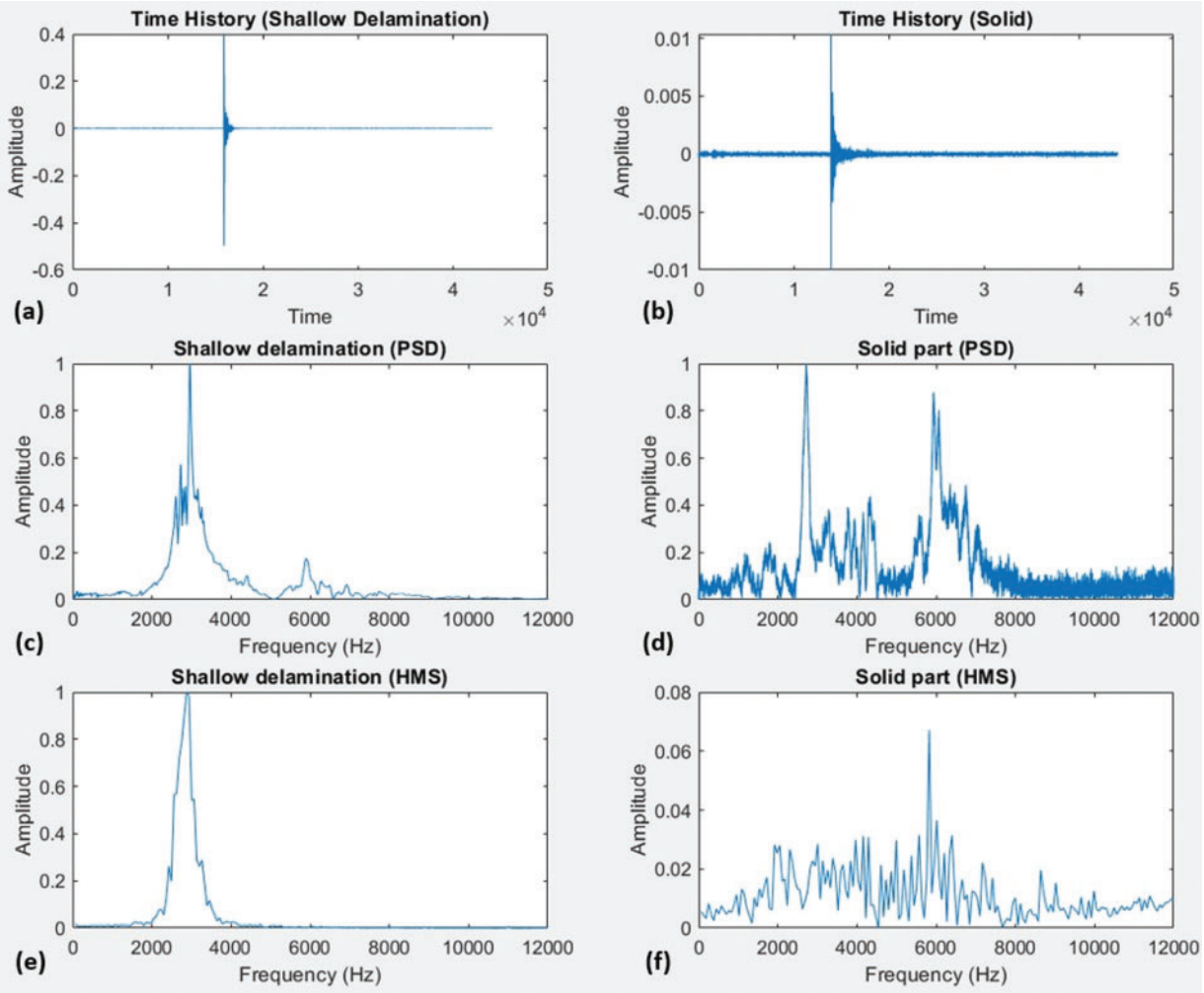

Figure 7. Comparison of time and frequency responses for shallow delamination and solid zones: (a, b) time histories, (c, d) PSD plots, and (e, f) HMS plots

spectra preserve the key low-frequency resonance signatures observed in raw data while suppressing random noise. The differences between defect and sound conditions become more apparent post-EMD, demonstrating how filtering and decomposition enhance interpretability. These processed signals later serve as inputs for feature extraction and ML classification.

The time-history plots of signals for shallow delamination and solid surfaces, shown in Figs. 7a and 7b, respectively, show clear differences between the delaminated and solid areas. The delaminated region has a higher peak and vibrates for a longer time, while the solid area shows a faster decay and lower amplitude. After applying EMD, the IMF1 was used to calculate both the PSD and the HMS (Figs. 7c–7f). These plots highlight important differences: the delamination case shows stronger energy in the lower frequency range (1.5–3 kHz), while the solid region spreads energy across higher frequencies above 3 kHz. In particular, the HMS plot for the solid part shows more scattered and weaker low-frequency energy. These results support using a frequency threshold and ML for accurate defect classification.

Frequency-based damage index visualization using PSD and HMS

To enhance the detection and spatial visualization of subsurface defects, a damage index metric was developed based on frequency-domain analysis. This index is defined as the ratio of spectral energy in the 2–4 kHz band to the total energy in the 0–8 kHz range and was computed using both the PSD and HMS of IMF1 signals. The 2–4 kHz frequency range was chosen based on prior observations indicating that shallow delamination consistently exhibits dominant energy in this band.

Fig. 8a presents the layout of the concrete slab used in this study, showing the locations of engineered defects, including shallow delamination, honeycomb, void, and deep delamination, as well as two surface cracks that occurred naturally during curing. At each grid point, a hammer was used to excite the slab, and the acoustic response was recorded using a foam-shielded microphone. The recorded signals were decomposed using EMD to isolate the dominant response (IMF1), from which spectral features were extracted for index calculation. The resulting PSD–based damage index map is shown in Fig. 8b. Ground-truth defect locations

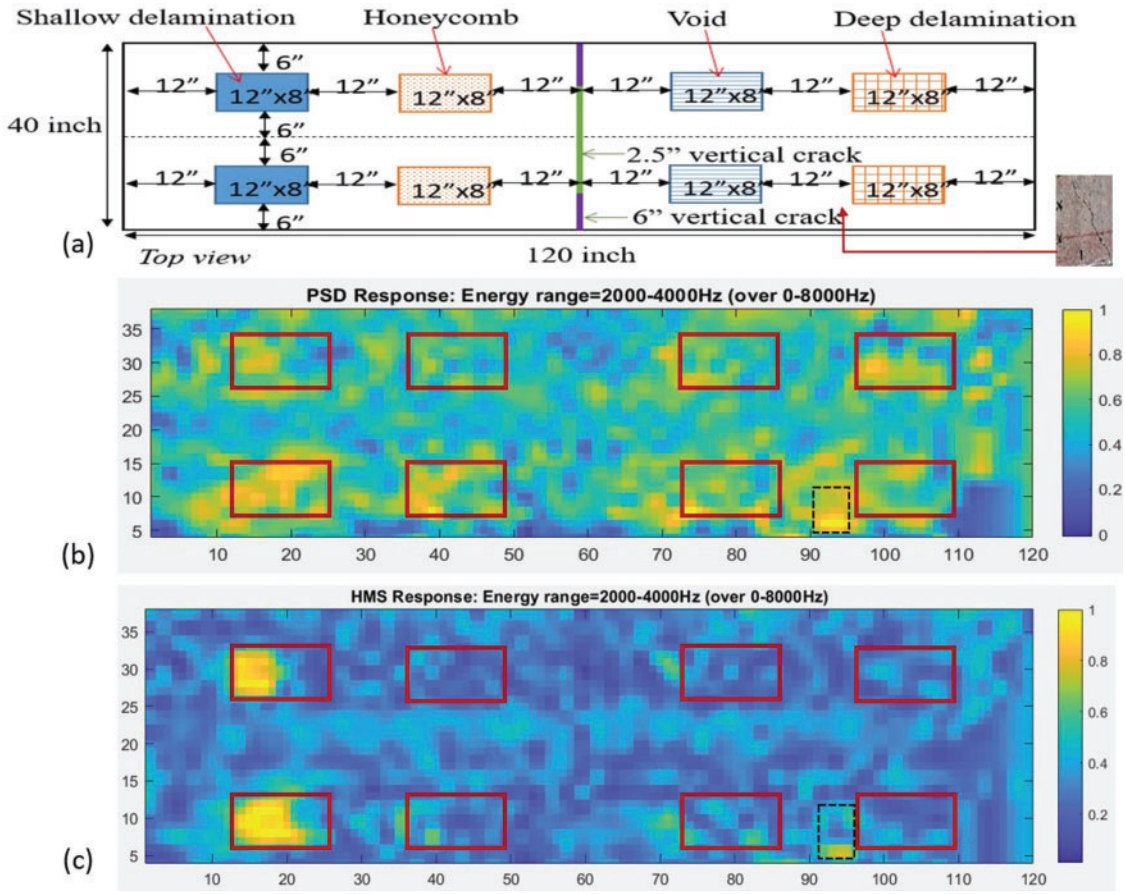

Figure 8. (a) Defect layout of the concrete slab, (b) damage map visualization using PSD, and (c) damage map using HMS

are marked with red rectangles. The PSD plot effectively highlights several damage zones, particularly the shallow delamination areas and a horizontal crack near the lower right region, which appears as a bright patch. However, the deep delamination region is less distinguishable, consistent with earlier findings that hammer sounding is relatively less effective in detecting deeper defects. Fig. 8c shows the HMS–based damage index map, which leverages time-integrated energy from the nonstationary acoustic signal. The shallow delamination zones appear more localized and better defined in the HMS plot compared to the PSD results. Additionally, the background (non-defect) regions show reduced noise and higher contrast, enhancing defect visibility. However, HMS displays reduced sensitivity to voids and deep delamination, as expected from its frequency-energy focus.

In summary, while both PSD and HMS provide valuable insights into damage localization, HMS offers enhanced clarity and spatial contrast for detecting shallow delamination, often the most critical for early maintenance intervention. PSD, on the other hand, is more responsive to broader spectral anomalies such as cracks and voids. Together, these complementary techniques support improved diagnosis of surface-level and subsurface deterioration, with HMS being especially useful for identifying early-stage, non-visible damage.

ML–based defect detection algorithm

While earlier studies[42,43] often relied on a single frequency band, typically 1.5–3 kHz, to identify damaged regions in concrete structures, this approach has limitations due to its subjectivity and narrow scope. Although this frequency range has shown utility in identifying shallow delamination, the effectiveness of such fixed-band approaches can vary depending on the defect type and surrounding material conditions. In response to this limitation, the present study introduces an ML framework that leverages multiple diagnostic frequency bands and statistical signal features to automatically classify defects with higher robustness and generalizability.

To train and validate the ML model, a dataset of more than 1100 acoustic response points was collected from a controlled concrete slab at the FHWA Resource Center. The slab measured 40 inches by 120 inches and included various engineered defects such as shallow delamination, honeycombs, voids, and deep delamination. Acoustic signals were acquired every two inches across the grid, ensuring dense spatial coverage. Each recorded data point was paired with a ground-truth label corresponding to its physical condition. The acoustic responses were preprocessed using EMD, and features were extracted from the IMF1 to ensure noise-filtered spectral data.

Instead of selecting a single spectral band, the ML model utilized multiple frequency-based features, including the area under the normalized spectral curve across several bands such as 1.5–3, 2–4, 2.5–4, 5–7, and 6–10 kHz. Additional time-domain statistics, such as signal mean and variance, were also computed. These features enabled the model to learn characteristic patterns associated with both sound and defective zones. A decision tree classifier was chosen for its balance of accuracy and interpretability, and was trained using 70% of the dataset, with the remaining 30% used for validation.

The classifier achieved high accuracy in identifying damaged zones across the slab. As shown in Fig. 9, the predicted damage regions (highlighted in yellow) align closely with the actual defect zones marked by red dashed boxes. Importantly, the model also detected an unlabeled vertical surface crack at the center of the slab, demonstrating its ability to generalize beyond the training data. This finding highlights the model's strength in learning structural damage patterns and applying them to novel conditions.

The successful detection of both known and unknown defect areas underscores the potential of supervised ML models in acoustic-based NDE. Unlike fixed-band techniques, the data-driven approach captures subtle differences in signal characteristics across a range of frequencies. This approach, thus, allows for more nuanced and accurate classification of various defect types, including those not explicitly represented during training. The ability to operate in real-time on embedded processors further supports the field deployment of such models as part of portable inspection systems.

Chirp-based excitation and signal processing for automated defect detection

The use of chirp-based excitation represents a significant advancement over traditional hammer sounding for concrete inspection. The experimental setup shown in Fig. 10 demonstrates a portable electronic configuration, where a vibration speaker generates a chirp signal directed at the concrete surface, and the resulting acoustic response is captured using a foam-shielded microphone. Compared to manual impact methods, this approach offers repeatability, reduced operator dependency, and the potential for robotic deployment. The chirp signal, spanning 0–10 kHz, can be triggered repeatedly without variation in amplitude, allowing for controlled, high-resolution frequency analysis.

Fig. 11 presents the source chirp and the corresponding recorded response, with the latter showing the system's sensitivity to subsurface conditions. By applying cross-correlation

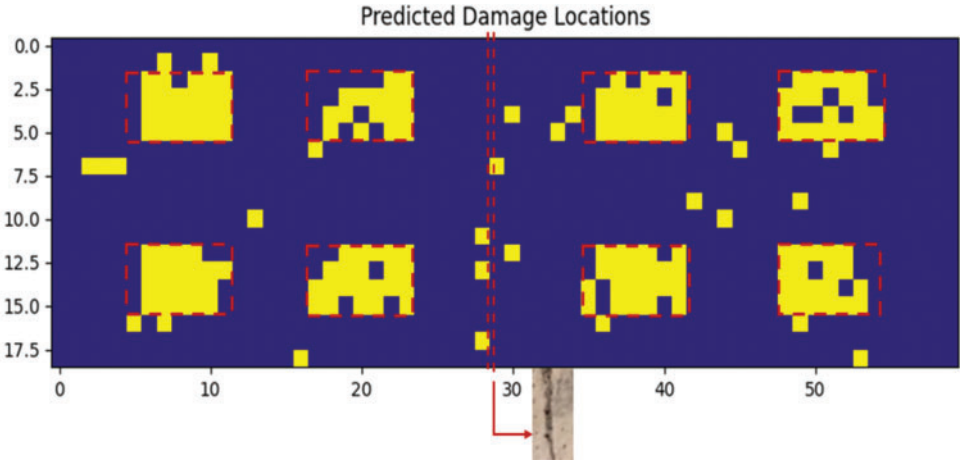

Figure 9. Machine learning–based defect prediction map from hammer acoustic data

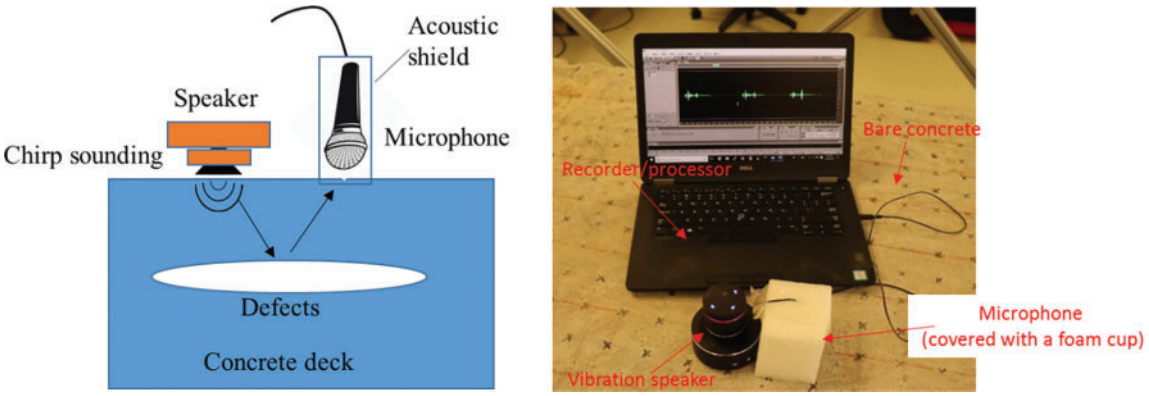

Figure 10. Chirp excitation test setup: (a) SASS components during slab testing and (b) schematic of acoustic signal emission and response capture

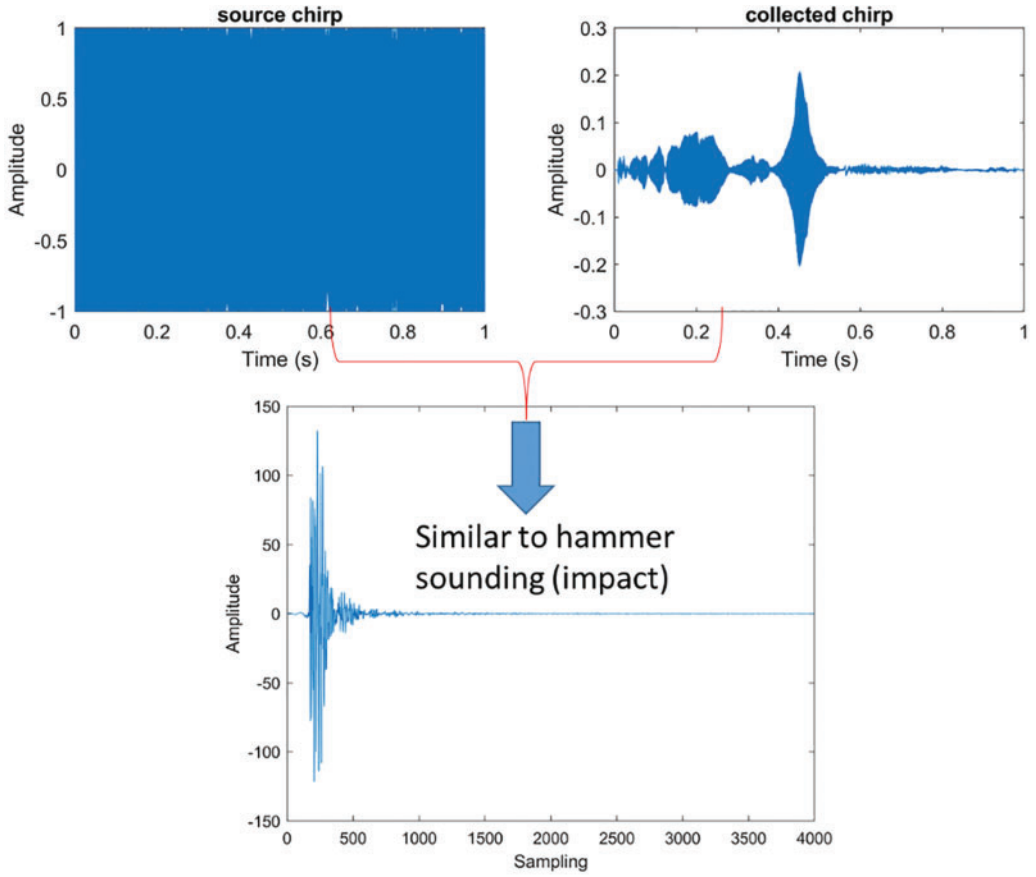

Figure 11. Illustration of cross-correlation of chirp sounding data

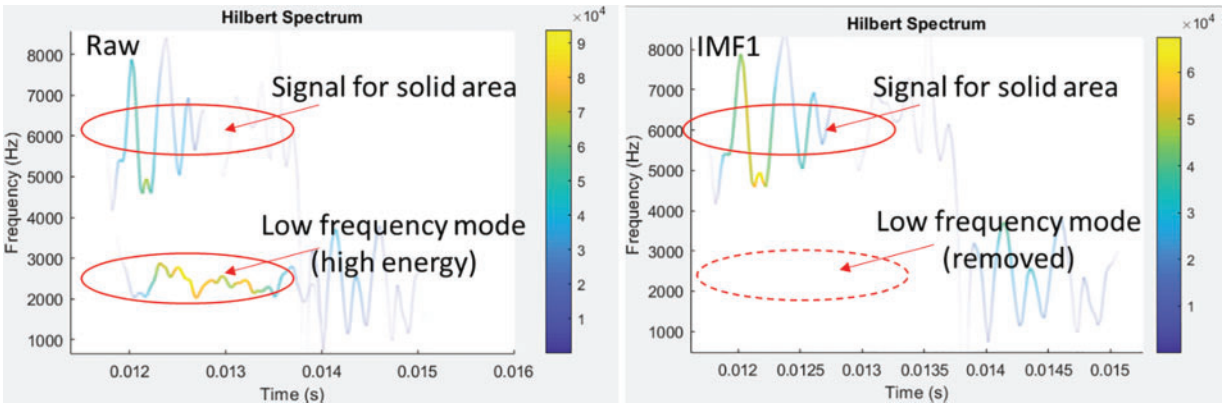

Figure 12. Noise suppression in chirp data using empirical mode Decomposition (EMD)

between the transmitted and received chirp signals, phase variations were removed, enhancing the signal-to-noise ratio. Notably, the resulting waveform closely resembles that of hammer sounding but exhibits much less ambient noise.

To further isolate structural responses, EMD was applied to the correlated chirp signal, followed by HHT analysis. As depicted in Figs. 12 and 13, the EMD method effectively removed low-frequency noise, with IMF1 containing most of the signal energy related to structural vibrations. The HHT spectrum of the filtered data (Fig. 13) revealed dominant frequencies in the 6–7 kHz range for solid regions and 2–3 kHz for delaminated areas, consistent with earlier hammer-based findings.

Fig. 13 confirms that EMD-filtered chirp responses are comparable in behavior to hammer sounding while offering higher repeatability and reduced noise interference. These insights validate chirp excitation as a reliable alternative for detecting shallow delamination, with EMD and HHT providing robust signal filtering and time-frequency resolution. This combined methodology enhances the detection capability of the smart sounding system and paves the way for automated, scalable NDE solutions for bridge decks and concrete structures.

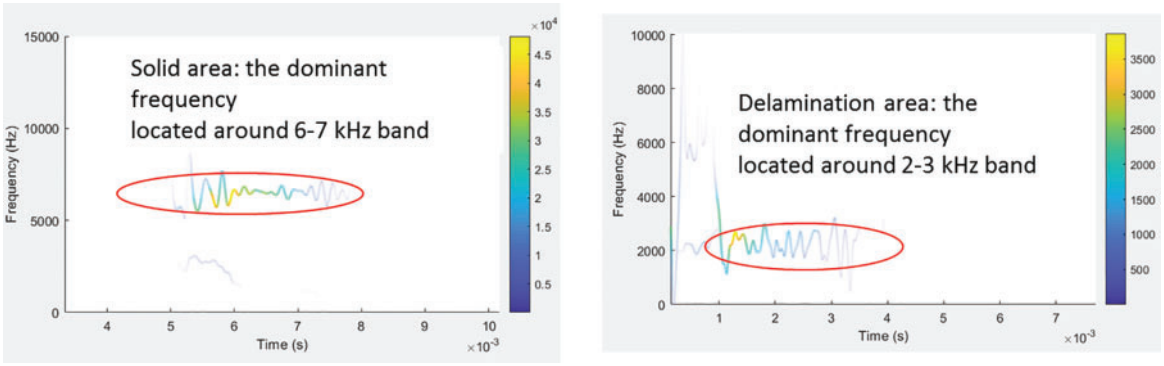

Figure 13. HHT spectrum showing instantaneous energy distribution from the EMD-filtered chirp signal for solid and delamination areas

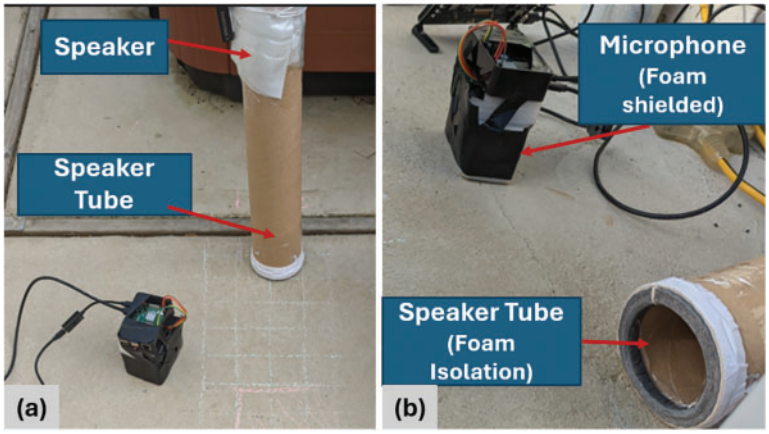

Figure 14. (a) SASS testing on concrete slab and (b) foam insulation ring added to reduce acoustic leakage from speaker tube

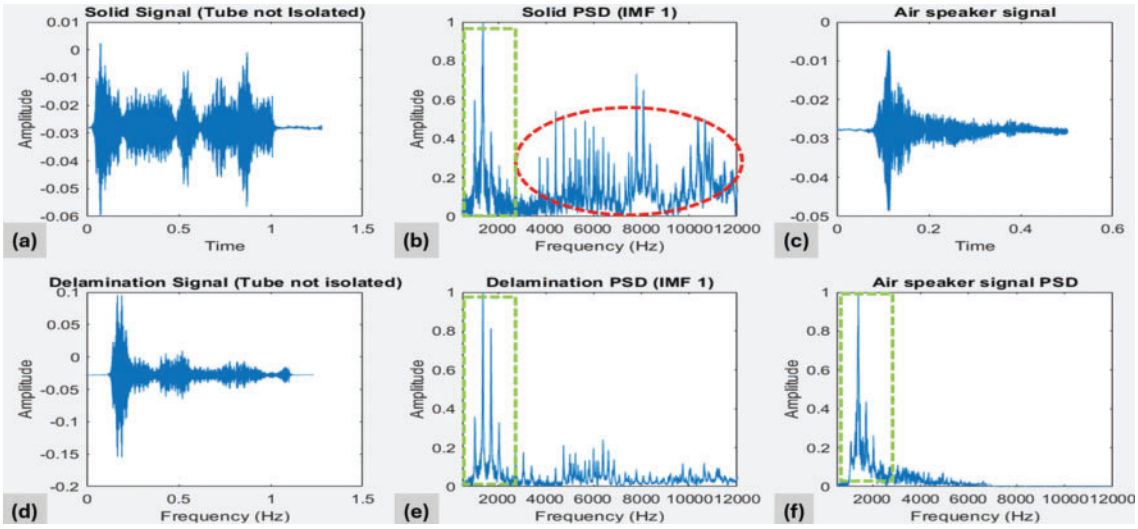

Figure 15. Effect of speaker isolation on acoustic signals: (a, c, d) time-domain responses and (b, e, f) PSD–based frequency spectra for solid and defective conditions

Smart sounding tool evaluation

Controlled experiments were conducted to evaluate the performance of the proposed SASS under both laboratory and field conditions. The testing involved two scenarios: (1) a concrete slab embedded with engineered defects and (2) a deteriorated in situ concrete beam located in an existing building. These scenarios allowed assessment of system behavior in both controlled and practical environments.

Fig. 14 shows the test setup on the concrete slab. Initial testing of the concrete slab showed that solid

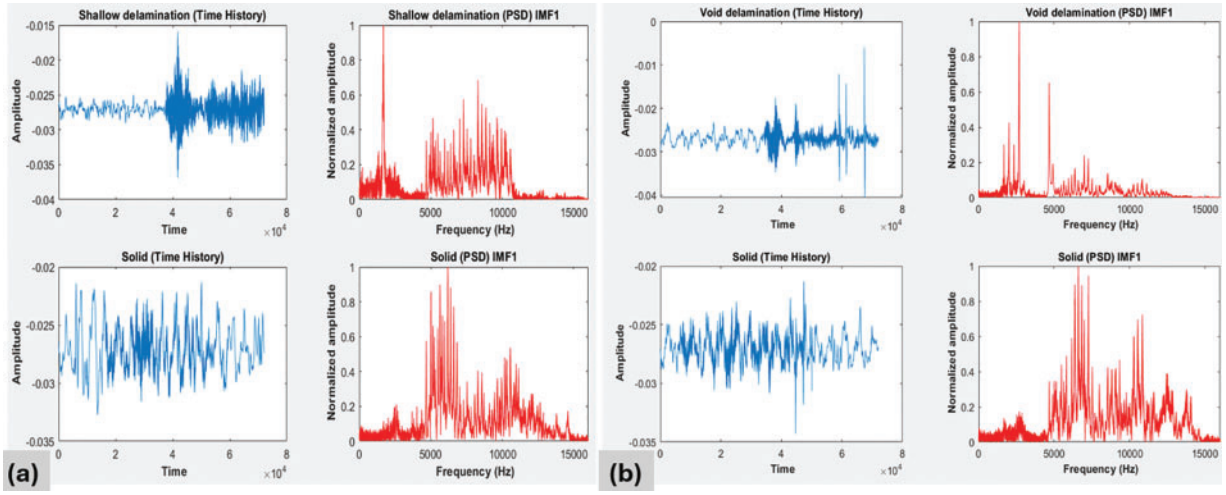

Figure 16. Frequency-based comparison of shallow and void delamination signals versus solid regions using PSD

Figure 17. Deteriorated concrete beam at CCNY campus

regions generated higher excitation beyond 3 kHz, corroborating past research findings. However, inconsistencies were observed in the lower frequency domain. Unexpectedly, defective areas did not exhibit significantly stronger responses at frequencies below 3 kHz, and instead, showed a similar spectral profile to the solid zones. Upon further investigation, it was determined that acoustic leakage from the speaker, due to inadequate sealing between the speaker tube and the rough concrete surface, was contaminating the signal. The sound, bypassing the concrete, directly reached the microphone, resulting in misleading low-frequency components in the PSD. Fig. 15 illustrates this issue, showing that the airborne noise emitted by the speaker dominates the frequencies below the 3 kHz region, masking the surface vibrations critical for defect detection.

To mitigate this interference, a circular foam ring was installed at the base of the speaker tube to ensure tighter acoustic isolation between the speaker and the concrete surface (see Fig. 14b). This modification significantly reduced noise intrusion and allowed for more accurate measurement of surface-transmitted signals. With the enhanced setup, subsequent testing produced results that aligned closely with theoretical and empirical expectations. As shown in Fig. 16, shallow delamination and voids now exhibited prominent spectral peaks below 3 kHz, while solid regions maintained dominant responses above this threshold. This clear separation validated the application of a 3 kHz threshold as a reliable criterion for distinguishing defective zones from intact concrete.

Field testing on a damaged beam

The refined system was field-tested on a deteriorated concrete beam as shown in Fig. 17. A grid pattern of 6 × 6-inch squares (Fig. 19) was used for mapping, and signals were collected at each node using the smart sounding tool. The frequency-domain response from each grid cell was analyzed by integrating spectral energy in the 1.5–3 kHz band, a frequency range previously associated with shallow defects.

The PSD and HMS outputs from EMD–filtered IMF1 signals revealed strong correspondence between low-frequency excitation and known damaged areas (Fig. 20). Delaminated zones showed elevated spectral energy within the 1.5–3 kHz range, while solid areas showed dominant responses above this range. HMS plots provided complementary visual evidence of energy concentration in defect-prone locations.

The smart sounding system accurately identified damaged regions, which were visually represented using a color-coded grid in Fig. 19. Purple zones corresponded to visibly damaged regions such as delamination, cracks, and spalling (e.g., grids 4, 9, 14, and 32), while yellow indicated moderate or potential damage. Interestingly, some surface-visible cracks (e.g., grid 6) were not flagged as defects, likely due to intact bonding behind the surface, highlighting the system's sensitivity to unbonded or hollow regions rather than superficial cracking. Proper microphone-speaker isolation proved essential. Initial tests suffered from airborne speaker noise leakage, which was resolved by the foam ring (Fig. 18), yielding significantly cleaner signals and more

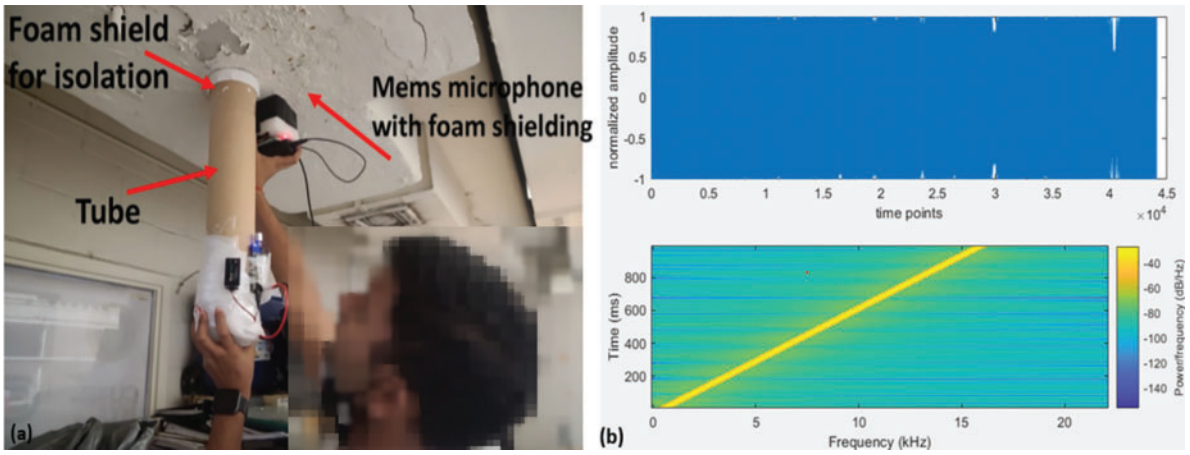

Figure 18. (a) SASS field testing on damaged beam and (b) chirp excitation characteristics used for signal analysis

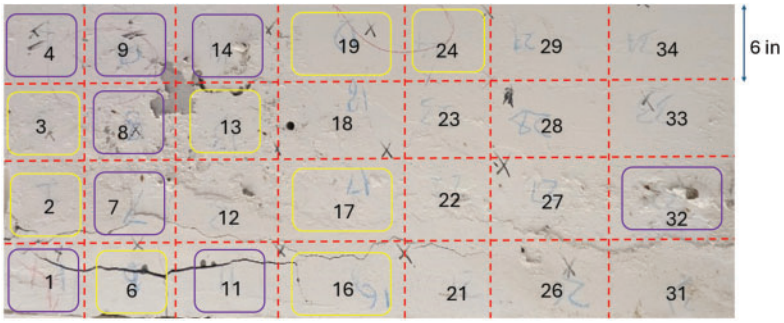

Figure 19. Defect mapping of deteriorated concrete beam using color-coded grid overlay with chirp-based acoustic data

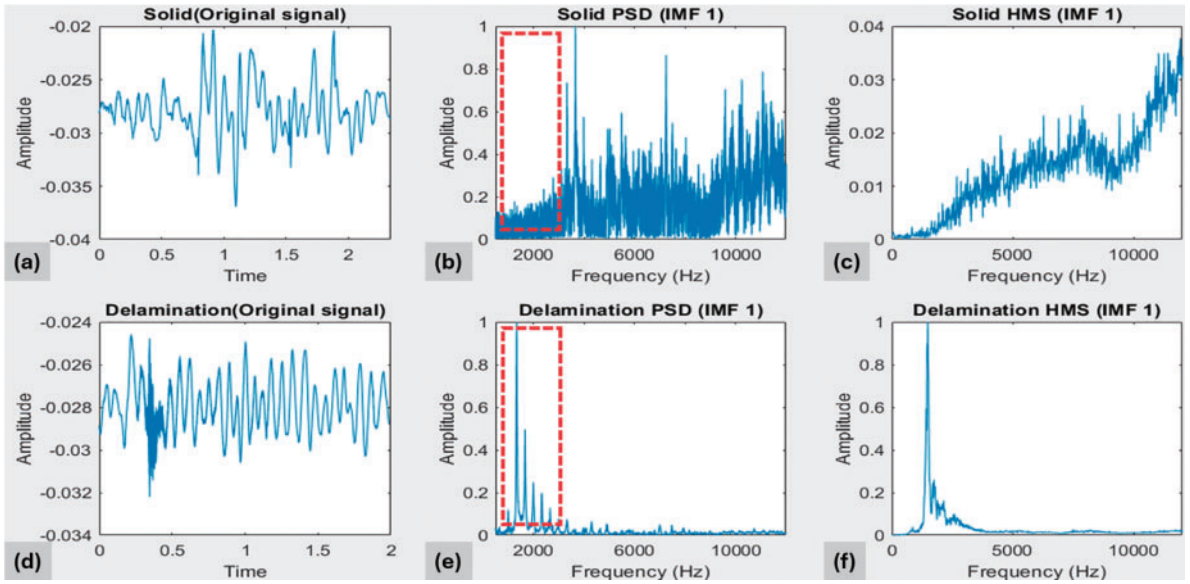

Figure 20. Time and frequency responses for solid and delaminated zones: (a, d) time-domain signals, (b, e) PSD plots, and (c, f) HMS plots after EMD filtering

accurate damage differentiation. Overall, the system provided rapid, repeatable, and visually interpretable feedback on shallow defect conditions. Future improvements, such as slimmer tubes, directional speakers, or higher-resolution microphones, could enhance detection depth and resolution, particularly in complex structural settings.

Discussion of novelty and contributions

The SASS developed in this study represents a notable departure from traditional manual impact sounding techniques by addressing key challenges of subjectivity, repeatability, and data interpretation. A primary innovation lies in the use of a programmable chirp signal, which allows consistent

excitation across all test points without dependence on operator skill or variability in force application. This uniformity is crucial for reliable comparison across large surfaces and under varying field conditions.

The integration of EMD and HHT enables the decomposition of noisy, nonstationary acoustic signals into intrinsic components, isolating frequency bands linked to common defects like delamination and voids. HMS analysis, derived from these IMFs, proved superior to conventional PSD in distinguishing closely spaced spectral features. In particular, defect zones showed elevated responses in the 1.5–3 kHz range, which were accurately captured using IMF1–based transformations. The enhanced resolution provided by HMS improved both interpretability and ML model classification performance. The visual SLAM camera further contributes to operational efficiency by automating spatial referencing, allowing direct mapping of test points and defect regions without manual gridding or drawing overlays. This spatial automation supports real-time mapping of deterioration and lays the foundation for digital asset management and robotic inspections.

However, limitations remain. The system currently depends on surface contact through a foam interface, which may limit usage in inaccessible or irregular geometries. Detection is primarily sensitive to near-surface flaws, and expanding its applicability to deeper defects would require broader frequency excitation or alternative techniques such as impact-echo. Field deployment also demands improved environmental shielding and robustness of the electronic components to handle temperature, dust, and moisture variability.

Conclusions

This research demonstrates the feasibility and effectiveness of a SASS for detecting and mapping subsurface defects in concrete. The combination of broadband chirp excitation, EMD–HHT–based signal analysis, and automated spatial tracking enables a portable, objective, and high-resolution inspection method. Controlled laboratory experiments and field validation in an existing building confirmed the system's ability to distinguish solid and defective regions based on frequency-domain features, particularly those in the lower-frequency range associated with delamination. ML classifiers trained on HMS features achieved high accuracy, even generalizing to untrained defect types, demonstrating the robustness of the spectral signatures. The system eliminates many of the manual steps involved in traditional acoustic inspections, such as grid layout, subjective sound interpretation, and post-processing, offering a scalable solution for large-scale bridge assessments. The ability to map results in real-time supports timely maintenance decisions and improved record-keeping for long-term monitoring.

Future work will focus on expanding the training dataset, integrating more advanced classification models, and miniaturizing hardware components to facilitate deployment in constrained environments. Enhancements to system durability and automation will be essential for widespread adoption by transportation agencies and infrastructure managers.

Acknowledegments

This research was conducted as part of the INSPIRE University Transportation Center (UTC) project on autonomous bridge inspection. The authors gratefully acknowledge the funding support from the U.S. Department of Transportation, Office of the Assistant Secretary for Research and Technology (USDOT/OST-R) under Grant No. 69A3551747126 through INSPIRE University Transportation Center (http://inspire-utc.mst.edu) at Missouri University of Science and Technology. We also acknowledge a partial support through a grant from the Social and Economic Mobility for People And Communities through Transportation (SEMPACT) University Transportation Research Center (UTRC), which is the designated United State Department of Transportation UTC for the federal region 2 and is housed at the City College of New York.

Disclaimer

The views, opinions, findings, and conclusions expressed in this paper are solely those of the authors and do not represent the official policy or position of the USDOT/OST-R or any state or other entity.

References

[1] American Society of Civil Engineers. Bridges: 2025 Infrastructure Report Card; 2025. https://infrastructurereportcard.org/cat-item/bridges-infrastructure/.

[2] Federal Highway Administration. *Incorporating Nondestructive Evaluation Methods Into Bridge Deck Preservation Strategies (FHWA-HRT-24-186)*. Washington, DC, United States: Department of Transportation, Federal Highway Administration, Office of Research, Development, and Technology; 2024. doi:10.21949/1521525.

[3] Tong F, XU XM, Luk BL, Liu KP. Evaluation of tile–wall bonding integrity based on impact acoustics and support vector machine. *Sens Actuat A: Phys*. 2008;144(1):97–104. doi:10.1016/j.sna.2008.01.020.

[4] Luk BL, Liu K, Tong F, Man K. Impact-acoustics inspection of tile-wall bonding integrity via wavelet transform and hidden Markov models. *J Sound Vib*. 2010;329(10):1954–1967.

[5] Luk B, Liu K, Tong F. Rapid evaluation of tile-wall bonding integrity using multiple-head impact acoustic method. *NDT & E Int*. 44(3):297–304.

[6] Popovics JS. *Investigation of a Full Lane Acoustic Scanning Method for Bridge Deck Nondestructive Evaluation*. Washington, D.C: Transportation Research Board, Final Report for Highway IDEA Project 134, Transportation Research Board; 2010.

[7] Sun H, Zhu J, Ham S. Automated acoustic scanning system for delamination detection in concrete bridge decks. *J Bridge Eng*. 2018;23(6):04018027.

[8] Larsen JL, McElderry J, Baxter JS, Guthrie WS, Mazzeo BA. Automated sounding for concrete bridge

deck inspection through a multi-channel, continuously moving platform. *NDT & E Int*. 2020;109(32):102177. doi:10.1016/j.ndteint.2019.102177.

[9] Hendricks LJ, Baxter JS, Chou Y, Thomas M, Boekweg E, Guthrie WS, Mazzeo BA. High-speed acoustic impact-echo sounding of concrete bridge decks. *J Nondestruct Eval*. 2020;39:1–12.

[10] Blaney S, Gupta R. Unmanned aerial vehicle-based sounding of subsurface concrete defects. *J Acoust Soc Am*. 2018;144(3):1190–1197.

[11] Akamatsu R, Sugimoto T, Utagawa N, Katakura K. Proposal of non contact inspection method for concrete structures using high-power directional sound source and scanning laser Doppler vibrometer. *Jpn J Appl Phys*. 2013;52(7S):07HC12.

[12] Dai X, Zhu J, Haberman MR. A focused electric spark source for non-contact stress wave excitation in solids. *J Acoust Soc Am*. 2013;134(6):EL513–EL519.

[13] Dabous SA, Feroz S. Condition monitoring of bridges with non-contact testing technologies. *Autom Constr*. 2020;116:103224.

[14] Michaels JE, Lee SJ, Hall JS, Michaels TE. Multi-mode and multi-frequency guided wave imaging via chirp excitations. In: *Proceedings, Health Monitoring of Structural and Biological Systems, International Society for Optics and Photonics*; 2011; San Diego, CA, United States. pp. 79840I.

[15] Michaels TE, Michaels JE, Lee SJ, Chen X. Chirp generated acoustic wavefield images. *Proceedings, Health Monitoring of Structural and Biological Systems, International Society for Optics and Photonics*; 2011; San Diego, CA, United States. pp. 79840I.

[16] Michaels JE, Lee SJ, Croxford AJ, Wilcox PD. Chirp excitation of ultrasonic guided waves. *Ultrasonics*. 2013;53(1):265–270.

[17] Feng B, Ribeiro AL, Ramos HG. A new method to detect delamination in composites using chirp-excited Lamb wave and wavelet analysis. *NDT & E Int*. 2018;100:64–73.

[18] Mizutani Y, Inokawa S. A fundamental study of an inspection method for thin-walled structures using lamb waves induced by chirp signals. *Proceedings, Third International Conference on Experimental Mechanics and Third Conference of the Asian Committee on Experimental Mechanics, International Society for Optics and Photonics*; 2005; Singapore. pp. 520–528.

[19] Muramatsu M, Uchida S, Takahashi Y. Noncontact detection of concrete flaws by neural network classification of laser doppler vibrometer signals. *Eng Res Express*. 2020;2(2):025017.

[20] Ye J, Kobayashi T, Iwata M, Tsuda H, Murakawa M. Computerized hammer sounding interpretation for concrete assessment with online machine learning. *Sensors*. 2018;18(3):833.

[21] Alhebrawi MN, Huang H, Wu Z. Artificial intelligence enhanced automatic identification for concrete cracks using acoustic impact hammer testing. *J Civil Struct Health Monit*. 2023;13(2):469–484. doi:10.1007/s13349-022-00651-8.

[22] Vy V, Lee Y, Yoon H. Crack detection of concrete structures using acoustic emission sensors and convolutional neural networks. In: *The International Conference on Sustainable Civil Engineering and Architecture*. Singapore: Springer Nature Singapore; Jul 2023:1306–1314.

[23] Habib MA, Hasan MJ, Kim JM. A lightweight deep learning-based approach for concrete crack characterization using acoustic emission signals. *IEEE Access*. 2021;9:104029–104050.

[24] Jafari F, Dorafshan S. Bridge inspection and defect recognition with using impact echo data, probability, and Naive Bayes classifiers. *Infrastructures*. 2021;6(9):132. doi:10.3390/infrastructures6090132.

[25] Barbosh M, Dunphy K, Sadhu A. Acoustic emission-based damage localization using wavelet-assisted deep learning. *J Infrastruct Preserv Resil*. 2022;3(1):6. doi:10.1186/s43065-022-00051-8.

[26] Hoxha E, Feng J, Sanakov D, Xiao J. *Robotic Inspection and Subsurface Defect Mapping Using Impact-Echo and Ground Penetrating Radar*. IEEE Robotics and Automation Letters; 2023.

[27] Lavadiya DN, Dorafshan S. Deep learning models for analysis of non-destructive evaluation data to evaluate reinforced concrete bridge decks: a survey. *Eng Rep*. 2023. doi: 10.1002/eng2.12608.

[28] Scherr JF, Grosse CU. Delamination detection on a concrete bridge deck using impact echo scanning. *Struct Concr*. 2021;22(2):806–812.

[29] Scherr JF, Grosse CU, Popovics JS. Evaluation of non-destructive impact-echo data from the national bridge inventory. *Dev Built Environ*. 2024;18:100468.

[30] Kumar D, Agrawal A. Advancing bridge infrastructure management through artificial intelligence: a comprehensive review. *Int J Bridge Eng, Manag Res*. 2025;2(3):214250021–1:18. doi:10.70465/ber.v2i3.45.

[31] Lehman M. The American Society of Civil Engineers' report card on America's infrastructure. In: *Women in Infrastructure*. Cham: Springer International Publishing; 2022:5–21. doi:10.1007/978-3-030-92821-6_2

[32] Lin S, Meng D, Choi H, Shams S, Azari H. Laboratory assessment of nine methods for nondestructive evaluation of concrete bridge decks with overlays. *Constr Build Mater*. 2018;188:966–982.

[33] Cao R, Agrawal AK. Defect detection of concrete structures through sounding data analytics. In: *Proceedings of the 9th International Conference on Structural Health Monitoring of Intelligent Infrastructure*; August 4–7, 2019; St. Louis, MO, USA: ISHMII.

[34] Zhang M, Zhang Q, Li J, Xu J, Zheng J. Classification of acoustic emission signals in wood damage and fracture process based on empirical mode decomposition, discrete wavelet transform methods, and selected features. *J Wood Sci*. 2021;67(1):1–13. doi:10.1186/s10086-021-01990-8.

[35] Huang NE, Wu Z. A review on Hilbert-Huang transform: method and its applications to geophysical studies. *Rev Geophys*. 2008;46(2):RG2006. doi:10.1029/2007RG000228

[36] Li H, Zhang Y, Zheng H. Hilbert-Huang transform and marginal spectrum for detection and diagnosis of localized defects in roller bearings. *J Mech Sci Technol*. 2009;23(2):291–301. doi:10.1007/s12206-008-1110-5.

[37] Nasteski V. An overview of the supervised machine learning methods. *Horizons. b*. 2017;4(51–62):56.

[38] Kotsiantis SB, Zaharakis I, Pintelas P. Supervised machine learning: a review of classification techniques. *Emerg Artif Intell Appl Comput Eng*. 2007;160(1):3–24.

[39] Charbuty B, Abdulazeez A. Classification based on decision tree algorithm for machine learning. *J Appl Sci Technol Trends*. 2021;2(01):20–28.

[40] Suthaharan S. Support vector machine. In: *Machine Learning Models and Algorithms for Big Data Classification: Thinking with Examples for Effective Learning*. Boston, MA: Springer US; 2023:207–235.

[41] Dietterich TG. Ensemble methods in machine learning. In: *International Workshop on Multiple Classifier Systems*. Berlin, Heidelberg: Springer Berlin Heidelberg; June 2023:1–15. doi:10.1007/3-540-45014-9_1

[42] Kumar D, Agrawal AK, Cao R, Zhan L, Wei J. Damage detection in concrete slab using smart sounding. In: Rizzo P, Milazzo A. (Eds.), *European Workshop on Structural Health Monitoring. EWSHM 2022. Lecture Notes in Civil Engineering*. vol. 254. Cham: Springer; 2023. doi:10.1007/978-3-031-07258-1_11

[43] Agrawal AK. *Quantitative Bridge Inspection Ratings using Autonomous Robotic Systems. Project IM-2. 1*. Rolla, Missouri, USA: Missouri University of Science and Technology; 2022. https://scholarsmine.mst.edu/project_im-2/1.

BER the international journal of bridge engineering management and research

Dynamic Investigations before and after the Strengthening of a Masonry Arch Bridge

Paolo Borlenghi and Carmelo Gentile*

Submitted: 20 August 2025 **Accepted:** 15 September 2025 **Publication date:** 10 October 2025

DOI: 10.70465/ber.v2i4.56

Abstract: The bridge crossing the Gesso River is a multi-span masonry arch bridge built in the 19th century in Cuneo, Piedmont, Italy. Due to extended local degradation and damage, the bridge recently underwent a significant strengthening intervention. Ambient vibration tests were performed both before and after the strengthening to assess the effectiveness of the repairs. The paper presents the results of the dynamic investigations, identifying the modal characteristics of the masonry bridge through different techniques. The pre-intervention analysis revealed clear anomalies, including a sort of "frequency splitting" phenomenon and irregularities in the mode shapes that were localized in the regions of maximum masonry decay. After the strengthening works, the identified modal parameters showed an increase in natural frequencies, along with the resolution of previously identified mode shape irregularities, indicating a clear improvement in the bridge's structural condition.

As a final remark, the presented results highlight the value of operational modal analysis (OMA) as a nondestructive tool for validating the effectiveness of rehabilitation measures.

Author keywords: Historical constructions; rehabilitation; repair; nondestructive testing; operational modal analysis

Introduction

The safety of bridges is a key concern worldwide, and particularly in Italy, where a recent survey documented more than 240 bridge collapses between 2000 and 2023.[1] This evidence highlights the importance of developing effective investigation and rehabilitation strategies for in-service bridges. Within this context, operational modal analysis (OMA) is widely recognized as a powerful tool for the nondestructive assessment of civil engineering structures (see, e.g., Magalhães and Cunha[2]; Rainieri et al.[3]). Generally speaking, OMA consists of estimating the modal characteristics of structures from the dynamic responses measured under operational conditions. The noninvasive nature of OMA, coupled with advances in sensing technologies and the development of numerical methods, has led to its widespread application across various structural typologies and disciplines. Notable examples include the condition assessment of existing bridges[4–8] and footbridges,[9–11] the continuous monitoring of structures for damage identification purposes,[12–14] the development of digital twins for key infrastructures,[15–17] and the evaluation of design choices or future loading scenarios.[18–22]

Despite these advancements, the number of studies applying OMA to evaluate the effectiveness of strengthening interventions remains limited, especially concerning masonry arch bridges. To the best of the authors' knowledge, no published research has specifically addressed the pre- and post-evaluation of the dynamic behavior of a masonry arch bridge using OMA.

Previous studies on reinforced concrete (RC) bridges have shown that the impact of strengthening interventions on dynamic properties can vary significantly according to the structural scheme and the intervention techniques. For instance, Zanardo et al.[23] observed that strengthening a 4-span continuous RC bridge with carbon fiber-reinforced polymer laminate strips resulted in negligible changes (less than 1%) in 2 out of 5 identified natural frequencies, while others showed frequency increases of up to 11%. Similarly, Cury et al.[24] found that additional longitudinal prestressing in a prestressed concrete (PSC) box girder bridge had minimal effects on its modal parameters. Conversely, Cury et al.[25] reported the occurrence of a substantial increase in natural frequencies, up to 15%, following the replacement of elastomeric bearings and expansion joints in a simply supported PSC bridge.

Similarly, research on historical steel bridges[26,27] has shown that structural rehabilitation can lead to a substantial increase in natural frequencies, up to +30%, as well as a significant decrease (–17%), highlighting the crucial role of modal masses.

In masonry structures, the effects of strengthening can be even more significant. For example, Ramos et al.[28] observed

*Corresponding Author: Carmelo Gentile.
Email: carmelo.gentile@polimi.it
Department of Architecture, Built Environment and Construction Engineering (DABC), Politecnico di Milano, Milan, Italy

Discussion period open till six months from the publication date. Please submit separate discussion for each individual paper. This paper is a part of the Vol. 2 of the International Journal of Bridge Engineering, Management and Research (BER), ISSN 3065-0569.

a 50% increase in natural frequencies and a 40% decrease in damping in a masonry tower after rehabilitation works involving lime injection and the installation of ties, likely due to crack closure and the subsequent increase in stiffness. Ercan[29] reported drastic changes in the modal behavior of a stone masonry building after the addition of RC beams at floor levels and the substitution of the roof. Similarly, Namlı and Aras[30] identified substantial increases in modal frequencies—up to 21%—in a masonry school building following the application of RC layers by shotcreting. Conversely, Masciotta et al.[31] found that only limited changes in the modal properties of a historical masonry chimney were induced by the reconstruction of damaged parts and mortar injections, with remarkable variations being observed only for high-frequency local modes.

Given the complexity and variability of masonry structures, evaluating the dynamic response of those structures before and after repair or strengthening is a topic of significant interest. Furthermore, performing an intervention on masonry bridges may be characterized by more constraints compared to buildings, often leading to complex projects being realized without closing the bridge. In this context, OMA is crucial for correctly identifying the pre-intervention structural issues and evaluating whether the solution adopted has been able to solve them (post-intervention). Although several researchers[32–38] have investigated the dynamic characteristics of masonry bridges using OMA, studies specifically addressing the comparison of modal parameters before and after an intervention are still missing.

This paper presents the results of dynamic investigations conducted on a historical multi-span masonry arch bridge, the bridge over the Gesso River in Cuneo, Italy (Figs. 1 and 2), before and after a significant strengthening intervention. The study highlights the retrofit effects by examining the changes in modal parameters. More specifically, a clear increase in natural frequency is observed after the intervention, as well as the disappearance of some mode shapes' anomalies.

The Bridge Over the Gesso River (Cuneo, Italy)

The historic bridge over the Gesso River in Cuneo (Figs. 1 and 2) is one of the two structures that cross the river near the entrance to the historic center of the city. The structure belongs to the Provincial Route SP422 and connects the districts of Borgo San Giuseppe and Cuneo Altopiano. It is managed by the Province of Cuneo, and it is still heavily used by both the traffic in the province and the traffic entering/exiting the densely populated area of the Municipality of Cuneo.

The investigated bridge was built between 1853 and 1856 and is protected by Piedmont's Superintendence of Cultural Heritage. Due to the increased vehicular traffic, a new RC arch bridge was built in 1996 alongside the original structure on the upstream side. The two bridges are independent and share only the base of the piers.

As shown in the geometrical representations in Fig. 2, the bridge under study is approximately 115 m long (including abutments), with a single carriageway 7.30 m wide and two lanes. It consists of three arches with spans of 24 m and two piers placed in the riverbed. The pier height from the foundation level is approximately 10.60 m, and their width along the longitudinal direction is 4.80 m. The piers of the two bridges are connected to each other for the first 6.40 m above the foundation level, while the remaining upper structures are completely independent (this detail is visible in the pictures in Fig. 1).

As known from past inspections, the masonry bridge suffered various decay phenomena, including scouring and common damage due to the aging of the material. Starting in 2018, the Province of Cuneo planned various interventions aimed at solving the observed structural issues. First, measures to prevent riverbed erosion were adopted, whereas the strengthening of the superstructure was subsequently planned. In October 2019, a first series of dynamic tests was performed by the authors to evaluate the modal properties of the structure, highlighting possible critical issues and providing indications for the intervention design.

In preparation for the dynamic tests, visual inspections were performed (Fig. 3). The arch barrels were generally characterized by superficial damage affecting durability, such as black crust, the presence of vegetation, different surface weathering, and diffuse efflorescence. In addition, a severe deterioration of the masonry was localized at the skewback of arch A3 on the side of pier P2 (Fig. 3b).

The strengthening of the bridge (Fig. 4) included the installation of four steel strips at the intrados of each arch barrel, together with the reconstruction of missing masonry portions. Specifically, the local dismantling and reconstruction (often called "scuci-cuci") was applied to fill gaps and restore continuity among damaged masonry portions. In addition, transverse bars were added to connect the external arches with the rest of the arch barrels, ensuring the monolithic behavior of the vaults. Finally, material restoration was carried out using traditional methods, involving cleaning by hydro-washing to remove traces of limestone on the bricks, biocidal treatment to eliminate vegetation, moss, and lichen from masonry surfaces, and protective treatment of decorative stone elements in the form of carved lion heads.

Ambient Vibration Tests and Modal Identification

Ambient vibration tests (AVTs) were performed on October 28th, 2019, and March 4th, 2024, with the main objectives of identifying the dynamic characteristics of the bridge (i.e., natural frequencies, mode shapes, and damping ratios) and assessing their variation after the repair intervention. Notwithstanding the relatively low level of vibration induced by vehicular passages, river flow, wind, and micro-tremors, as well as the high vertical and transverse stiffness of the masonry bridge, AVTs proved to be fully suitable for modal identification.

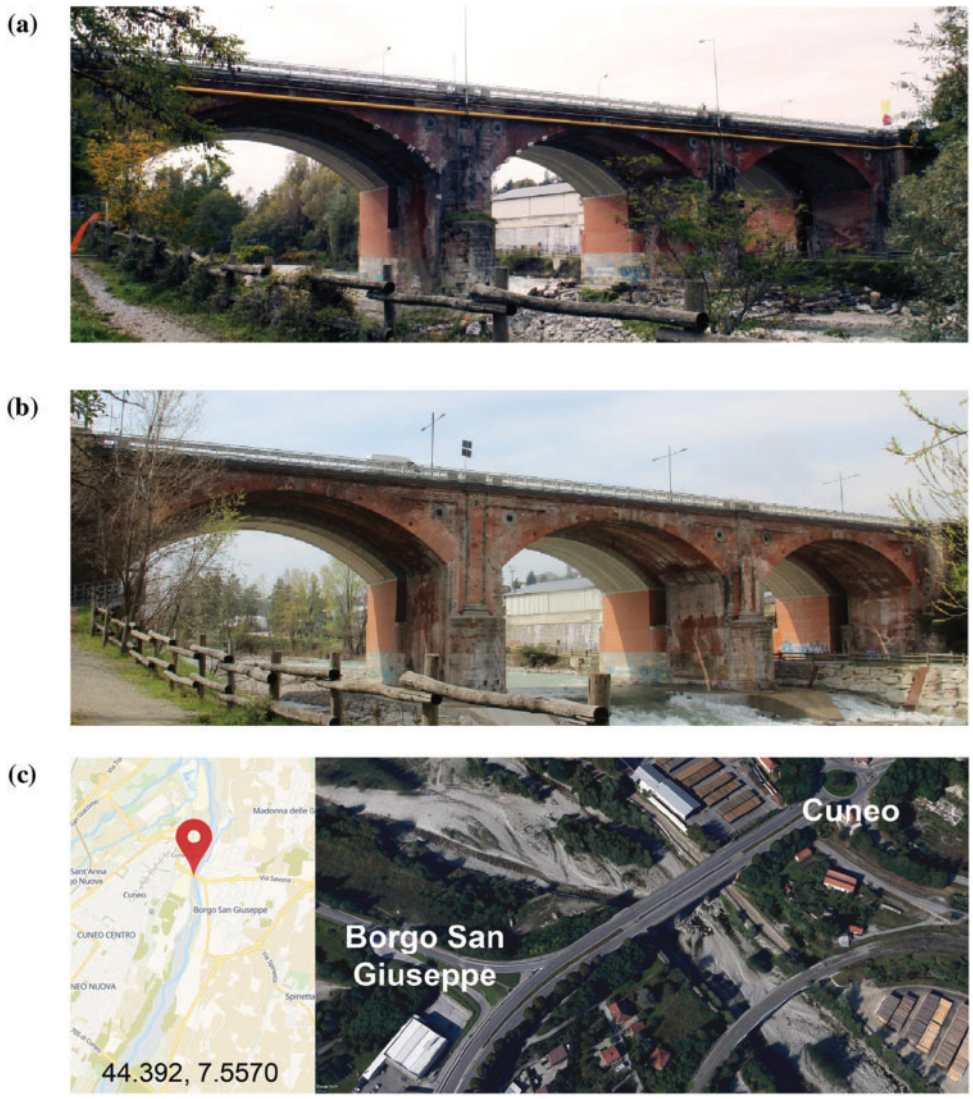

Figure 1. Views from the downstream of the bridge over the Gesso River (Cuneo, Italy) before (a) and after (b) the repair interventions, and (c) bridge location

Experimental procedures

The experimental procedures adopted for the two tests included the measurement of the horizontal and vertical responses of the bridge under operational conditions: due to the presence of sidewalks on both sides, neither traffic interruption nor traffic restrictions were required. Overall, the bridge was instrumented with 17 highly sensitive piezoelectric accelerometers, according to the two measuring setups shown in Fig. 5. The first setup was mainly aimed at characterizing the horizontal response of the structure, with 11 transversal and 6 vertical accelerometers. The second setup was devoted to describing the vertical vibration modes with a higher accuracy, involving 12 vertical and 3 transversal accelerometers. During both setups, 6 vertical (A3, A8, A13, and A15–A17 in Fig. 5) and 3 transversal (A2, A7, and A12 in Fig. 5) accelerometers were used as reference transducers.

The AVTs were conducted using a multichannel acquisition system based on NI9234 devices (24-bit resolution, 102 dB dynamic range, and anti-aliasing filters). The sensors adopted were uniaxial piezoelectric accelerometers (WR model 731A) with 10 V/g sensitivity and ±0.50 g peak acceleration, even though sensors with lower sensitivity could also be suitable. In addition, each sensor was connected to a power unit amplifier (WR model P31) aimed at enhancing the performance of the measuring chain. This unit provided constant current to power the accelerometer's internal amplifier, signal amplification, and selective filtering.

The sampling frequency adopted was equal to 200 Hz, which is more than sufficient for the considered structure, whose dominant frequencies are below 20 Hz. During both tests, the dynamic response of the bridge was recorded for about 90 minutes for each measuring setup.

Data processing and operational modal analysis techniques

The modal identification was performed using the accelerations mainly induced by the regular vehicular traffic on time

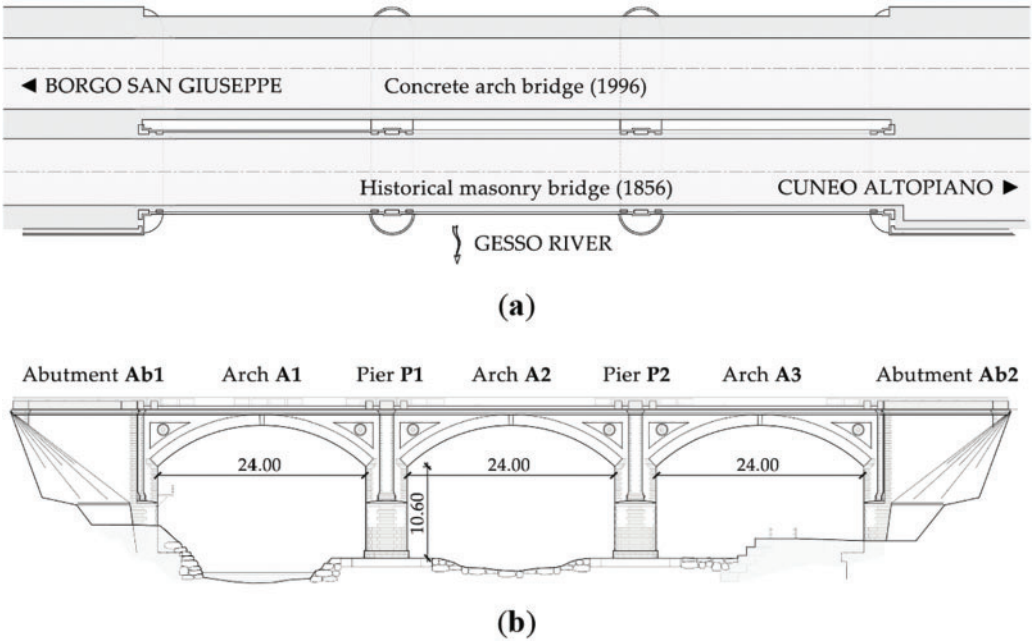

Figure 2. Geometry of the bridge over the Gesso River (Cuneo, Italy): (a) plan and (b) downstream elevation (dimensions in m)

Figure 3. Damages observed at the top of pier P2: (a) general view from downstream and (b) detail of the decayed masonry of the arch A3 skewback (on the right)

Figure 4. Strengthening works: (a) view from downstream of arches A2–A3 and pier P2 and (b) the four steel strips and the transverse connections of the external arch

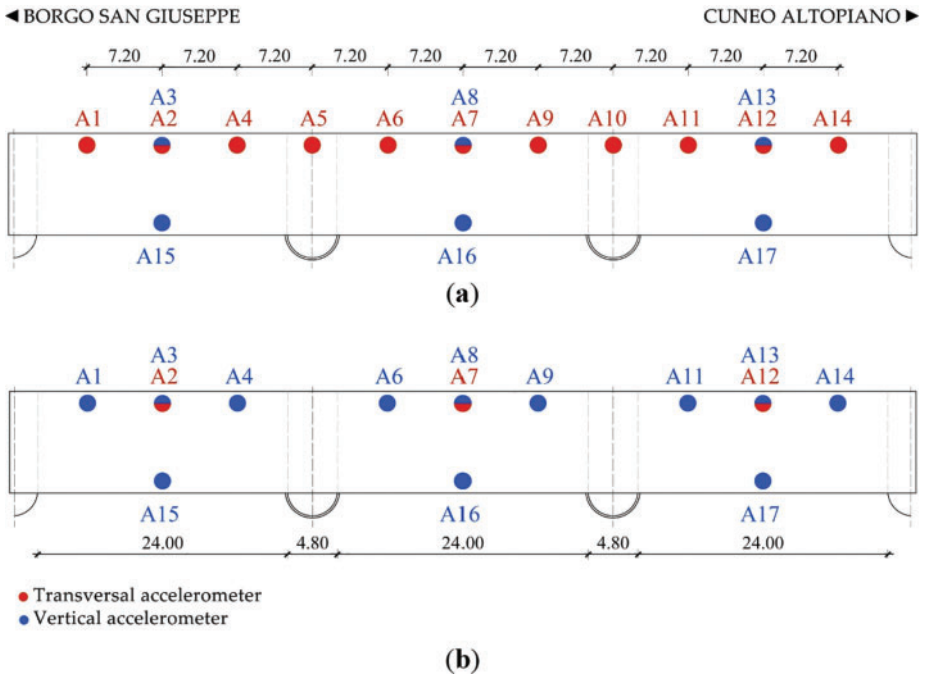

Figure 5. Sensor's layout adopted during the dynamic tests: different configurations to characterize both the transversal (a) and vertical (b) responses

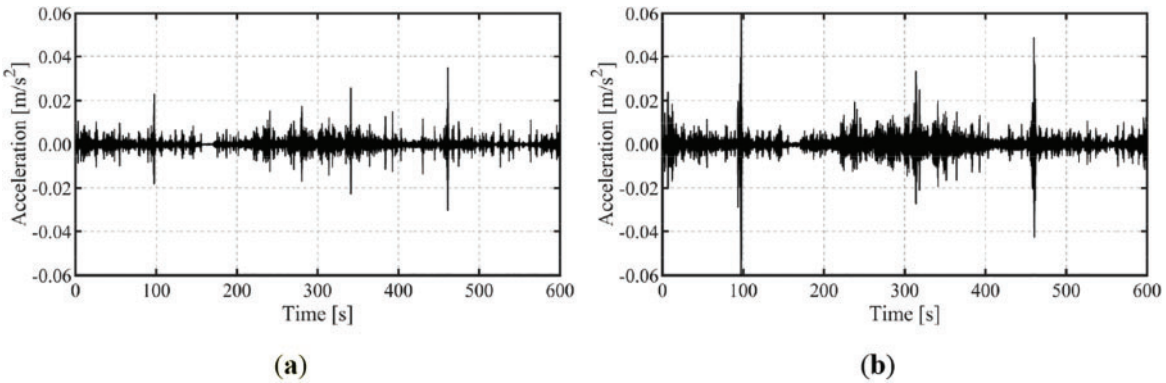

Figure 6. Typical acceleration time series recorded at the center of arch A3 (sensors A12 and A13) in October 2019: (a) lateral and (b) vertical responses

windows of 5400 s. Fig. 6 presents a sample of acceleration time series collected in October 2019, highlighting that the level of vertical vibration is about two times higher (both in terms of RMS and peak accelerations) than that observed in the lateral direction.

From a preliminary modal analysis, it emerged that the vibration modes of the investigated bridge are associated with the dominant vertical or lateral components of motion. Consequently, the modal analysis was performed twice, separating vertical and transverse accelerations. Furthermore, low-pass filtering and decimation were applied to downsample the data to 50 Hz.

In detail, the output-only modal identification was carried out by the frequency domain decomposition (FDD) technique[39] in the frequency domain and the covariance-driven stochastic subspace identification (SSI-Cov) method[40] in the time domain. Both methods have been implemented in MATLAB-based tools developed in previous research.[41]

The FDD technique consists of three main steps: (i) estimation of the spectral matrix **G**; (ii) singular value decomposition (SVD) of **G** at each frequency; (iii) peak-picking of the local maxima in the first singular value curve. The spectral matrix G (containing the auto- and cross-spectra of the responses) is estimated by applying Welch's method[42] to the measured signals. Then, the SVD of **G** is computed at each frequency:

$$\mathbf{G}(f) = \mathbf{U}(f)\boldsymbol{\sigma}(f)\mathbf{U}^{\mathrm{H}}(f) \tag{1}$$

where **U** is a complex matrix containing the singular vectors as columns, the superscript $^{\mathrm{H}}$ denotes a complex conjugate transpose matrix, and $\boldsymbol{\sigma}$ is the diagonal matrix collecting singular values in descending order. At each frequency, the first and largest singular value (σ_1) represents the intensity

of the vibration mode at that frequency. Therefore, the vibration modes can be identified as the local maxima of the first singular value curve: at each selected frequency peak is associated with a mode shape.

The SSI technique is based on the discrete state-space representation of the equations of motion of a linear, time-invariant system subjected to unknown excitation:

$$x_{k+1} = \mathbf{A}\, x_k + w_k \tag{2}$$

$$y_k = \mathbf{C}\, x_k + v_k \tag{3}$$

where $x_k \in \Re^N$ denotes the discrete-time state vector, which includes the displacements and velocities describing the condition of the system at the time instant $t_k = k\Delta t$; $y_k \in \Re^L$ is the output vector, containing the L measured responses; $w_k \in \Re^N$ and $v_k \in \Re^L$ represent the process and measurement noise, respectively. Matrix $\mathbf{A}$ is the discrete state matrix, whose values depend on the structural mass, stiffness, and damping properties, while $\mathbf{C}$ is the discrete output matrix, responsible for mapping the state vector into the measured response. Eq. (2) is commonly referred to as the state equation, whereas Eq. (3) is known as the observation, or output, equation.

In the SSI-Cov method, covariance matrices of the responses are computed at increasing time lags to identify the matrices $\mathbf{A}$ and $\mathbf{C}$ from the recorded signals. These covariance matrices are arranged into a Toeplitz matrix, and then SVD is performed. However, in practical applications, the model order is not known a priori. To address this issue, a common practice is to obtain possible modal parameters by increasing the model order and representing all results in a diagram, called a stabilization diagram. A physical mode is identified when consistent dynamic characteristics (in terms of frequency, damping ratio, and mode shape) are obtained from models of increasing order. Conversely, "modes" or poles characterized by a strong dispersion of modal parameters are called spurious and represent "nonphysical" modes. Cleaning the stabilization diagram, therefore, consists of eliminating spurious poles and identifying stable pole alignments associated with "physical" modes. In detail, the present application adopted the following sequence of cleaning steps: (1) modal damping threshold; (2) mode shape complexity threshold using the modal phase collinearity (MPC) coefficient;[43] and (3) hierarchical clustering. Once the stabilization diagram is cleaned, each cluster is associated with average values of frequency, damping, and mode shape, together with the corresponding standard deviations.

The selection of SSI parameters was guided by the careful interpretation of the stabilization diagrams and prior experience with masonry structures. The chosen time lag (60–70) provided sufficient information to capture the dominant modes while maintaining numerical stability; the model order range (20–120) captured all relevant structural modes while limiting spurious ones; and the damping/MPC thresholds (8–14% and 0.75–0.85) reflected values typically observed in civil structures.[44–46] These criteria, although tuned manually, follow established practice and make the procedure reproducible for future studies.

To compare the mode shapes identified from different methods and tests, the well-known modal assurance criterion (MAC)[47] was computed. The MAC correlation coefficient ranges from 0 to 1: a value greater than 0.85 indicates a good correlation, whereas a value lower than 0.50 is considered a poor match.

Dynamic Characteristics of the Bridge Over the Gesso River

Dynamic characteristics before strengthening (October 2019)

As previously pointed out, the first AVT was carried out in late October 2019, during daytime, with air temperature ranging between 16.5°C and 17.6°C. The application of FDD and SSI techniques led to the identification of 5 lateral and 3 vertical vibration modes in the frequency range of 0–18 Hz.

As shown in Fig. 7, the vibration modes are identified from the local maxima of the first SV line using the FDD method (Fig. 7a refers to lateral responses, whereas Fig. 7b relates to the vertical ones) and through the alignment of stable poles in the stabilization diagram obtained by applying the SSI method (Fig. 7c refers to lateral responses and Fig. 7d to vertical ones). As expected, the spectral analysis of vertical accelerations exhibits more evident peaks due to the higher excitation level. Nevertheless, both methods provided consistent indications of the same vibration modes in both lateral and vertical responses.

Fig. 8 shows the mode shapes identified using the FDD method. The fundamental vibration mode is in the transverse direction, and with a frequency of 5.3 Hz. The lateral modes exhibit an increasing number of half-sine waves and inflection points, with the only exception being mode L3*, which has the same mode shape as mode L3. The mode shapes V1 and V2 are associated with vertical bending, while V3 corresponds to a torsional mode.

Table 1 summarizes the results obtained by applying the FDD and the SSI identification methods through: (a) the natural frequencies identified by the FDD technique; (b) the natural frequencies and modal damping ratios identified by the SSI method. In addition, Table 1 compares the estimates of corresponding mode shapes obtained by the two techniques through the MAC. The limited differences in mode shapes are demonstrated by a MAC larger than 0.90 for all modes except for L3*, for which the MAC is equal to 0.84. In this last case, the FDD technique seems to provide a more accurate estimation of the mode shape.

The modal characteristics identified in the first test suggest the following comments:

- The damping estimates are generally relatively high, with modes L1, L2, and L4 having values higher than 7%.
- Modes L1 and L2 exhibit a local distortion of the mode shapes, localized at the third quarter of arch A1 (Borgo side) and–more evidently–at the first quarter of arch A3 (Cuneo side). As highlighted by visual

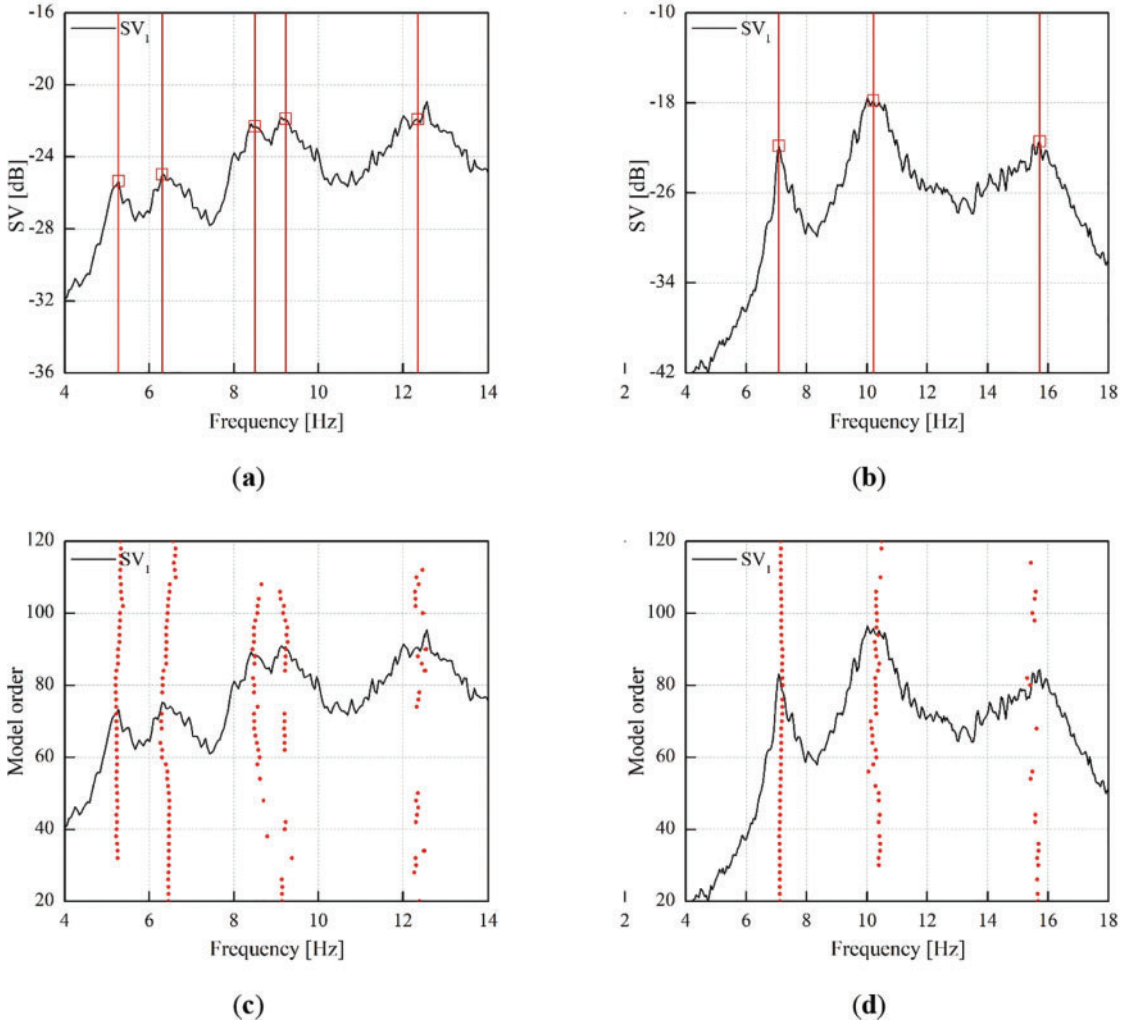

Figure 7. Identification of vibration modes from the AVT of October 2019: (a, b) first singular value (SV) curve and peak picking (FDD) of horizontal and vertical accelerations, respectively; (c, d) stabilization diagram (SSI-Cov) of horizontal and vertical accelerations, respectively

inspection, the arch barrels are affected in those regions by a severe state of degradation, providing a possible explanation for the identified irregularities.

- Mode L3* exhibits the same mode shape as mode L3 with a slight difference in natural frequency. This phenomenon should be classified as a "frequency splitting"[48] and, in this case, it is likely related to existing damage at the arch barrels, although this remains an assumption supported by indirect evidence. Particularly, the visual inspections highlighted the presence of discontinuities at the skewback between arch A3 and pier P2, where mode L3 exhibits the maximum modal displacement.

Dynamic characteristics after strengthening (March 2024)

The second AVT was performed at the beginning of March 2024, during daytime, with air temperature ranging between 12.8°C and 16.9°C. Applying the FDD and SSI techniques led to the identification of 7 vibration modes in the frequency range of 0–18 Hz: 4 lateral and 3 vertical modes.

The output-only identification was first performed with the FDD technique: Figs. 9a, 9b shows the first SV line obtained from the analysis of the lateral and vertical accelerations, respectively. As shown by the alignments of stable poles in Figs. 9c, 9d, the SSI-Cov algorithm was also applied to lateral and vertical responses, respectively. It should be noted that the presence of normal modes is clearly highlighted by both the local maxima of the SV lines (FDD) and the corresponding alignments of stable poles (SSI-Cov).

Fig. 10 illustrates the mode shapes identified by applying the FDD method. The fundamental vibration mode is characterized by a predominant transverse modal displacement with a natural frequency of 5.8 Hz. The subsequent lateral modes exhibit an increasing number of half-sine waves and inflection points, as expected. Furthermore, vibration modes V1 and V2 are associated with vertical bending, while mode V3 represents a vertical torsion mode.

Table 2 summarizes the natural frequencies identified by applying the FDD and SSI-Cov procedures, the damping

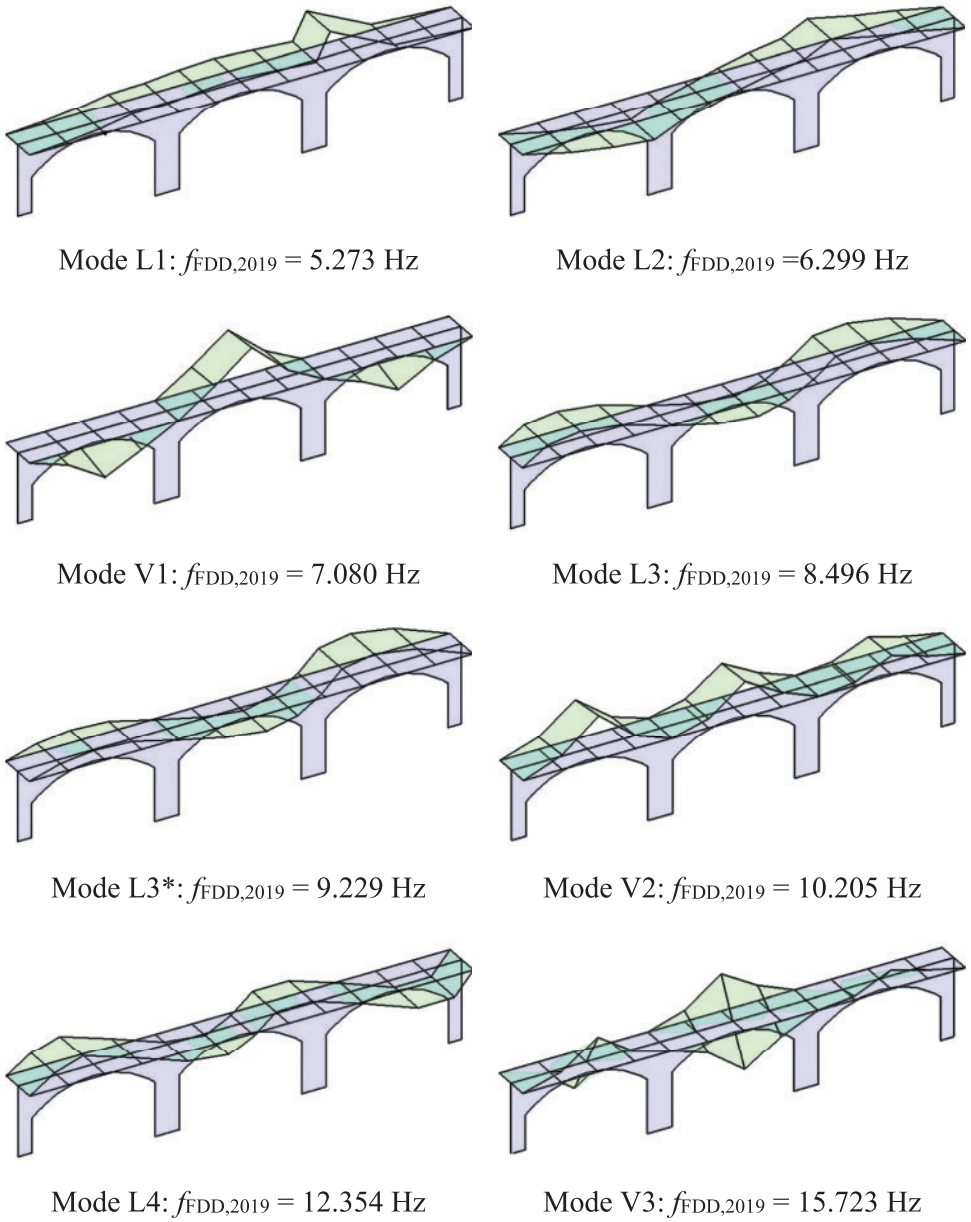

Figure 8. Vibration modes identified before the repair intervention in October 2019 (L = dominant lateral, V = dominant vertical)

Table 1. Summary of the modal parameters identified in 2019 by FDD and SSI

Mode ID	FDD	SSI		MAC
	f_{2019} (Hz)	f_{2019} (Hz)	ζ (%)	
L1	5.273	5.263	7.65	0.97
L2	6.299	6.435	7.47	0.96
V1	7.080	7.154	3.36	0.99
L3	8.496	8.541	2.98	0.94
L3*	9.229	9.204	4.97	0.84
V2	10.205	10.321	2.54	0.98
L4	12.354	12.371	7.84	0.96
V3	15.723	15.563	3.11	0.92

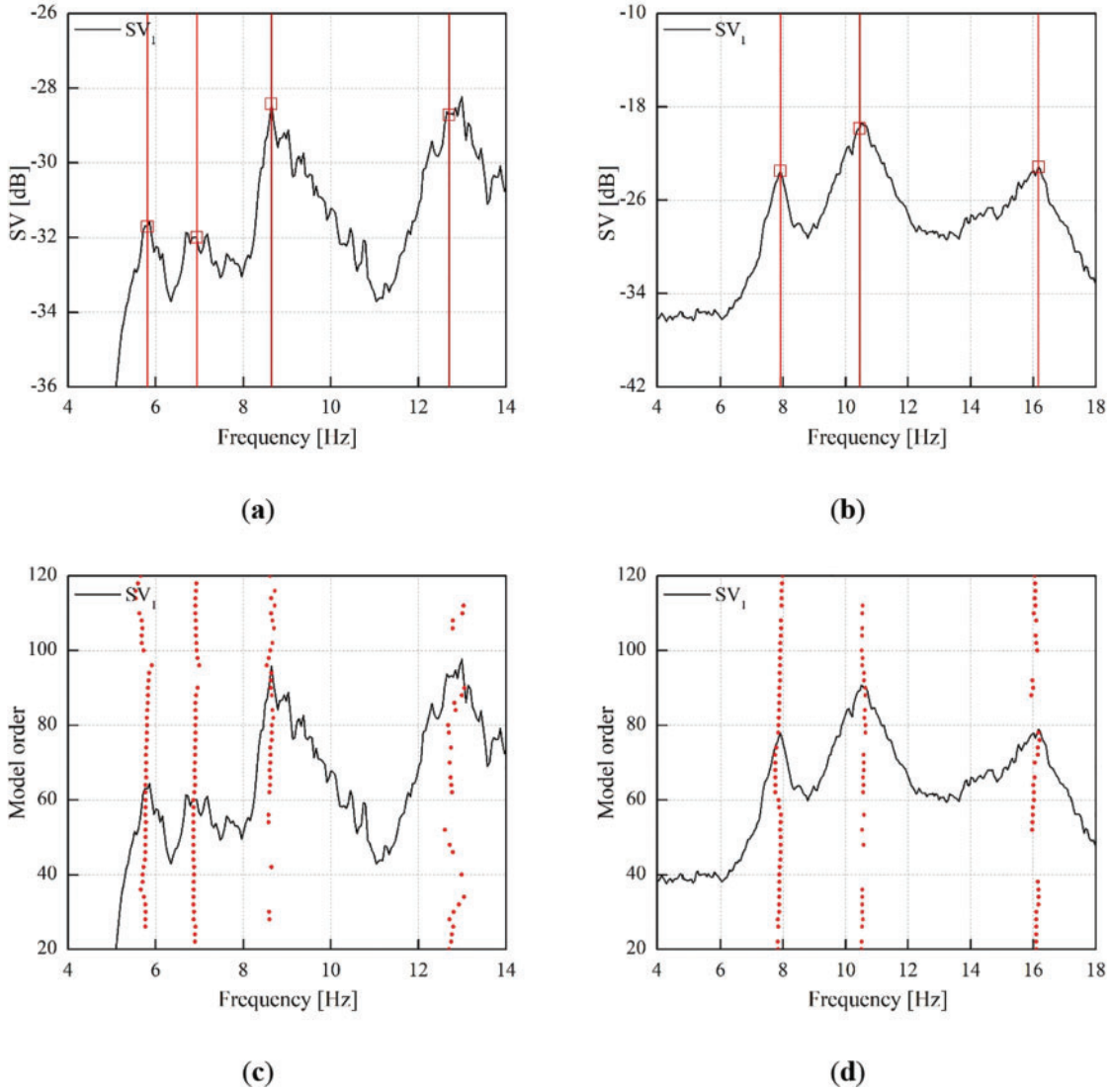

Figure 9. Identification of vibration modes from the AVT of March 2024: (a, b) first singular value curve and peak picking (FDD) of horizontal and vertical accelerations, respectively; (c, d) stabilization diagram (SSI-Cov) of horizontal and vertical accelerations, respectively

ratios (from SSI-Cov), and the MAC between the corresponding mode shapes. The differences in mode shapes are generally negligible, with MAC values greater than 0.98 for the first four modes and values ranging from 0.92 to 0.96 for the higher modes.

The modal characteristics identified in the second test suggest the following comments:

- The estimates of modal damping are particularly high for modes L1 and L2, with values greater than 9%, while for the other modes, the damping ranges from a minimum of 3% for mode V3 to a maximum of 5.6% for mode L4.
- The mode shapes are generally regular but not perfectly symmetrical with respect to the center of the structure. This is particularly visible in the mode shapes L2 and L4, in which the modal displacements at piers P1 and P2 are nonsymmetric.

Comparison between the Modal Properties before and after the Intervention

Performing dynamic investigations before and after the strengthening intervention allowed the evaluation of the intervention's effects in solving the detected structural issues. The AVT carried out after the consolidation works was indeed a substantial repetition of the 2019 investigation, employing the same measurement devices and the same measurement positions.

During the 2024 test, seven vibration modes were identified, while in the 2019 test, an additional vibration mode was present. As previously noted, the additional vibration mode L3* is probably related to the "frequency splitting" phenomenon generated by the presence of discontinuities at the skewback between arch A3 and pier P2. The absence of mode L3* in the 2024 results suggests the effectiveness

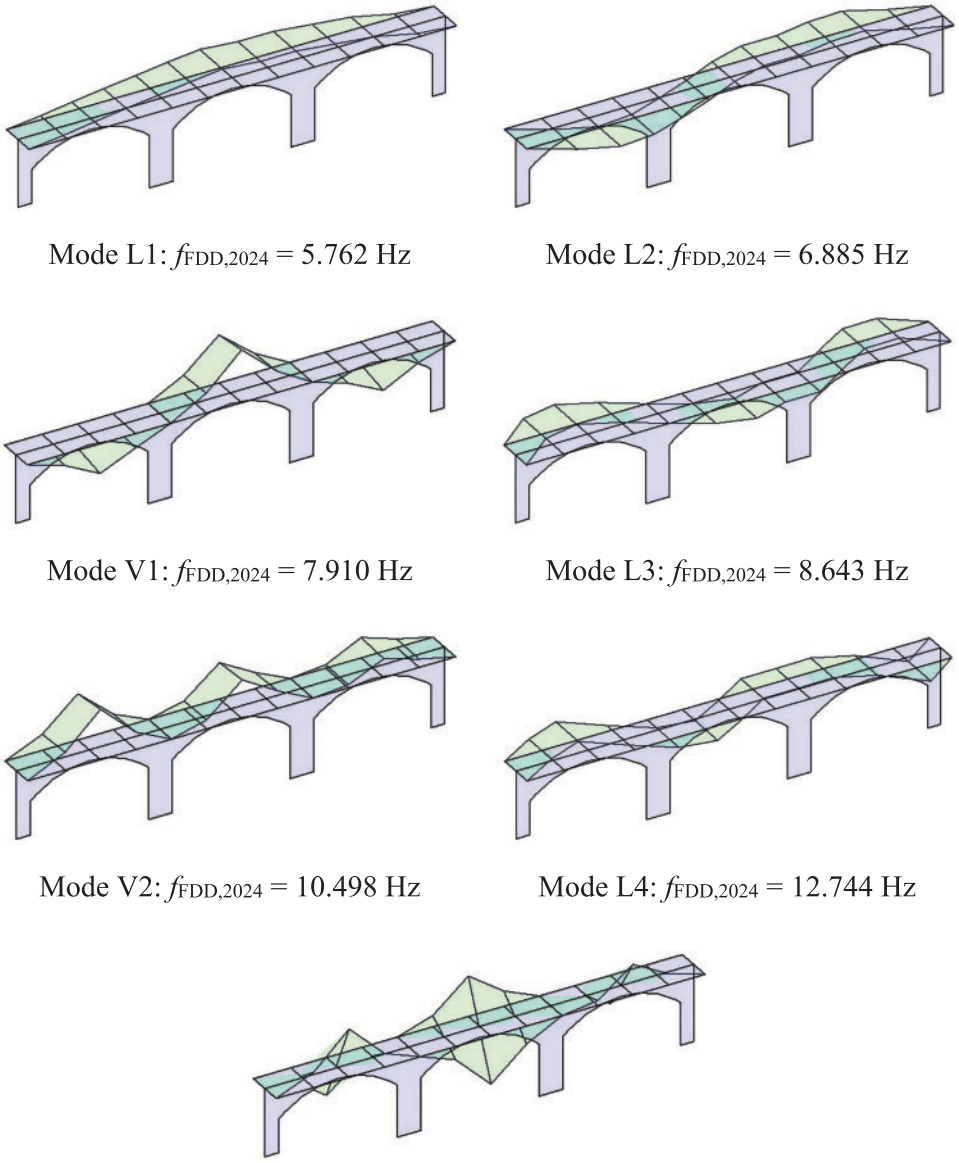

Figure 10. Vibration modes identified after the repair intervention in March 2024 (L = dominant lateral, V = dominant vertical)

Table 2. Summary of the modal parameters identified in 2024 by FDD and SSI

Mode ID	FDD	SSI		MAC
	f_{2024} (Hz)	f_{2024} (Hz)	ζ (%)	
L1	5.762	5.751	10.66	1.00
L2	6.885	6.898	9.62	0.99
V1	7.910	7.878	3.85	0.99
L3	8.643	8.632	4.71	0.98
V2	10.498	10.562	3.78	0.92
L4	12.744	12.814	5.64	0.92
V3	16.162	16.069	3.26	0.96

Table 3. Comparison between the natural frequencies identified in 2024 and 2019

Mode ID	$f_{FDD,2019}$ (Hz)	$f_{FDD,2024}$ (Hz)	Δf (%)
L1	5.273	5.762	+9.27
L2	6.299	6.885	+9.30
V1	7.080	7.910	+11.7
L3	8.496	8.643	+1.73
V2	10.205	10.498	+2.84
L4	12.354	12.744	+3.16
V3	15.723	16.162	+2.80

$\Delta f = [(f_{FDD,2024}/f_{FDD,2019}) - 1] \times 100$

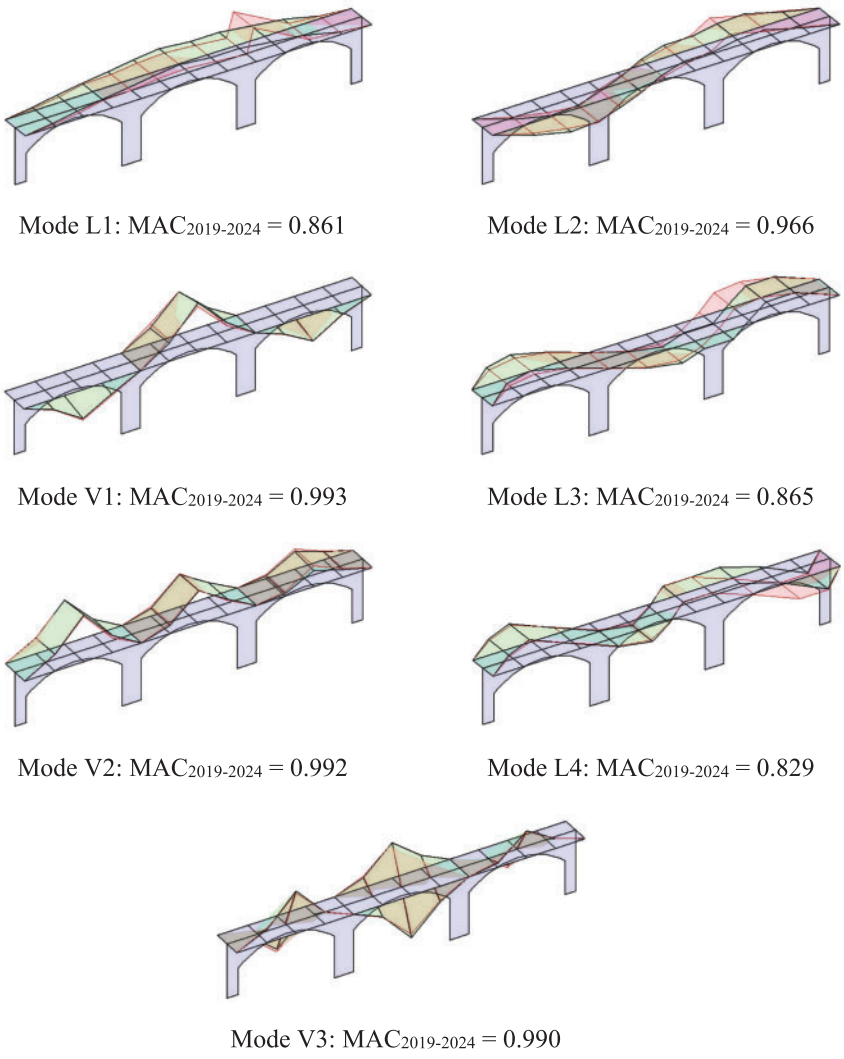

Figure 11. Comparison between the vibration modes identified in 2019 and 2024

of the intervention in repairing the existing damages and discontinuities.

Table 3 and Fig. 11 illustrate the comparison between the current dynamic characteristics (2024) and those identified in 2019 using the FDD method. In particular, Table 3 shows a substantial increase in natural frequencies, with an average percentage value across the seven modes of +5.4%, and a more pronounced increase in the first three modes (L1, L2, and V1), with an average percentage value of +9.2%.

The average temperatures recorded during the two surveys were 17.1°C and 15.0°C on October 28, 2019 and April 4, 2024, respectively. As known from previous monitoring experiences on masonry structures,[12,14] natural frequencies tend to increase with temperature increase. Consequently, the slight decrease in temperature between the 2019 and 2024

tests should have caused a slight reduction in natural frequencies rather than contributing to the identified increase. In other words, the observed frequency increase might be even higher once the temperature effects are compensated.

Regarding the other environmental and operational effects, both tests were conducted under moderate vehicular traffic conditions, with an average flow of light vehicles and occasional heavy trucks. The river level was close to the seasonal average, and weather conditions were stable. These conditions were comparable between the two surveys and, as expected, no effects on the identified dynamic behavior were observed.

Fig. 11 presents a comparison of the mode shapes with the associated MAC factor. The consistently high MAC correlation factors confirm that the nature of the modes identified in the two tests is the same, with values exceeding 0.8. However, the comparison reveals localized differences in the modal deformations before and after the intervention. In the 2019 test, irregularities were found in the modal deformations at measurement points A4 (third quarter of the lateral arch on the Borgo S. Giuseppe side) and, more prominently, A11 (first quarter of the lateral arch on the Cuneo Altopiano side). In the 2024 investigations, the previously observed distortions appear to have been effectively resolved, suggesting a clear improvement in the bridge's condition.

Conclusions

The paper focuses on the operational modal analysis of a historical masonry arch bridge (1856) to evaluate the effectiveness of a strengthening intervention. Two dynamic tests under operational conditions were carried out before and after the repair work (in October 2019 and April 2024, respectively). The dynamic characteristics of the structure were evaluated using the FDD and SSI-Cov output-only identification techniques.

The visual inspections carried out in 2019 revealed the general state of degradation of the brick masonry and the presence of a severe discontinuity at the skewback between arch A3 and pier P2. The OMA highlighted irregularities in the mode shapes, which were more evident around the structural discontinuity. In addition, the presence of two vibration modes characterized by a slight difference in natural frequencies but the same mode shape (i.e., L3 and L3*) suggests the presence of a "frequency splitting" phenomenon caused—again—by the discontinuity at pier P2–arch A3.

Following the strengthening intervention, the 2024 test indicated a clear change in the bridge's dynamic response. The disappearance of mode L3* and the remarkable increase in natural frequencies, particularly in the first three modes, demonstrated the success of the repairs in addressing the previously identified damages. In addition, the comparison of mode shapes before and after the intervention, supported by a consistently high MAC correlation factor, further confirmed the structural improvements, with the irregularities in modal displacements being effectively amended.

Overall, the results presented show that operational modal testing and analysis are effective tools for evaluating the dynamic behavior of masonry bridges. These methods provide valuable insights for assessing structural deficiencies and evaluating the effectiveness of strengthening interventions. Future developments of this research will focus on collecting additional information on the bridge geometry, material properties, and details of the strengthening works. These data will enable the development of a calibrated numerical model, which will be used to support a quantitative assessment of the damage and to complement the experimental results presented in this study.

Acknowledgments

Sincere thanks are due to M. Cucchi, M. Iscandri (LPMSC, Politecnico di Milano), and PhD A. Ruccolo (DABC, Politecnico di Milano), for their assistance in conducting the field tests.

Author Contributions

Conceptualization, P.B. and C.G.; investigation, P.B. and C.G.; data curation, P.B. and C.G.; writing—original draft preparation, P.B.; writing—review and editing, P.B. and C.G.; visualization, P.B.; supervision, C.G.; funding acquisition, C.G. All authors have read and agreed to the published version of the manuscript.

Data Availability Statement

The experimental datasets collected and analyzed during the current study are available from the corresponding author upon reasonable request. Additionally, data requests will require approval from the bridge manager (Province of Cuneo).

Conflicts of Interest

The authors declare no conflicts of interest.

References

[1] D'Angelo M, Civera M, Giordano PF, et al. Bridge collapses in Italy across the 21st century: survey and statistical analysis. *Struct Infrastruct Eng*. 2025. doi:10.1080/15732479.2025.2483500.

[2] Magalhães F, Cunha A. Explaining operational modal analysis with data from an arch bridge. *Mech Syst Signal Process*. 2011;25(5):1431–1450. doi:10.1016/j.ymssp.2010.08.001.

[3] Rainieri C, Notarangelo MA, Fabbrocino G. Experiences of dynamic identification and monitoring of bridges in serviceability conditions and after hazardous events. *Infrastructures (Basel)*. 2020;5(10):1–23. doi:10.3390/infrastructures5100086.

[4] Benedettini F, Dilena M, Morassi A. Vibration analysis and structural identification of a curved multi-span

viaduct. *Mech Syst Signal Process*. 2015;54(12):84–107. doi:10.1016/j.ymssp.2014.08.008.

[5] Clemente P, Bongiovanni G, Buffarini G, Saitta F. Structural health status assessment of a cable-stayed bridge by means of experimental vibration analysis. *J Civ Struct Health Monit*. 2019;9(5):655–669. doi:10.1007/s13349-019-00359-2.

[6] Cunha Á, Caetano E, Magalhães F, Moutinho C. Dynamic identification and continuous dynamic monitoring of bridges: different applications along bridges life cycle. *Struct Infrastruct Eng*. 2018;14(4):445–467. doi:10.1080/15732479.2017.1406959.

[7] D'angelo M, Menghini A, Borlenghi P, et al. Hydraulic safety evaluation and dynamic investigations of Baghetto Bridge in Italy. *Infrastructures (Basel)*. 2022;7(4):53. doi:10.3390/infrastructures7040053.

[8] Gentile C, Saisi A. Ambient vibration testing and condition assessment of the Paderno iron arch bridge. *1889 Constr Build Mater*. 2011;25(9):3709–3720. doi:10.1016/j.conbuildmat.2011.04.019.

[9] Bayat E, Milone A, Tubino F, Venuti F. Vibration serviceability assessment of a historic suspension footbridge. *Buildings*. 2022;12(6):732. doi:10.3390/buildings12060732.

[10] Caetano E, Cunha Á, Magalhães F, Moutinho C. Studies for controlling human-induced vibration of the Pedro e Inês footbridge, Portugal. Part 1: assessment of dynamic behaviour. *Eng Struct*. 2010;32(4):1069–1081. doi:10.1016/j.engstruct.2009.12.034.

[11] Nicoletti V, Quarchioni S, Tentella L, Martini R, Gara F. Experimental tests and numerical analyses for the dynamic characterization of a steel and wooden cable-stayed footbridge. *Infrastructures (Basel)*. 2023b;8(6):100. doi:10.3390/infrastructures8060100.

[12] Gentile C, Guidobaldi M, Saisi A. One-year dynamic monitoring of a historic tower: damage detection under changing environment. *Meccanica*. 2016;51(11):2873–2889. doi:10.1007/s11012-016-0482-3.

[13] Magalhães F, Cunha A, Caetano E. Online automatic identification of the modal parameters of a long span arch bridge. *Mech Syst Signal Process*. 2009;23(2):316–329. doi:10.1016/j.ymssp.2008.05.003.

[14] Ubertini F, Cavalagli N, Kita A, Comanducci G. Assessment of a monumental masonry bell-tower after 2016 central Italy seismic sequence by long-term SHM. *Bullet Earthq Eng*. 2018;16(2):775–801. doi:10.1007/s10518-017-0222-7.

[15] Catbas FN, Cano JA, Luleci F, Walters LC, Michlowitz R. On the generation of digital data and models from point clouds: application to a pedestrian bridge structure. *Infrastructures (Basel)*. 2024;9(1):6. doi:10.3390/infrastructures9010006.

[16] Funari MF, Hajjat AE, Masciotta MG, Oliveira DV, Lourenço PB. A parametric scan-to-FEM framework for the digital twin generation of historic masonry structures. *Sustainability (Switzerland)*. 2021;13(19):11088. doi:10.3390/su131911088.

[17] Nicoletti V, Martini R, Carbonari S, Gara F. Operational modal analysis as a support for the development of digital twin models of bridges. *Infrastructures (Basel)*. 2023a;8(2):24. doi:10.3390/infrastructures8020024.

[18] Brownjohn JMW, Moyo P, Omenzetter P, Lu Y. Assessment of highway bridge upgrading by dynamic testing and finite-element model updating. *J Bridge Eng*. 2003;8:3–162. doi:10.1061/(asce)1084-0702(2003)8:3(162).

[19] Castelli S, Labò S, Belleri A, Moaveni B. Operational modal analysis, seismic vulnerability assessment and retrofit of a degraded RC bell tower. *J Civ Struct Health Monit*. 2024;14(4):885–907. doi:10.1007/s13349-024-00765-1.

[20] Pierdicca A, Clementi F, Fortunati A, Lenci S. Tracking modal parameters evolution of a school building during retrofitting works. *Bullet Earthquake Eng*. 2019;17(2):1029–1052. doi:10.1007/s10518-018-0483-9.

[21] Ribeiro D, Costa B, Cruz L, et al. Simulation of the dynamic behavior of a centenary metallic bridge under metro traffic actions based on advanced interaction models. *Int J Struct Stab Dynam*. 2021;21(04):2150057. doi:10.1142/S0219455421500577.

[22] Zaki MA, Abu-Hamd MH. Rehabilitation assessment of a steel railway bridge by dynamic field testing. *Struct Infrastruct Eng*. 2007;3(4):343–353. doi:10.1080/15732470600578767.

[23] Zanardo G, Hao H, Xia Y, Deeks AJ. Stiffness assessment through modal analysis of an RC slab bridge before and after strengthening. *J Bridge Eng*. 2006;11:590–601. doi:10.1061/(ASCE)1084-0702(2006)11:5(590).

[24] Cury A, Cremona C, Dumoulin J. Long-term monitoring of a PSC box girder bridge: operational modal analysis, data normalization and structural modification assessment. *Mech Syst Signal Process*. 2012;33:13–37. doi:10.1016/j.ymssp.2012.07.005.

[25] Maalek S, Akbari R, Ziaei-Rad S. The effects of the repair operations and replacement of the elastomeric bearings on the modal characteristics of a highway bridge. *Struct Infrastruct Eng*. 2010;6(6):753–765. doi:10.1080/15732470802334829.

[26] Costa BJA, Magalhães F, Cunha T, Figueiras J. Rehabilitation assessment of a centenary steel bridge based on modal analysis. *Eng Struct*. 2013;56(4):260–272. doi:10.1016/j.engstruct.2013.05.010.

[27] Costa BJA, Magalhães F, Cunha Á, Figueiras J. Modal analysis for the rehabilitation assessment of the Luiz I Bridge. *J Bridge Eng*. 2014;19(12):14. doi:10.1061/(ASCE)BE.1943-5592.0000632.

[28] Ramos LF, Marques L, Lourenço PB, De Roeck G, Campos-Costa A, Roque J. Monitoring historical masonry structures with operational modal analysis: two case studies. *Mech Syst Signal Process*. 2010;24(5):1291–1305. doi:10.1016/j.ymssp.2010.01.011.

[29] Ercan E. Assessing the impact of retrofitting on structural safety in historical buildings via ambient vibration tests. *Constr Build Mater*. 2018;164(1):337–349. doi:10.1016/j.conbuildmat.2017.12.154.

[30] Namlı M, Aras F. Performance evaluation of a seismic strengthening applied on a masonry school building by dynamic analyses. *Structures*. 2024;62(2):106200. doi:10.1016/j.istruc.2024.106200.

[31] Masciotta M-G, Ramos LF, Lourenço PB, Vasta M. Damage identification and seismic vulnerability assessment of a historic masonry chimney. *Ann Geophy*. 2017;60(4):S0442. doi:10.4401/ag-7126.

[32] Borlenghi P, Saisi A, Gentile C. ND testing and establishing models of a multi-span masonry arch bridge. *J Civ Struct Health Monit*. 2023;13(8):1595–1611. doi:10.1007/s13349-022-00666-1.

[33] Brencich A, Sabia D. Experimental identification of a multi-span masonry bridge: the Tanaro Bridge. *Constr Build Mater*. 2008;22(10):2087–2099. doi:10.1016/j.conbuildmat.2007.07.031.

[34] Civera M, Mugnaini V, Zanotti Fragonara L. Machine learning-based automatic operational modal analysis: a structural health monitoring application to masonry arch

bridges. *Struct Control Health Monit*. 2022;29(10):499. doi:10.1002/stc.3028.
[35] Costa C, Ribeiro D, Jorge P, Silva R, Arêde A, Calçada R. Calibration of the numerical model of a stone masonry railway bridge based on experimentally identified modal parameters. *Eng Struct*. 2016;123(2):354–371. doi:10.1016/j.engstruct.2016.05.044.
[36] Mansour S, Rizzo F, Giannoccaro NI, La Scala A, Sabbà MF, Foti D. Essential dynamic characterization of a historical bridge: integrated experimental and numerical investigations. *J Civ Struct Health Monit*. 2024;14(1):85–102. doi:10.1007/s13349-023-00744-y.
[37] Pantò B, Ortega J, Grosman S, et al. Advanced calibration of a 3D masonry arch bridge model using non-destructive testing and numerical optimisation. *Constr Build Mater*. 2024;438(5):137131. doi:10.1016/j.conbuildmat.2024.137131.
[38] Zini G, Betti M, Bartoli G, Morano SG, Spinelli P. Structural health monitoring of a masonry arch bridge: modal identification and model updating. *Int J Maso Res Innovat*. 2023;9(1/2):42–53. doi:10.1504/IJMRI.2024.135244.
[39] Brincker R, Zhang L, Andersen P. Modal identification of output-only systems using frequency domain decomposition. *Smart Mater Struct*. 2001;10(3):441–445. doi:10.1088/0964-1726/10/3/303.
[40] Peeters B, De Roeck G. Reference-based stochastic subspace identification for output-only modal analysis. *Mech Syst Signal Process*. 1999;13(6):855–878. doi:10.1006/mssp.1999.1249.
[41] Gentile C, Pirrò M, Borlenghi P. DYMOND: a matlab toolbox for the dynamic monitoring of bridges according to the Lombardia regional guidelines. *Lect Not Civil Eng*. 2024;514 LNCE:476–487. doi:10.1007/978-3-031-61421-7_47.
[42] Welch PD. The use of fast fourier transform for the estimation of power spectra: a method based on time averaging over short, modified periodograms. *IEEE Transact Aud Electroacou*. 1967;15(2):70–73. doi:10.1109/TAU.1967.1161901.
[43] Pappa RS, Elliott KB, Schenk A. Consistent-mode indicator for the eigensystem realization algorithm. *J Guid Cont Dynam*. 1993;16(5):852–858. doi:10.2514/3.21092.
[44] Anastasopoulos D, Reynders EPB. Modal strain monitoring of the old Nieuwebrugstraat Bridge: local damage versus temperature effects. *Eng Struct*. 2023;296(3–4):116854. doi:10.1016/j.engstruct.2023.116854.
[45] Cabboi A, Gentile C, Saisi A. From continuous vibration monitoring to FEM-based damage assessment: application on a stone-masonry tower. *Constr Build Mater*. 2017;156(5):252–265. doi:10.1016/j.conbuildmat.2017.08.160.
[46] Hernández-González IA, García-Macías E, Costante G, Ubertini F. AI-driven blind source separation for fast operational modal analysis of structures. *Mech Syst Signal Process*. 2024;211(5):111267. doi:10.1016/j.ymssp.2024.111267.
[47] Allemang RJ, Brown DL. Correlation coefficient for modal vector analysis. *Proceedings of the International Modal Analysis Conference & Exhibit*; 1982
[48] Zonta D, Modena C. Observations on the appearance of dispersive phenomena in damaged structures. *J Sound Vib*. 2001;241(5):925–933. doi:10.1006/jsvi.2000.3320.

BER the international journal of bridge engineering management and research

History of Bridges: Materials and Structural Types of a Monument to Progress

Paolo Clemente*

Submitted: 03 August 2025 **Accepted:** 01 October 2025 **Publication date:** 10 October 2025

DOI: 10.70465/ber.v2i4.48

Abstract: The history of bridges is retraced as a witness to humanity's progress. The evolution of materials and structural typologies has enabled ever-longer spans to be achieved at sustainable costs. The availability of materials such as reinforced concrete and steel has offered new possibilities, unthinkable when using wood and masonry. Then girder bridges were built, followed later by cable-stayed and suspension bridges, as well as long-span arch bridges. The race for long spans continues. Bridges have always been, and always will be, monuments to progress.

Author keywords: History of Bridges; Materials; Structural typologies; Beam bridges; Arch bridges; Cable-stayed bridges; Suspension bridges

Introduction

The disasters that have affected bridges and viaducts all over the world in recent years have brought concerns about the safety of such structures not only to the attention of technicians and authorities but also among the general public. These events have sparked curiosity among them about how these structures work and how they evolved over time.[1] These disasters have led to a greater focus on the protection and maintenance of existing bridges. However, this is not possible without a deep understanding of their static and dynamic behavior and, therefore, a reliable knowledge of bridge design and construction.[2–4] Over time, various structural typologies have been developed and used, depending on the available materials and technologies, as well as on theoretical and practical knowledge derived from previous experiences.[5]

The evolution of bridges has followed the history of humanity, and the history of humanity itself could be studied and told through the evolution of bridges over time. Since the Neolithic age, the construction of a bridge has always been motivated by the need to overcome, with a vehicular or pedestrian path, an obstacle due to the geomorphology of the land, such as a river or a valley, to facilitate travel, contact, exchange, and trade with other peoples. The Romans, therefore, were great bridge builders, requiring fast and safe connections for the maintenance and control of their vast empire. With the fall of the Roman Empire and until the 9th century AD, interest in bridges decreased considerably because the political units extended over small territories and, consequently, could not afford the costs of construction and maintenance of these challenging structures.

Building a bridge has always been a challenge against the forces of nature, accompanied by the fear of failure: "Every span is something that can't be done until the men in steel helmets have driven in their last rivet," said Joseph Strauss, designer of the Golden Gate Bridge.[6] These difficulties have always fascinated people. The availability of new materials and the use of new technologies have revolutionized the way of building and conceiving bridges, but the admiration for ancient bridges that have survived to the present day is no less than that for modern long-span bridges.

In this paper, the materials and typologies used to overcome ever-longer spans at sustainable costs over time are reviewed. The availability of new materials, such as steel and reinforced concrete, has offered new possibilities in recent centuries, unthinkable with wood or masonry, such as the use of simple structural typologies like girder bridges, or those characterized by elements subject to traction, such as cable-stayed and suspension bridges.[7,8] The language and treatment are deliberately simple, to facilitate reading and understanding, with the goal of encouraging young researchers, as well as even non-bridge engineers, to deepen their knowledge of these magnificent civil engineering works.

Materials used for Bridges

Organic materials

Early bridges were made of natural fibers and were similar to the modern suspension bridges. The earliest evidence comes from a rope bridge on the Indus River near Swat, dating from 400 BC, although suspension bridges were probably

*Corresponding Author: Paolo Clemente.
Email: paolo.clemente59@gmail.com
Research Director, Formerly ENEA Casaccia Research Centre, 00123 Rome, Italy

Discussion period open till six months from the publication date. Please submit separate discussion for each individual paper. This paper is a part of the Vol. 2 of the International Journal of Bridge Engineering, Management and Research (BER), ISSN 3065-0569.

in use much earlier in Southeast Asia, South America, and Equatorial Africa. In India, one or two main bamboo cables were usually laid between trees used as pylons, from which a walkway of cross-reeds was suspended by means of handrail cables. Similar bridges, sometimes made of wicker ropes and twisted vines, still exist in the Himalayas and elsewhere in Southeast Asia. The Incas in South America built suspension bridges with aloe or woven wicker cables and natural rock pylons. Anchorages were made by attaching the cables to heavy, crossed wooden beams held in place by rocks. Maintenance was entrusted to nearby villages, which were responsible for repairing and replacing the cables every few years. In Equatorial Africa, various types of climbing plants were used to build bridges.

Later, wood was used. The primitive girder bridges were made of tree trunks placed between the two banks of a river. Wood was well suited to the construction of the girders, thanks to its ability to resist both tensile and compressive stresses in the direction parallel to the fibers. Its lightness made it particularly suitable for long spans. However, wood was very vulnerable to humidity and fire and had high deformability. Furthermore, constructing joints in wooden bridges was difficult. Because of these drawbacks, ancient wooden bridges have not withstood the passing of the centuries, and we only have indirect evidence of them.

The Pons Sublicius, the oldest bridge in Rome and famous after the legend of Horatius Cocles, was made of wood. Bridges built during a war were generally made of wood: in *De Bello Gallico* (Chapter 17, Book IV) there is a detailed description of the construction of a bridge over the Rhine River. A bas relief on Trajan's Column reproduces the famous bridge over the Danube River, built by Apollodorus in Romania in 103–105, at the time of the expedition of Emperor Trajan against the Dacians (Fig. 1). It was composed of 20 masonry piers, on which wooden arches with a span of 55 m rested. It was demolished after the death of Trajan, leaving only the piers as a testimony to human genius.

Figure 1. Bas relief on the Trajan's Column, which reproduces the famous Apollodorus' Bridge over the Danube

After a period in which bridges were mostly destroyed rather than built, following the fall of the Roman Empire, wood was rarely adopted for permanent bridges. Nevertheless, there were notable examples such as the bridge over the Grand Canal in Venice, where the Rialto Bridge now stands, and the bridge over the Brenta near Bassano, Italy, designed by Andrea Palladio in the 16th century. Palladio proposed several schemes for wooden bridges with longer spans, including an arch bridge with a span of 36 m. However, true masterpieces in the field of wooden bridges were built in Switzerland:[9]

- The Zurich Bridge, with a span of 40 m, and the Schaffhausen Bridge over the Rhine, with two spans of about 60 m, were both built by Johann Ulrich Grubenmann in 1770.
- The Wettingen Bridge, completed in 1788, has a span of 118 m.

Wood was used for bridges in America in the 19th and 20th centuries, while in Europe today wooden bridges are built mainly in the Nordic countries but also elsewhere, especially for walkways and in mountainous areas. An interesting example is the Traversina Footbridge, completed in 1996 in the Swiss Alps, with a span of 47 m, whose elements were transported to the site by helicopter. Particular care was taken in protecting the structural elements and in studying the oscillations induced by the wind.

The masonry arch

The arch is certainly the most notable invention of classical art in the field of tension and a notable development in bridge construction. The arch allowed the use of no-tension-resistant materials, such as masonry, for bridges. The masonry arch was the most widely used structural type in bridges until the mid-20th century.[10]

The arch was already known in the ancient civilizations of Egypt, Babylon, Persia, and Magna Graecia. The Romans created notable examples of bridges (Fig. 2) and aqueducts (Fig. 3) that have survived to this day, even outside Rome. They had great merit not only in having used the arch extensively but also in having used natural cement with pozzolana. The construction of bridges over the Tiber River (Fig. 4) was presided over by the *Collegium Pontificum*, headed by the Pontifex Maximus. The title of Pontifex, literally meaning "bridge builder," has been interpreted etymologically with reference to these great works of civil engineering. It later passed later to the Roman emperors and is still in use to designate the Pope.

It may seem strange, but the arch was used for many centuries without its static behavior being fully understood. Leonardo da Vinci proposed practical rules for the design of an arch, and some of his drawings demonstrate how he posed the problem of determining the thrust, that is, the horizontal action transmitted by the arch to the foundations at the springing. In the first treatise on bridges, written by Henri Gautier in 1714, relationships between the dimensions of the various parts were suggested, and attention was paid to the thrust, but no rules were given on how to evaluate it. Later, in 1730, Claude Antoine Couplet proposed the first theories on the determination of the pressure line and, therefore, of the thrust. Other eminent scholars, such as Charles Coulomb in 1773, Gabriel Lamé, and Émile Clapeyron in

Figure 2. The Roman Leproso Bridge, Benevento

Figure 3. The Pont du Gard, Nimes

Figure 4. The Pons Aelius, known as Ponte Sant'Angelo, Rome

1823, also studied the subject. Finally, the mystery of the thrust and how to proportion the abutments was discovered. Carlo Alberto Castigliano carried out detailed studies on the statics of arches in 1879. His analysis of the Ponte Mosca in Turin is notable.

The construction of an arch is done by laying voussoirs, either dry or with mortar, and requires a centering, that is, a temporary support, until the keystone is placed. This operation represents the closing of the arch, hence the name of the stone itself. The height of the keystone center relative to the springers divided by the span is the sag ratio of the arch. The secret of a masonry arch lies in its shape rather than in the quality of the materials.[11] The shape must guarantee that at least one possible thrust line of the acting loads can be found that lies within the arch profile, with a certain safety margin that depends on the material strength.[12,13]

Usually, Roman arches had a semicircular shape, not suitable for overcoming long spans. Lowered arches, that is, with a low sag ratio, appeared in Europe around the 14th century, after the journey of Marco Polo to China, where they had already been used. Notable examples of low sag ratio arches built in Europe are:

- The Ponte Vecchio in Florence, completed in 1325. It consists of three arches with a span of 28.7 m and a rise of 4.2 m. It is also one of the most famous inhabited bridges in the world (Fig. 5).
- The Rialto Bridge, which crosses the Grand Canal in Venice. It was opened in 1591 and has a span of 27 m.
- The Pont de la Concorde in Paris, completed in 1791 with spans of 31.2 m and a sag ratio of 1/8. It was designed by Jean-Rodolphe Perronet, founder of the École Royale des Ponts et Chaussées (Fig. 6).
- The Ponte Mosca (named after the architect who designed and built it), was the first stone bridge built in Turin over the Dora Riparia. It was completed in 1827, has a span of 55 m and a height of only 5.5 m with a width of 13.70 m.

A particularly remarkable bridge was the Stari Mostar on the Neretva River, designed by the Turkish architect Mimar Hajrudin on behalf of Sultan Suleiman the Magnificent and completed in 1566 (Fig. 7).[14] It looks like a part of the building on both banks and was probably the longest single-arch bridge at the time of its construction. The original bridge was destroyed on November 9, 1993, during the war in Bosnia and Herzegovina. At the end of hostilities, it was rebuilt as it was before the conflict, recovering original blocks from the waters of the river and shaping the new blocks from the same mine in the village of Ortijes, so that each faithfully reproduced the corresponding lost original one. The new bridge was completed on July 22, 2004.

Figure 5. The Ponte Vecchio, Florence

The masonry arch, now considered an obsolete structural type in most countries, is still used in some countries. In China, there are several stone arch bridges with spans exceeding 100 m that were built in the last century and

Figure 6. The Pont de la Concorde, Paris

Figure 7. The Stari Mostar

are characterized by a low sag-to-span ratio. Among these extraordinary realizations are:[15]

- The Changhung Bridge on the Nanpan River in Yunnan Province, with a span of 112.5 m and a clear width of 8.5 m, completed in 1961 (Fig. 8).
- The Chiuhsikou Bridge in Fengtu, Szechuan, with a span of 116 m, completed in 1972 (Fig. 9).
- The Dan River Bridge on the Xindan River along the Jin-Jiao highway, 10 km from Jicheng in Shanxi, completed in 2000. With its 146 m span and 82 m height, it is the longest masonry arch bridge in the world (Fig. 10).

In this regard, it should be remembered that Leonardo da Vinci proposed an arch bridge to cross the Golden Horn in Istanbul for Sultan Bayazid II, with a clear span of 240 m, a rise of 57 m, and a thickness varying from 42 m at the springing to 9 m at the crown. The bridge was not constructed due to the insurmountable difficulties in its execution, but its static efficiency has been demonstrated in recent times.

Rudimentary stone girder bridges were also built using large blocks. The oldest was a bridge over the Meles River at Smyrna, now Izmir, Turkey, probably built in 850 BC. Another example is over the East Dart River at Postbridge on Dartmoor in Devon, which is thought to date back to the 12th century and consists of huge granite slabs resting on granite piers. Finally, the Anping Bridge at Chuanchow, an important Chinese seaport during the Sung dynasty, is particularly impressive. It was completed in 1152 and consists

Figure 8. The Changhung Bridge on the Nanpan River, China

Figure 9. The Chiuhsikou Bridge in Fengtu, China

Figure 10. The Dan River Bridge on the Xindan River, China

of 331 stone piers, on which girders made of several stone blocks rest, for a total length of over 2000 m.

Metallic materials

In 1779, Abraham Darby III built the first cast iron bridge over the Severn River at Coalbrookdale, England (Fig. 11). In 1795, the bridge survived an overflow of the same river that destroyed many bridges. This occurrence demonstrated the better resistance of metal bridges, encouraging their use and development. The Iron Bridge is now considered a World Heritage Site by UNESCO.

However, cast iron was fragile and had poor tensile strength. Therefore, it was not used for a very long time and was soon replaced by steel. It should be noted that the construction technique was still strongly influenced by knowledge of wooden constructions in early metal bridges: dovetail joints and mortise and tenon joints were still used in internal joints.

With the use of steel, increasingly larger spans were realized, thanks also to the evolution of structural systems, from the simply supported beam to the continuous beam, from the solid wall beam to the truss, to the thrust systems with inclined or arched piers up to the suspension bridge. Among

Figure 11. The Iron Bridge over the Severn River at Coalbrookdale, England

Figure 12. The Garabit Viaduct on the Truyère River, France

the designers who have made the history of bridges, it must be remembered:

- Robert Stephenson designed the Britannia Bridge on the Menai Strait in North Wales in 1850. It is a continuous girder bridge with four spans: 72 m side spans and 142 m central spans. This bridge masterfully reflected the modern concept of steel girder bridges.
- Gustave Eiffel designed the Garabit Viaduct on the Truyère River in the Massif Central, France, in 1884. This bridge is approximately 560 m in total length, including an arch bridge with a span of 165 m and a height of 120 m with respect to the river (Fig. 12).

Other examples of bridges from the same period are:

- The Luiz I Bridge over the Douro River in Porto, with a span of 172.5 m, completed in 1885. The bridge had upper and lower lanes.
- The Paderno Bridge on the Adda River, with a parabolic arch with a span of 150 m. The bridge, completed in 1889, was surmounted by a double carriageway truss with a road on the upper deck and a railway on the lower deck.

The reinforced concrete

In 1867, the French gardener Joseph Monier obtained a patent for the construction of vases and containers in concrete with steel reinforcement. This was the beginning of reinforced concrete, which was then widely used in the 20th century. In this new material, there is a perfect collaboration between the concrete, which has a good compression strength and the task of giving rigidity to the structural elements, and steel, which has a good tensile strength. The reinforced concrete changed radically the world of construction, allowing any shape to be created and was also very competitive from an economic point of view.

In the construction of bridges, reinforced concrete was initially used with the previous shapes, typical of masonry, not fully exploiting its potential. Afterward, new shapes and anatomies of structures were used. Reinforced concrete does not have the potential of steel spanning long distances but has the advantages of having greater durability and being able to be shaped.

François Hennebique, the first great designer of reinforced concrete bridges, used this new material with great intuition. Referring to arch bridges, he proposed the technique of early removal of the centering to obtain partializations at the extrados of the springing with consequent lowering of the center of gravity of the resistant cross-sections. This led to an increase in the sag ratio with a reduction in thrust. The Risorgimento Bridge over the Tiber River in Rome was built with this technique in 1911. It has a span of 100 m and a height of only 10 m. It also represents a bold structure in terms of geometry and execution methods.

A new way of thinking about reinforced concrete architecture was introduced by Robert Maillart. He intuited the great potential of the new material and realized bridges of great elegance and dynamism, appropriately lightened compared to traditional masonry bridges. Among the bridges that have marked Maillart's work is the Tavanasa Bridge, built in 1905, on the Rhine River with a span of 51 m. In this bridge, the arch and the deck are connected in a central area and are separate at the springing. Another example is the Salgina Bridge (Fig. 13), built in 1930 in Schiers with a span of 90 m. In this bridge, arch and deck were connected by some vertical walls.

Figure 13. The Salgina Bridge, Schiers

The prestressed reinforced concrete

In arch bridges, jacks were used to space the various parts before the subsequent casting that joined them together. By artificially compressing the concrete in this way, Eugène Freyssinet intuited the possibility of introducing a state of coercion in a reinforced concrete beam to keep the material in compression everywhere when loads are applied. In reinforced concrete, in fact, the concrete is not used to its best advantage, since its poor tensile strength results, on the one hand, in the presence of material that does not collaborate statically and represents only dead weight, and on the other, in the formation of cracks with consequent exposure of the reinforcement and its oxidation.

The state of coercion is created by mutual contrast between steel cables stretched between the ends of the beam and the beam itself. The contrast can occur at the two ends of the beam, creating a prestressing with sliding cables, or by adhesion between steel and concrete, in which prestressing is given by means of adhering wires.

Due to the slow phenomena of concrete, known respectively as shrinkage (spontaneous reduction in volume) and viscosity (delayed deformation over time in the presence of a constant load), and the relaxation of steel (reduction in tension with constant deformation), the initially applied compression force tends to decrease over time. Therefore, the practical implementation of the prestressing technique was only possible when high-strength harmonic steels were produced, which allow for the application of significant initial prestressing forces. However, a high percentage of these (30–40%) is lost over a certain period of time.

Prestressing, therefore, has made it possible to create slender structures using reinforced concrete with longer spans. In the field of prestressed reinforced concrete bridges, Riccardo Morandi must be remembered. He was an experimental designer rather than a calculator, who operated by relying mainly on his brilliant intuition rather than on abstract theories. Seven patents on prestressing systems are due to his genius. Among the most interesting bridges, it is worth reminding the San Nicola Bridge in Benevento completed in 1955, the Bisantis Viaduct on the Fiumarella in Catanzaro completed in 1962 (Fig. 14), which includes an arch with a span of 235 m, and above all some cable-stayed bridges of great importance, which are described later in this paper.

Mixed steel-concrete systems

Bridges made of steel beams and a reinforced concrete slab above them, in which the advantages of both materials have been exploited, have been widely used in recent decades. The steel beams are mainly entrusted with tensile stresses, while the concrete slab supports compressive stresses and has the task providing the sufficient rigidity and creating a surface suitable for supporting the road surface.

Steel-concrete was born in a rather casual way: it was noted that floors made of iron beams and a concrete slab, calculated considering only the iron beams as load structure and the slab as a dead load without any static contribution, behaved in reality better than expected. This was due to the contribution of the slab, because of composite action between steel and concrete. This adherence between beams and slab was favored by the presence, on the extrados of the beams, of the heads of the nails that opposed the sliding. Great advantages were obtained by improving this adherence.

Figure 14. The Bisantis Viaduct, Catanzaro

In the current construction practice, metal beams are assembled by welding. Electro-welded pins are placed on the upper wings to counteract sliding between the upper wing and the concrete slab. Mixed structures made of prestressed reinforced concrete beams and a reinforced concrete slab are also very common. In these beams, prestressing is applied only to a limited part of the structure, particularly in the portion that would otherwise be subject to tension, with obvious advantages from an economic point of view.

Composite materials

The use of composite materials has been spreading for several decades. Among these, fiber-reinforced polymers (FRPs), already known in the aerospace, automotive, and naval industries, are mostly used. The first applications involved pedestrian walkways and cycle paths and, in some cases, also the decks of road bridges. Composite bridges have significant advantages.

The lightness leads to simplifications in transport operations and installation. Therefore, it is possible to prefabricate large structural elements to be assembled on site using cranes of non-excessive dimensions. The reduced loads require smaller foundations, with smaller excavations, and also determine lower seismic actions. Furthermore, the polymer matrix guarantees good durability. It requires little maintenance, primarily because of its high resistance to atmospheric agents, chemicals, fuels and deicing salts. It also offers greater sustainability due to the absence of harmful emissions during production and the lower energy required for production and transportation. Its mechanical strength is also greater than that of steel and concrete. Finally, it offers good resistance to fire, impact, and fatigue. The wide freedom in the choice of shapes should not be underestimated.

Up to now, their use has been limited by the lack of design standards and above all by the lack of experience using these materials by technicians, as well as by the poor knowledge and reliability of their mechanical properties.

Among the most interesting projects is the mobile bridge over the River Clwyd at Rhyl Harbour in Wales. It consists of two spans, each 30 m long, with a width varying from 3 to 4 m and weighing about 140 kN. The spans are hinged to a central box pier and can be lifted by means of cables pulled symmetrically from a central mast about 50 m high, to allow the passage of boats. The use of FRP has allowed the greatest possible weight savings and has reduced lifting times and energy consumption.

Structural Types

The availability of new materials also determined an evolution of the structural typologies, allowing the overcoming of ever-longer spans with sustainable costs. In beam bridges, which are mainly stressed by bending, the material is often poorly utilized. In a generic cross-section, the maximum compressive and traction tensions under the service loads occur only at the two ends, upper (extrados) and lower (intrados). This limitation is overcome by truss structures, in which the solid wall beam is replaced by a set of rods arranged according to the preferential directions of the main stresses and therefore subject to axial, tensile, or compressive stresses. In this way, the material use is optimized, minimizing its quantity and hence the structural weight, essential requirement when considering long spans. For bridges with longer spans, it is necessary to consider other static types, namely, the arch, the cable-stayed bridge, and the suspension bridge.

Beam bridges

The most common type currently used are beams supported by vertical piers. Generally, these are statically determinate structures, in which the beam of each span is simply supported on the piers and is independent of adjacent spans. Even for small spans, reinforced concrete is not advantageous from an economic point of view. Nowadays, in the field of girder bridges, the most commonly used materials are prestressed reinforced concrete and mixed steel-concrete systems, which offer significant advantages from a construction perspective. Prefabrication and subsequent assembly allow to build a bridge by launching the beams, without providing a centering. This procedure is particularly advantageous when the structure must cross a river or, in the case of overpasses, when it is not possible to interrupt traffic on the road or railway below. Launching can also be realized by longitudinal thrust, which allows the girder to be positioned even on very high piers and to span large distances in inaccessible areas.

The girder can have an open cross-section, composed of a set of parallel longitudinal beams, connected by transverse beams and a top slab that houses the roadway. Alternatively, the girder can have a box or multi-box cross-section, with a top slab, often protruding from the box, which houses the roadway (Fig. 15). The difference between the static behaviors of the two schemes consists essentially in the way of dealing with the torsional actions and, therefore, the rotation of the girder around its longitudinal axis. In an open cross-section, the effect of the torsional actions translates into an increase in bending in the beams (secondary torsion), especially the edge beams, while in the box cross-section it is faced by the primary torsional stiffness of the beam. The second solution allows for overcoming longer spans. In steel beams, the box can also be simulated by connecting the longitudinal beams at their lower flanges with braces in the horizontal plane.

In a simply supported beam, the most stressed section is at mid-span, where the maximum bending moment occurs. A continuous beam, that is, one resting on more than two supports, allows for the creation of spans longer than those of simply supported beams, as each span makes a counterweight action on the adjacent ones. Near the internal supports, the bending moment changes sign; the maximum absolute values of the bending moment occur at the internal supports and are lower (in the case of at least four supports) than the mid-span values of a simply supported beam of the same span. Often, for obvious economic reasons, beams with a variable height section are often used. The piers can have considerable heights, as in the following bridges:

- The Europa Bridge, a continuous six-span beam on the motorway between Brenner and Innsbruck, was the highest bridge in Europe at the time of its completion in 1963. It has a maximum span of 198 m, while the tallest pier is 146.5 m high (Fig. 16).
- The Italia Viaduct on the Lao River, completed in 1969 along the Salerno–Reggio Calabria highway, is a continuous beam with three spans: the central one of 175 m and the side spans of 125 m each. The tallest

(a) (b)

Figure 15. (a) Open cross-section and (b) prestressed reinforced multi-box cross-section

pier is 155 m high. It was the highest bridge in Europe until the completion of the Millau Viaduct in 2004.

Figure 16. The Europe Bridge

A continuous beam can be made statically determinate by adding hinges. If these are positioned in sections where the moment is almost zero for the main load condition, the advantages of the continuous beam in terms of stresses are retained, but also those of statically determinate beams with regards to distortions. The Gerber schemes are based on these considerations. The most common are those with three spans, with the central one longer than the lateral spans. In the Niagara scheme, the two hinges are placed along the central span, while in the Kentucky scheme there is one hinge for each of the lateral spans. The hinges are realized with the typical Gerber saddle, which leaves the total height of the section unchanged.

Arch bridges

Because of its shape, an arch supports external loads mainly through compressive stresses, with an almost uniform distribution in the generic cross-section and, therefore, allows an optimum use of the material. The theoretical limitation of the maximum span of an arch is related to instability problems, typical of structures subject to compression. The subject, approached as a pure scientific curiosity by Leonhard Euler towards the end of the 18th century, found enormous applications with the use of slender structures in the 20th century.

In the field of bridges, the arch always requires a girder, connected to it by vertical elements (columns or struts). The girder houses the road paving and contributes to the arch–beam structural system. Depending on the contribution of the girder, we move from a pure arch, in which the main structural element is the arch alone, while the beam only has the task of transferring the loads acting on it to the arch, to an arch with a stiffening girder, proposed and used by Robert Maillart. In this last latter scheme, a very precise separation of tasks occurs between the beam and the arch. The first, equipped with a high flexural stiffness, is entrusted with the bending moments; the second, instead, made of a very thin thickness, is stressed exclusively by simple compressive stresses. The columns or struts, which connect the beam and the vault, give the vault the stiffening necessary to avoid instability.

The main bridges realized with the Maillart's scheme have already been mentioned. Among the pure arches, we should mention the Sando Bridge in Stockholm, completed in 1943 with a span of 264 m and a rise of 45 m; the Sydney Bridge completed in 1964 with a span of 300 m; and the Wanxian Yangtze Bridge in China, completed in 1997, with a reinforced concrete arch having a span of 429 m and a rise of 85 m.

Steel arch bridges, built with a reticular structure, are also of considerable interest. In addition to the bridges already mentioned, it is worth recalling the following record-breaking bridges:

- The Sydney Harbour Bridge, completed in 1932, with a span of 503 m and a rise of 107 m. It carries four railway tracks and a roadway 17 m wide (Fig. 17).
- The New River Gorge Bridge in Fayetteville, West Virginia, completed in 1977, with a span of 518 m.
- The Lupu Bridge in Shanghai, completed in 2003, with a span of 550 m.
- The Chaotianmen Bridge in Chongqing, China, completed in 2009, with a span of 552 m.
- The Pingnan Third Bridge, on the Xun River near Pingnan, Guangxi, China, with a span of 575 m and a height of 140 m, opened to traffic on December 28, 2020.
- The Tian'e Longtan Bridge over the Hongshui River in the Guangxi Zhuang Autonomous Region, China, opened on February 1, 2024. With a span of 600 m, it is now the longest arch bridge in the world (Fig. 18).

Figure 17. The Sydney Harbour Bridge

When building an arch bridge, it is necessary to provide foundation structures that are capable of transmitting the thrust to the ground. If the foundation soil is not able to withstand such actions, a bowstring bridge can be considered, in which the horizontal force is absorbed by a chord, i.e., a tie rod that connects the arch ends. The chord may also act as a deck that houses the road paving and is suspended from the arch. In the Larsen scheme, the suspension elements are vertical; in the Nielsen scheme, the suspension elements are inclined.

Figure 18. The Tian'e Longtan Bridge, China

Recent constructions demonstrate a rediscovery of the arch for spanning medium to large distances, after limited use in the last decades of the 20th century. In medium spans, steel girder bridges or mixed system bridges are now very competitive, while the field of very large spans remains the domain of cable-stayed bridges and suspension bridges.

Cable-stayed bridges

In a cable-stayed bridge, the deck is supported by inclined cables, the stays, anchored at their other end to a pylon.[16–18] The idea of creating intermediate supports for the beam, by means of lower struts or upper tie rods, had already been known for some time and had been applied by Palladio. The first cable-stayed structures date back to the 17th century. Nevertheless, the cable-stayed bridge had a terrific development only in the last decades of the 20th century. The spans overcome so far are smaller than those of suspension bridges. The advantages of a cable-stayed bridge include greater savings in material, lower assembly cost, and, above all, lower deformability.[19]

As for arch bridges, also for cable-stayed bridges two limit schemes can be identified. The first is that of the bridge with a stiffening girder, which is characterized by a limited number of stays and a girder with a high bending stiffness. The second scheme is the reticular behavior scheme, in which the beam has only the task of transferring the load acting at each section to the two adjacent stays. A certain stiffness of the girder is, however, required to limit the local deformations due to the elongation of the stays.[20]

Riccardo Morandi was inspired by the first scheme when he designed the following prestigious bridges:

- The General Rafael Urdaneta Bridge on the Maracaibo Bay in Venezuela, inaugurated in 1962. The entire viaduct has a total length of about 8700 m and includes five main cable-stayed spans of 235 m each, supported by stays connected to the tops of six 92 m high towers. The deck is 46 m above the lake level. The bridge was initially designed with spans of 400 m, but these were reduced due to the exorbitant cost of the equipment needed for the construction.
- The Polcevera Viaduct in Genoa, built between 1963 and 1967, was part of the A10 motorway. It included two main cable-stayed spans of 210 m, with three towers of approximately 90 m in height. After the collapse of one of the three balanced cable-stayed systems (the first on the left in Fig. 19), which occurred on August 14, 2018, the viaduct was demolished on June 28, 2019. It has been replaced by a continuous beam with a total length of 1067 m and 19 spans, three of them of 100 m, while the others are 50 m, except for two of about 40 and 26 m, respectively. The new deck is composed of a steel box beam shaped like a ship's hull and a reinforced concrete slab. It is supported by elliptic reinforced concrete piers by means of curved surface sliders. The bridge is also equipped with an integrated monitoring system. The simple scheme allowed the construction to be completed in a very short time.[21]
- The Wadi al-Kuf Bridge on the Cyrenaican plateau in Libya, completed in 1971, features two pylons approximately 57 m high above road level and a central span of 282 m. It was the longest span bridge in Africa until 1984 (Fig. 20).
- The Pumarejo bridge (officially named after the president of Colombia, Laureano Gómez Castro, but better known throughout the country by the name of its client, the manager Alberto Pumarejo), was constructed between 1970 and 1974. It includes a main cable-stayed span of 140 m, which crosses the Magdalena River, 20 km from its mouth into the Caribbean Sea, near Barranquilla, Colombia.

Morandi's cable-stayed bridges are characterized by balanced systems with longitudinal A-shaped pylons. Two pairs of cables extend from the top of each pylon, respectively, upstream and downstream of it. The deck is cantilevered from a V-shaped trestle, which extends from the base of the pylon but is independent of it and is suspended from the stays at its ends. The deck's central section also rests on the top of the trestle, resulting in a continuous three-span beam. Buffer spans connect the described structures to each other and to the adjacent parts of the viaduct. During construction, the stays were made only of harmonic steel strands inserted into appropriate sheaths. Once the structure was completed and all permanent loads were applied, the strands were covered with a prestressed rectangular section concrete casting. Finally, the strands and the prestressed concrete were connected by injecting the sheaths. Therefore, the prestressed concrete part contributes only to the travelling loads.

The use of a high number of stays simplifies the construction details relating to the anchors of the girder, reduces assembly problems, and allows the construction of cable-stayed bridges with much longer spans.[22] In the 1970s, it was thought that the cable-stayed bridge would not be suitable for spans longer than 500 m, even though Fritz Leonhardt had proposed a cable-stayed bridge with a central span of 1300 m for the Strait of Messina.[23]

The presentation of the Normandie Bridge project at the Conference on Cable-Stayed Bridges in Bangkok in 1987 paved the way for the use of cable-stayed bridges to overcome very long spans.[24] The Japanese authorities decided

Figure 19. The Polcevera Viaduct, Genoa. The first balanced system on the left collapsed on August 14, 2018

Figure 20. The Wadi al-Kuf cable-stayed bridge, Libya

to change the design of the Tatara Bridge from a suspension bridge to a cable-stayed one. The Normandie Bridge (Fig. 21) was opened to traffic in January 1995. With its 856 m span, it set a new record for cable-stayed bridges, surpassing the Yang Pu Bridge in Shanghai, which had a span of 602 m. The project required detailed static and dynamic studies, which also included the aesthetic aspect, achieving a rare balance between engineering and architecture. The main features of the bridge are the aerodynamic shape of the deck, which reduces wind–induced actions and increases aerodynamic stability, and its high torsional stiffness. This stiffness is provided by the arrangement of the stays, anchored to the outside of the girder and converging at the center of the pylons. The pylons have an inverted Y shape, particularly suited to resist the horizontal actions of the wind. The beam is made of steel in the central part and of prestressed reinforced concrete in the parts near the pylons and in the lateral spans. It is rigidly constrained to the pylons and, in the side spans, is supported by several piers.

The Normandie Bridge lost its record as the longest cable-stayed bridge in the world (it still holds the record in Europe), but it was the first to enter the field of very long spans, which until then had been reserved for suspension bridges. In fact, in 1990 the Tatara Bridge in Japan was completed with a main span of 890 m. The record was subsequently broken by:

Figure 21. The Pont de Normandie, France

- The Sutong Yangtze River Bridge between Nantong and Changshu (a satellite city of Suzhou), completed in 2008, with a main span of 1088 m. The bridge was awarded the Outstanding Civil Engineering Achievement Award by the American Society of Civil Engineers in 2010.
- The Russky Bridge in Vladivostok (Fig. 22), completed in 2012, with a main span of 1104 m. It is currently the longest cable-stayed bridge in the world, with the longest stays (580 m) and pylons reaching 321 m. The design had to take into account the severe climatic conditions, with temperatures ranging from −31 to +37°C, ice formation of considerable thickness, wind speeds of up to 36 m/s and waves reaching 6 m. The deck is 29.5 m wide and accommodates two lanes in each direction.

It is also worth mentioning the Husutong Yangtze River Bridge, opened to traffic in 2020, which crosses the Yangtze River in Jiangsu, China. It is a combined rail and road bridge, with a main span of 1092 m.

Figure 22. The Russky Bridge, Vladivostok

The most recent cable-stayed bridges of greatest interest are in Asia, as well as the future record-breaking cable-stayed bridges. Among these is the Changtai Yangtze River Bridge, located between Changzhou and Taizhou in Jiangsu, China, with a main span of 1208 m. However, there are also interesting applications in Africa, such as:

- The Mubarak Peace Bridge, which crosses the Suez Canal at El-Qantara. The viaduct includes a main cable-stayed span of 400 m, providing a clearance of 70 m for navigation. The pylons, 154 m high, are shaped like Egyptian obelisks.
- The Mohammed VI Bridge (dedicated to the King of Morocco), on the Bou Regreg River near Rabat, Morocco, was inaugurated on July 7, 2016. It has a span of 376 m and two 200-m-high arched towers that symbolize the new gateways to the cities of Rabat and Salé.

Regarding the arrangement of the stays there are mainly two types. In a fan-shaped layout, the stays converge at the top of each pylon. The last outer stay (possibly composed of several cables), that is, the mooring stay, can be anchored either to the ground or to the girder. In the first case, the bridge has external anchors. In the second, the horizontal forces are closed within the structure, and the bridge is self-anchored. In this case, the last stay does not transmit any horizontal force to the ground, but strongly compresses the girder. The vertical force, however, must be resisted by an external support. The other type of stay arrangement is harp-shaped, with parallel stays all having the same inclination.

Among the other notable realizations, are:

- The Alamillo Bridge in Seville, a very striking and innovative structure completed in 1992. It consists of a real harp, with a 200 m span beam and a pylon inclined outward so as to use its own weight to balance the forces transmitted by the stays.
- The Millau Viaduct (Fig. 23), which crosses the Tarn Valley near Millau, France, opened to traffic in 2004. It was designed by Michel Virlogeux in collaboration with Foster and is one of the highest road bridges in the world, with the top of its pylon reaching 341 m. The girder was launched using the incremental longitudinal thrust technique.
- The Stonecutters Bridge in Hong Kong, completed in 2009. With its main span of 1018 m and pylons 298 m high, it was the second cable-stayed bridge in the world at the time of construction.
- The Yavuz Sultan Selim Bridge (Fig. 24), also known as the third bridge over the Bosphorus in Turkey, opened on August 26, 2016. This bridge presents a hybrid suspension–cable-stayed design, with a central span of 1408 m and a deck width of 58.4 m.
- The Hong Kong–Zhuhai–Macau Bridge, a series of bridges and tunnels designed and built to cross the Lingdingyang Canal and connect the cities of Hong Kong, Zhuhai, and Macau, the three major cities of the Pearl River Delta. The crossing, opened to traffic on October 23, 2018, has a total length of approximately 55 km, with a viaduct section of 29.6 km that includes three cable-stayed spans with a maximum span of 460 m.

Suspension bridges

The suspension bridge, which can be seen as an inverted arch, is the structural type that allows the longest spans. It generally has two parallel cables, from which the deck, which houses the road surface, is suspended by means of steel tie rods. The cables extend over three spans, the main span and two side spans. At the ends of the side spans, the cables can be anchored to the girder, which will be highly compressed, and the suspension bridge appears as an inverted thrust-eliminated arch. Alternatively, they can be anchored to the ground by means of foundation structures capable of transferring horizontal actions to the ground. In both cases, the anchors must transmit the vertical uplifting actions to the ground. The girder must support the loads locally, limiting deformations.[25] The importance of the bending stiffness of the girder compared to the extensional stiffness of the cables can be considerable for small and medium spans, but it decreases as the span increases and becomes insignificant in very long-span bridges.[26]

Figure 23. Two piers of the Millau Viaduct during construction

Figure 24. The Yavuz Sultan Selim Bridge, Bosphorus.

The considerable dimensions that are reached make suspension bridges extremely vulnerable to dynamic actions induced by the wind. The natural periods of vibration are very high, placing suspension bridges outside the range of seismic interest. Nevertheless, the evaluation of the effects of an earthquake is quite complex, since the pylons and anchors are very distant from each other and therefore subject to seismic actions of different intensity and characteristics.[27]

It has been said that the first suspension bridges had natural fiber cables. The first transformation occurred in

China, where the fiber cables were replaced by iron chains joined by bars of 1 inch diameter, and the pylons were often made of masonry. An elegant example of this type is a 60-m-long chain bridge over the Hwa Kiang River, built in 1632 and still standing. Many smaller chain bridges exist in northern China, and for safety reasons, the number of animals crossing the bridge at the same time is carefully limited.

The first suspension bridges of the modern era were built at the end of the 18th century in England and the United States. These too were chain bridges. At that time, the studies of Johann Bernoulli (1691) on the catenary and of Fuss (1794) on the parabolic cable were already known. The stability of the bridge was entrusted exclusively to the cables, while the beam had only the task of transferring the loads to the cables themselves.

There was great interest in suspension bridges also in France. Claude Navier visited England in 1821 with the aim of studying suspension bridges and, in 1823, he published his book *Mémoires sur les ponts suspendus*. In 1826, the 175 m Menai Straits Bridge was completed, which set an engineering standard for the future and set a world record for its length. The bridge, which impressed Navier and influenced most bridge engineers, was supported by chains with flat wrought iron links. Vertical and horizontal vibrations caused by the wind damaged it. The importance of the girder was then understood. This, with its bending stiffness, could reduce the high deformability of a suspension bridge under vertical loads.

Chain suspension bridges were also built in Italy. The Lima Bridge at Formali from 1840 still exists. The Real Ferdinando Bridge, near the mouth of the Garigliano River, has recently been restored, while only the four masonry pylons remain of the Calore Bridge near Benevento. These last two bridges were built by the Bourbons in 1830–1831, demonstrating their sensitivity to technological progress.

The technique improved rapidly, and in 1883 the Brooklyn Bridge in New York was completed. It has masonry pylons and a span of 486 m, that is, double the longest existing span. The development of the theory allowed the design of bridges with ever-greater spans.[28] There were some failures, such as the Tacoma Narrows Bridge in 1940, which had a span of 853 m and a girder only 2.44 m high. It collapsed under the action of the wind after days of agony, further highlighting the importance of the stiffness of the girder. The new bridge, built in 1950, has the same span but a 10-m-high girder. Today, the tendency is to create aerodynamically shaped girders, transparent to the wind, which cause the minimum possible disturbance to the natural flow of air. The behavior of the bridge is always studied with models in wind tunnels before construction.

After the Brooklyn Bridge, there was a gradual but remarkable increase in span:

- In 1932, the George Washington Bridge in New York was completed. It was the first bridge to exceed 1 km, with its main span of 1067 m.
- In 1937, it was the turn of the Golden Gate Bridge in San Francisco, an area very exposed to the currents and winds from the Pacific Ocean (Fig. 25). It has a span of 1280 m and is probably the most famous suspension bridge in the world.
- In 1964, the Verrazzano Bridge was opened to traffic. It connects Brooklyn to Staten Island in New York and is still the longest bridge in the United States, with its 1298 m span.
- In 1981, the record passed to the Humber Bridge between Barton-upon-Humber and Hessle in Humbershide, England, whose main span is 1410 m.
- In 1996, the Great Belt Link East Bridge in Denmark was completed, with a main suspended span of 1624 m. The deck has an aerodynamic cross-section offering little resistance to the wind.
- In 1998, the Akashi Kaikyo Bridge in Kobe, Japan (Fig. 26), was inaugurated. During construction, the bridge was subjected to the earthquake that destroyed Kobe on January 17, 1995. The event had a magnitude of 7.2 and an epicenter very close to the bridge. A relative displacement of about 1 m occurred between the pylons, and following this, the main span increased to 1991 m. The pylons and cables, already in place at the time of the earthquake, were not damaged. The design of the girder was revised to adapt it to the new length. The Akashi Kaikyo Bridge remained the longest bridge in the world for a long time.
- Finally, in March 2022, a year and a half ahead of schedule, the 1915 Çanakkale Bridge on the Dardanelles Strait in Turkey, between Asia and Europe, was inaugurated (Fig. 27). The suspended part has a total length of 3563 m, with a central span of 2023 m. The two pylons are submerged for 37 and 318 m above the water. The roadway, with three lanes in each direction, is 36 m wide and approximately 70 m above sea level. The deck is supported by multidirectional sliding spherical bearings at the abutments, while the transverse constraint is achieved by eight elastomeric bearings arranged vertically at the abutments and towers. The seismic protection system consists of eight special fluid-dynamic dissipators installed longitudinally between the suspended deck and the towers.

In addition to these, the following bridges deserve to be mentioned, although they did not set new records:

- The Firth Road Bridge in Edinburgh, completed in 1964. It was the first European bridge to exceed 1 km, having a span of 1006 m.
- The Bogazici Bridge, opened to traffic in 1973, with a span of 1074 m (Fig. 28), and the Fatih Sultan Mehmet Bridge, completed in 1987, with a span of 1090 m, both on the Bosphorus in Istanbul.
- The South Bisan in Japan, part of the Seto Ohashi Bridge, an engineering feat consisting of three suspension bridges, two cable-stayed bridges, one truss bridge and five viaducts, between the islands of Honshu and Shikoku. The bridge was completed in 1988 and has a main span of 1100 m.

- The Xihoumen Bridge in the Zhoushan Archipelago in China, completed in 2009, with a central span 1650 m long.

Figure 25. The Golden Gate Bridge, San Francisco

Figure 26. The Akashi Kaikyo Bridge, Kobe

Figure 27. The 1915 Çanakkale Bridge, Dardanelles Strait

Finally, the project to cross the Strait of Messina deserves special mention. In addition to the attractive proposals for an underground tunnel, rejected due to the considerable depth of the seabed, and the so-called Archimedes Bridge, an underwater tunnel anchored to the seabed, two main bridge options have been proposed: a cable-stayed bridge with pylons in the water and a suspension bridge with pylons on dry land. The latter was considered the viable solution. If built, the Messina Strait Bridge would have the longest span in the world, with 3300 m between the two pylons, far greater than the current maximum span. The deck, featuring an original aerodynamic shape and known as the Messina-type deck, is suspended by two pairs of cables.[29] The towers are 370 m high, and the foundations, both at the pylons and at the cable anchors to the ground, are very large. Special measures will be implemented at the towers and terminal structures to withstand horizontal forces and thermal effects.

Figure 28. The Bogazici Bridge, Istanbul

Conclusions

Bridge design requires expertise in road, hydraulic, geotechnical, structural, and environmental engineering. Project planning requires accurate and in-depth knowledge of the geomorphology of the area of interest. If the bridge spans a river, a thorough hydraulic study must be conducted, and the effects of the piers on water flow must be assessed. Once the bridge location, alignment, and geometric characteristics (namely, the span and transverse profile) are known, the connections with the road at the abutments must be defined. The results of the geotechnical investigations can also lead to a revision of the project, with modifications to the road layout. They are crucial in choosing the structural typology and foundation type.

The study of deformation and stress regimes is nowadays performed with the aid of sophisticated finite element calculation and analysis codes that allow for accurate modeling of all structural aspects. However, most existing structures were designed without such tools. The structure was reduced to a theoretical calculation model through a series of simplifications and hypotheses. When the definition of a suitable theoretical model was uncertain or the calculation models were unsatisfactory, an experimental model was realized and tested, especially in the case of large structures. Preliminary determination of the most severe load conditions among the infinite possibilities was essential, and this was accomplished by drawing influence lines. Particular attention was paid to studying the transverse position of the loads, for which various theories were developed that considered the non-negligible width of the beam itself.

Despite all these challenges, an old saying goes: "Give us the plans, and we will build a bridge to heaven or to hell."

The most daring challenge for the future is that of very long spans. The free space required for navigation, due to the increase in the size of boats and the volume of marine traffic, will determine the need to realize bridges with ever-longer spans. On the other hand, the lower cost of horizontal structures compared to that of deep foundations in water will favor the design of bridges with longer spans. This choice also reduces the risk of collision of boats against the piers. Therefore, the battle against the forces of nature continues and will require great technical knowledge, but also uncommon skills, intuition, and audacity.

As the span increases, the self-weight of a structure increases, and a high percentage of its load-bearing capacity is used to support itself. The limit span, that is, the span for which the bridge can support only its self-weight but no other loads, depends on the structural type, the resistance of the material used, and its weight per unit volume. For a cable of harmonic steel with a sag-to-span ratio equal to 0.1, the limit span is approximately 8000 m. Considering other permanent and travelling loads, it can be deduced that the limit span for a suspension bridge made of traditional materials is much lower. Therefore, the possibility of bridges with very long spans is related to the use of more resistant and lighter materials than the current ones.

Materials will continue to improve in the future, structural types will be optimized, and the construction of a bridge will always be something special: "When you build a bridge, you build something for all time," said Joseph Strauss.

References

[1] Clemente P. Monitoring and evaluation of bridges. Lessons from the Polcevera Viaduct collapse in Italy. *J Civil Struct Health Monit*. 2020;10(2):177–182. doi:10.1007/s13349-020-00384-6.

[2] Ormando C, Lucaferri V, Giocoli A, Clemente P, Buffarini G, Tofani A. Index of attention for a simplified condition assessment and classification of bridges. *Infrastructures*. 2024;9(8):125. doi:10.3390/infrastructures9080125.

[3] Buffarini G, Clemente P, Giovinazzi S, Ormando C, Pollino M, Rosato V. Preventing and managing risks induced by natural hazards to critical infrastructures. *Infrastructures*. 2022;7(6):76. doi:10.3390/infrastructures7060076.

[4] Buffarini G, Clemente P, Giovinazzi S, Ormando C, Scafati F. Structural assessment of the pedestrian bridge accessing Civita di Bagnoregio, Italy. *J Civil Struct Health Monitor*. 2023;13(8):1499–1516. doi:10.1007/s13349-022-00628-7.

[5] Kranakis E. *Constructing a Bridge*. Cambridge, Massachusetts: The MIT Press; 1997.

[6] Cassady S. *Spanning the Gate*. Santa Rosa, CA, USA: Square books; 1986.

[7] Raithel A. *Costruzioni di ponti*. Napoli: Liguori; 1962.

[8] Raithel A. *Ponti a travata*. Napoli: Liguori; 1970.

[9] Widmann R, Müller A. History and development stages in timber bridge construction in Switzerland. In: *Conference Proceedings 4th ICTB*. Biel/Bienne, Switzerland; 2022. doi:10.24451/779w-2t59.

[10] Clemente P, Ormando C. CM/SHM of historic masonry arch bridges. In: Karbhari VM, Ansari F, eds. *Condition Monitoring of Infrastructure Systems*. Sawton, Cambridge, UK: Woodhead Publishing Ltd; in press, Cap. 5. doi:10.1016/B978-0-443-38315-1.00027-1.

[11] Clemente P, Occhiuzzi A, Raithel A. Limit behavior of stone arch bridges. *J Struct Eng*. 1995;121(7):1045–1050. doi:10.1061/(ASCE)0773-9445(1995)121:7(1045).

[12] Clemente P, Saitta F. Analysis of no-tension material arch bridges with finite compression strength. *J Struct Eng*. 2017;143(1):04016145. doi:10.1061/(ASCE)ST.1943-541X.0001627.

[13] Clemente P, Saitta F, Ormando C, Buffarini G. Masonry arch bridges with finite compression strength subject to horizontal longitudinal seismic actions. *Appl Sci*. 2023;13(13):7509. doi:10.3390/app13137509.

[14] Dani F. *Il libro dei ponti*. Pomezia: SARIN; 1988.

[15] Mao YS. *Bridges in China: Old and New*. Peking: Forein Languages Press; 1978.

[16] Podolny W, Scalzi J. *Construction and Design of Cable-Stayed Bridges*. Hoboken, USA: John Wiley and Sons; 1976.

[17] Troitsky MS. *Cable-Stayed Bridges*. London: Crosby Loockwood Staples; 1977.

[18] Billington DP, Nazmy A. History and aesthetics of cable-stayed bridges. *J Struct Eng*. 1991;117(10):3103–3134. doi:10.1061/(ASCE)0733-9445(1991)117:10(3103).

[19] Clemente P, Marulo S, Lecce L, Bifulco A. Experimental modal analysis of the Garigliano cable-stayed bridge. *Soil Dyn Earthq Eng*. 1998;17(7–8):485–493. doi:10.1016/S0267-7261(98)00022-0.

[20] Clemente P, Bongiovanni G, Buffarini G, Saitta F. Structural health status assessment of a cable-stayed bridge by means of experimental vibration analysis. *J Civil Struct Health Monit*. 2019;9(5):655–669. doi:10.1007/s13349-019-00359-2.

[21] Clemente P, Ormando C. Monitoring system of the San Giorgio bridge at Genoa, Italy. *The Monitor*. Winter 2021. https://ishmii.org/the-monitor/.

[22] Podolny W. Future trends in cable-stayed bridges. *Proceedings of IASS Symposium Spatial Structures: Heritage, Present and Future (Milan, 1995)*. 1995;2:985–994; SGE Padova.

[23] Clemente P. On the limit span of cable-stayed structures. In: *IABSE Report Long-Span and High-Rise Structures*. Zurich: IABSE; 1998;79:287–292.

[24] Virlogeux M. The normandie bridge, France: a new record for cable-stayed bridges. *Struct Eng Int*. 1994;4(4):208–2013. doi:10.2749/101686694780601629.

[25] Pugsley A. *The Theory of Suspension Bridges*. 2nd ed. London: Arnold LTD; 1968.

[26] Clemente P, Nicolosi G, Raithel A. Preliminary design of very long-span suspension bridges. *Int J Eng Struct*. 2000;22(12):1699–1706. doi:10.1016/S0141-0296(99)00112-1.

[27] Clemente P. Effects of differential displacements between the ground anchors in suspension bridges. *Infrastructures*. 2024;9(11):211. doi:10.3390/infrastructures9110211.

[28] Buonopane SG, Billington DP. Theory and history of suspension bridge design from 1923 to 1940. *J Struct Eng*. 1993;119(3):954–977. doi:10.1061/(ASCE)0733-9445(1993)119.

[29] Brancaleoni F, Diana G. The aerodynamic design of the Messina Straits Bridge. *J Wind Eng Ind Aerodyn*. 1993;48(2–3):395–409. doi:10.1016/0167-6105(93)90148-H.